FEDERAL UNIVERSITY OF SÃO CARLOS
CENTER OF EXACT SCIENCES AND TECHNOLOGY
POSTGRADUATE PROGRAM IN MATERIALS SCIENCE AND ENGINEERING

FRICTION SPOT JOINING OF ALUMINUM ALLOY 2024-T3 AND CARBON-FIBER-REINFORCED POLYPHENYLENE SULFIDE COMPOSITE LAMINATE WITH ADDITIONAL PPS FILM INTERLAYER

Natália Manente André

São Carlos
2015

FEDERAL UNIVERSITY OF SÃO CARLOS
CENTER OF EXACT SCIENCES AND TECHNOLOGY
POSTGRADUATE PROGRAM IN MATERIALS SCIENCE AND ENGINEERING

FRICTION SPOT JOINING OF ALUMINUM ALLOY 2024-T3 AND CARBON-FIBER-REINFORCED POLYPHENYLENE SULFIDE COMPOSITE LAMINATE WITH ADDITIONAL PPS FILM INTERLAYER

Natália Manente André

Master thesis submitted to the Postgraduate Program in Materials Science and Engineering as a partial requirement to obtain the degree of MASTER IN MATERIALS SCIENCE AND ENGINEERING

Advisor: Dr. Leonardo Bresciani Canto (UFSCar/DEMa)
Co-Advisor: Dr.-Ing. Sergio de Traglia Amancio Filho (HZG/Germany)
Financial Support: FAPESP

São Carlos
2015

Ficha catalográfica elaborada pelo DePT da Biblioteca Comunitária UFSCar
Processamento Técnico
com os dados fornecidos pelo(a) autor(a)

André, Natália Manente
A555fs Friction spot joining of aluminum alloy 2024-t3 and carbon-fiber-reinforced polyphenylene sulfide composite laminate with additional pps film interlayer / Natália Manente André. -- São Carlos : UFSCar, 2016.
113 p.

Dissertação (Mestrado) -- Universidade Federal de São Carlos, 2015.

1. Soldagem. 2. União pontual por fricção. 3. Estrutura híbrida. 4. Filme intermediário. 5. CF-PPS. I. Título.

DEDICATORY

I kindly dedicate this MSc thesis to the bravest woman I have ever met: Delvania Desolina Manente, my loved mother.

VITAE OF THE CANDIDATE

Bachelor's in Materials Engineering at the Federal University of São Carlos (UFSCar, 2014) with emphasis on polymeric materials.

UNIVERSIDADE FEDERAL DE SÃO CARLOS

Centro de Ciências Exatas e de Tecnologia
Programa de Pós-Graduação em Ciência e Engenharia de Materiais

Folha de Aprovação

Assinaturas dos membros da comissão examinadora que avaliou e aprovou a Defesa de Dissertação de Mestrado da candidata Natália Manente André, realizada em 30/11/2015:

Prof. Dr. Leonardo Bresciani Canto
UFSCar

Prof. Dr. José Alexandrino de Sousa
UFSCar

Prof. Dr. José Ricardo Tarpani
USP

ACKNOWLEDGMENTS

The development of this MSc thesis counted with the support and contribution of many people who I would like to sincerely thank:

- Prof. Dr. Leonardo Bresciani Canto for the supportive orientation, unconditional dedication and confidence in this work.
- Prof. Dr.-Ing. Sergio Amancio for the honorable opportunity to perform this MSc study in partnership with the Young Investigator Group. Foremost for all discussions, encouragement and precious guidance in this work.
- Dr.-Ing. Seyed Mohammad Goushegir for kindly sharing with me his expertise in FSpJ through valuable lessons and absolute support. Above all, for his priceless advices, encouragement, patience and friendship.
- The Young Investigator Group, for the greatest example of competence and dedication. Special thanks to my colleagues André Abibe, Lucian Blaga, Bruno Proença and Natascha Borba for the support and friendship.
- All my colleagues of Helmholtz-Zentrum Geesthacht for their support and fellowship during my stay in Germany. Specially to Dr. Jorge dos Santos for the internship opportunity and support of this work.
- My dearest friends Thereza, Leandro, Bruno and Thales for all fun, comprehension and support during the good and hard times.
- My loved girls Naiara, Giovana, Jéssica and Jéssica for being with me even from far away, and Natascha, Fernanda, Juliana and Debby for making my life lighter in a daily basis.
- My beloved family for all confidence and supportive love. Specially to my mom: there are no enough words in this world to express my gratitude for all you have done for me. I love you!
- FAPESP for sponsoring me with a MSc scholarship.
- All members of DEMa/UFSCar and PPG-CEM for the professional support and opportunity to conclude this MSc study in such renowned and dignified institution.
- Finally, and most important, God for the guidance and all blessings in my journey.

ABSTRACT

Friction Spot Joining (FSpJ) is a prize-winning joining technique for hybrid metal-polymer composite structures. This master thesis was devised to investigate the feasibility of FSpJ of metal-composite structures with additional film interlayer. Friction spot joints of aluminum alloy 2024-T3 and carbon-fiber-reinforced polyphenylene sulfide laminate composite with additional PPS film interlayer were successfully produced. The highest peak temperature achieved during the joining process was 417°C. DSC analysis demonstrated that the degree of crystallinity decreased for the composite (from 22% to 12%) and increased for the PPS film (from 7% to 27%) after joining. TGA analysis indicated that no extensive thermo-mechanical degradation induced by the joining process occurred. The main bonding mechanisms of FSp joint were identified as macro- and micro-mechanical interlocking, as well as adhesion forces. The process-related microstructural effects were evaluated and correlated to the local mechanical performance of the joining parts through micro and nanohardness. Further, mechanical grinding, sandblasting and plasma activation surface pre-treatments were performed on the composite part to enhance the adhesion between the joining parts. The generated surface features due to the surface pre-treatments were correlated to the mechanical performance of the joints. Sandblasted specimens showed the best mechanical performance among the surface pre-treatments used in this work. The lap shear strength of joints with interlayer (2703 ± 114 N up to 3069 ± 166 N) was up to 55% higher than the corresponding joints without film. The fatigue life of the joints with interlayer was 4 times longer in comparison with those without interlayer; superior fatigue strength was also observed. The durability of the joints was evaluated through hydrothermal accelerated aging; the maximum reduction in initial strength was 12.4% for 28 days of aging. Finally, the failure mechanisms of the joints were discussed, demonstrating a mixture of adhesive-cohesive failure mode.

UNIÃO PONTUAL POR FRICÇÃO (FSpJ) DE JUNTAS HÍBRIDAS CONSTITUÍDAS DE ALUMÍNIO 2024-T3 E COMPÓSITO LAMINADO DE POLISULFETO DE FENILENO REFORÇADO COM FIBRA DE CARBONO COM FILME INTERMEDIÁRIO DE PPS

RESUMO

A União Pontual por Fricção (FSpJ) é uma técnica internacionalmente premiada para união de estruturas híbridas metal-compósito polimérico. Esta dissertação de mestrado investigou a viabilidade técnica da produção de juntas metal-compósito com filme polimérico intermediário através do FSpJ. Juntas de alumínio 2024-T3 e laminado compósito de poli(sulfeto de fenileno) (PPS) reforçado com fibras de carbono com filme intermediário de PPS foram produzidas com sucesso. A máxima temperatura processual identificada foi de 417°C. Análises de DSC demonstraram decréscimo no grau de cristalinidade do compósito (de 22% para 12%) e acréscimo no caso do filme intermediário (de 7% para 27%) depois de submetidos ao processo de união. Análises de TGA não identificaram evidências de ocorrência de degradação termomecânica dos componentes poliméricos das juntas induzida pelo FSpJ. Os principais mecanismos de união identificados na interface das juntas foram macro- e micro-ancoramento mecânico, além de forças adesivas. As mudanças microestruturais induzidas pelo processo de união foram investigadas e correlacionadas com o desempenho mecânico local dos componentes da junta através de medidas de micro e nanodureza. Pré-tratamentos superficiais de lixamento, jateamento de areia e ativação por plasma foram realizados no componente compósito a fim de aprimorar a adesão entre os componentes a serem unidos. As superfícies pré-tratadas foram caracterizadas e suas propriedades foram correlacionadas com a resistência mecânica das juntas correspondentes. As amostras jateadas produziram juntas com a melhor resistência mecânica entre os pré-tratamentos superficiais investigados neste estudo. A resistência ao cisalhamento das juntas com filme (2703 ± 114 N até 3069 ± 166 N) apresentou-se até 55% superior à resistência das respectivas juntas sem filme. A vida em fadiga das juntas com filme apresentou-se cerca de 4 vezes mais longa em comparação às juntas sem filme. A durabilidade das juntas foi investigada através de envelhecimento hidrotérmico acelerado, sendo que a máxima redução em resistência ao cisalhamento foi de 12,4% para 28 dias de envelhecimento. Finalmente, os mecanismos de falha das juntas foram discutidos, demonstrando a predominância do modo coesivo de falha.

LIST OF PUBLICATIONS

ANDRÉ, N. M.; GOUSHEGIR, S. M.; SANTOS, J.; CANTO, L. B.; AMANCIO-FILHO, S. T. Influência da espessura do filme polimérico intermediário na resistência mecânica de juntas híbridas de alumínio 2024-T3 e CF-PPS produzidas por União Pontual por Fricção. Submitted to Soldagem & Inspeção, 2015.

ANDRÉ, N. M.; GOUSHEGIR, S. M.; SANTOS, J.; CANTO, L. B.; AMANCIO-FILHO, S. T. Influência termomecânica do processo de União Pontual por Fricção na recristalização dos componentes poliméricos de junta híbrida CF-PPS/Alumínio com filme intermediário de PPS. In: 13° CONGRESSO BRASILEIRO DE POLÍMEROS, Natal, Brazil, 18-22 of October, 2015.

ANDRÉ, N. M.; GOUSHEGIR, S. M.; SANTOS, J.; CANTO, L. B.; AMANCIO-FILHO, S. T. Influência da espessura do filme polimérico intermediário na resistência mecânica de juntas híbridas de alumínio 2024-T3 e CF-PPS produzidas por União Pontual por Fricção. In: XLI CONGRESSO NACIONAL DE SOLDAGEM, Salvador, Brazil, 12-15 of October, 2015.

ANDRÉ, N. M.; GOUSHEGIR, S. M.; SANTOS, J.; CANTO, L. B.; AMANCIO-FILHO, S. T. Friction Spot Joining of Aluminum Alloy 2024-T3 and Carbon-Fiber-Reinforced Poly(phenylene sulfide) with Additional PPS Film Interlayer: Microstructure, Mechanical Strength and Failure. Submitted to Composites-Part B Engineering, 2015.

x

CONTENTS

LIST OF TABLES

LIST OF FIGURES

LIST OF ABBREVIATIONS

AA	Aluminum alloy
ANOVA	Analysis of variance
AZ	Magnesium alloy
CF	Carbon fiber
CTE	Coefficient of thermal expansion
DSC	Differential Scanning Calorimetry
FSpJ	Friction Spot Joining
GF	Glass fiber
HZG	Helmholtz-Zentrum Geesthacht
PA	Polyamide
PEEK	Polyether ether ketone
PPS	Polyphenylene sulfide
SEM	Scanning electron microscopy
TGA	Thermogravimetric Analysis
TUHH	Hamburg University of Technology
XPS	X-ray Photoelectron Spectroscopy
wt	Weight
5H Satin	5 harness of fabric woven with a glossy face and a dull back
CPS	Counts per second
ULSF	Ultimate lap shear force

LIST OF SYMBOLS

Al_2O_3	Corundum alumina
R_a	Arithmetic average surface roughness parameter
SiC	Silicon carbide
T_{cc}	Temperature of cold crystallization
T_c	Temperature of crystallization
T_g	Temperature of glass transition
T_m	Temperature of melting
X_c	Degree of crystallinity
W_f	Weight percentage of carbon fiber in the composite
γ_{LV}	Interfacial free energy per unit area of liquid-vapor
γ_{SL}	Interfacial free energy per unit area of solid-liquid
γ_{SV}	Interfacial free energy per unit area of solid-vapor
θ	Equilibrium contact angle
ΔH_m	Enthalpy of melting
ΔH_{cc}	Enthalpy of cold crystallization
ΔH^0_m	Enthalpy of fusion for 100% crystalline material

1 INTRODUCTION

Metal-composite hybrid structures combining carbon-fiber-reinforced polymer composites and lightweight metal alloys have become a matter of success for transport industries, such as aeronautical and automotive [1]. The new economic and environmental policies are increasingly rigorous on developers and manufacturers. Reduction of CO_2 emission and fuel consumption are the most demanding issues. The concept of metal-composite hybrid structures is a promising solution to fulfill these requirements mainly due to the optimal specific strength and stiffness associated to these materials [2].

The development of lightweight hybrid structures has recently been the focus of the transport industries. In aircraft industry, for instance, the Boeing 787 is composed of over 50 wt% advanced polymer composites in its structure, saving 20% of the total aircraft weight compared to the conventional aluminum structure [3]. Over the past 30 years Airbus has also addressed the use of carbon-fiber-reinforced polymer composites (CFRP). Some of the applications of CFRPs reported by Airbus are the wing movables and the vertical tail plane of A310, the horizontal tail plane of A320, the keel beam of A340-600, the center wing box of A380 as well as the wing parts of Falcon 10, ATR 72 and A400M [4]. Recently, the A350 XWB launch has set a new standard at Airbus with the use of 53 wt% composites in its structure contributing to a reduction of 25% in fuel consumption [4]. Embraer, the largest aircraft manufacturer in South America, has also invested in carbon-fiber-reinforced polymers with recent release of the military transport aircraft KC-390 [5]. The KC-390 presents lightweight ballistic protection solutions provided by the use of composites [5]. Additionally, in the automotive industry, for example the new generation of fully electric and hybrid cars has been developed by BMW (e.g., i3 and i8) [6]. By replacing steel with carbon-fiber-reinforced polymers, BMW engineers were able to reduce 18% of the car weight, while reductions of 50% in energy and 70% in water consumption were accomplished during the manufacturing process [6].

Friction Spot Joining (FSpJ) is an innovative friction-based joining technique for hybrid structures developed at Helmholtz-Zentrum Geesthacht

(HZG), Germany [7]. The FSpJ is a suitable process for joining of metal-polymer or composite hybrid structures. One of the major advantages over currently available welding-based techniques lies on the fact that FSpJ avoids or reduces polymer degradation and damage of composite fiber network, which may cause a decrease in the mechanical performance of the hybrid joint. Additionally, FSpJ presents short joining cycles, while extensive surface preparation is not mandatory [8].

The feasibility of the FSpJ process was investigated for different combination of materials such as magnesium alloy AZ31 [8], Al 6181-T4 [9], and Al 2024-T3 [10] to carbon (CFRP) and glass fiber (GFRP) reinforced polymers.

The use of an additional film interlayer may increase the in-plane shear strength, out-of-plane load-carrying capability and corrosion resistance of spot-welded joints [11]. The larger bonding area provided by the film may also improve load and stress distribution, enhancing the fatigue life of the joints [11, 12]. Mitschang *et al.* [13] investigated the influence of a polymer film interlayer on the mechanical performance of metal-composite joints produced by induction welding. From the current knowledge of the author, apart from this publication there are no scientific studies exploring the effects of the interlayer on the behavior of the metal-composite joints produced by welding-based techniques (see Chapter 3 for the description of state-of-the-art in welding-based techniques). Therefore, the accomplishment of this thesis advances the scientific knowledge of using the film interlayer not only with FSpJ but also other similar metal-composite joining technologies.

In the current study, Al 2024-T3/CF-PPS with additional PPS film interlayer joints were successfully produced and studied. The use of a film interlayer was a strategy based on the weld-bonding technology to improve the mechanical performance of the hybrid FSp joints. During the FSpJ process, the interlayer is melted and recrystallized forming a thin layer in between the joint's parts. Therefore, superior load distribution and mechanical strength can be achieved as a result of the larger bonding area and pronounced adhesion forces provided by the interlayer material. In addition, the use of a film may

exempt the required curing time of an adhesive compared to the currently used industrial adhesives [14].

This MSc thesis is structured as follows. After this introduction the objectives of the work is presented in Chapter 2. Chapter 3 briefly reviews the state-of-the-art literature on various metal-polymer joining techniques including FSpJ. Further, it describes the materials used in this work as well as the principles of composite surface pre-treatments and their influence on metal-polymer adhesion. Technical details of the materials used as joining parts and the experimental methods are described in Chapter 4. The main results obtained in the current work and the respective discussions are presented in Chapter 5. The results and discussion chapter is divided into the evaluation of temperature evolution, process-related physicochemical changes, bonding mechanisms at the joint's interface, process-related microstructural effects, influence of composite surface pre-treatments, quasi-static and cyclic global mechanical performance and failure mechanisms of single lap shear joints. Finally, the conclusions and the recommendations for future work are given in Chapter 6 and Chapter 7, respectively.

2 OBJECTIVES

This study aimed to evaluate the effect of adding the PPS film interlayer on the behavior of Al 2024-T3 and CF-PPS single lap friction spot joints. Where needed, a comparison with the Al 2024-T3/CF-PPS joints without interlayer was made to better understand the influence of the interlayer. The following specific objectives were defined for this work:

Scientific objectives:

- Evaluate the bonding mechanisms of Al 2024-T3 and CF-PPS FSp joints with PPS film interlayer, as well as the physicochemical and microstructural changes of the joining parts, and their relation with the joining parameters (heat input).
- Understand the influence of composite surface pre-treatments and accelerated environmental aging on the mechanical performance of the joints.
- Investigate the global mechanical performance of the single lap FSp joints under static and dynamic loading and the respective failure mechanisms.

Engineering objective:

- Demonstrate the feasibility of FSpJ for metal-composite with interlayer and its potential for the transport industry.

3 LITERATURE REVIEW

3.1 Metal-Composite Joining Technologies

The possibility of joining metals with polymer composites is one of the most important issues to the cost-effectiveness of the hybrid structures in mass production industries, such as transport. Because of the high dissimilarity in physicochemical properties of metals and polymer composites, design of large and complex hybrid structures is not a simple achievement and requires advanced joining techniques [15-18]. There are basically three categories of processes to join hybrid structures: mechanical fastening, adhesive bonding, and welding-based techniques.

Currently, mechanical fastening and adhesive bonding are the most applied techniques for joining dissimilar materials [2, 19]. Mechanical fastening allows the joining of extremely dissimilar materials while retaining their individual properties [19]. Adhesive bonding enables the joining of dissimilar materials without generation of thermal stresses as found in welding-based techniques [20]. Furthermore, the adhesive bonding provides a surface-related instead of spot-related load transfer with homogeneous load distribution [20]. Despite the mentioned benefits, these techniques have some intrinsic limitations. In mechanical fastening, weight penalty and stress concentration are the main limitations, whereas adhesive bonding often requires extensive surface preparation and long curing time of the thermoset adhesive [20, 21].

Due to the increasing importance of joining metals to polymer composites, and the limitations of mechanical fastening and adhesive bonding, a number of alternative welding-based techniques have been recently developed. Resistance, induction, ultrasonic and laser welding have been introduced with different related advantages and drawbacks [17].

Resistance welding is a fusion bonding process which uses an electric current as heat source. Several studies have described this process and demonstrated the feasibility of joining metal-polymer composite structures by resistance welding [17, 22, 23]. Among its advantages, ease of automation and cost efficiency have been listed [22]. However, disadvantages such as

mandatory additional heating element and long welding cycles (1-11 minutes) are reported in the literature [22].

Induction welding uses an alternating electromagnetic field as an inductive heating to melt the composite matrix and produces a joint between metal and composite under pressure [13]. It was reported that induction welding produces strong joints, being a well-controllable and simple process [13]. Nevertheless, relatively long welding cycles (1-4 minutes), low energy efficiency (thermal losses by Joule effect) and expensive equipment are some drawbacks of induction welding process [1].

Laser welding is another recent metal-polymer composite joining technique in which the heat source is an electromagnetic radiation with high energy density [24]. Laser non-transparent materials are joined through radiation absorption resulting in joints with a well-defined heat affected zone and low residual stresses [24-26]. Yet, expensive equipment and high generation of volumetric defects due to local polymer degradation are currently the main limitations of laser welding technique [27].

Ultrasonic welding has also been recently explored for hybrid metal-polymer composite structures [28]. Frictional heat is generated at the interface between parts through high frequency vibration of a tool [29]. It presents very short joining cycles (1-4 s) and high energy efficiency [29]. However, the welding equipment is expensive and the technique is suitable only to thin metal sheets (usually up to 3 mm thick for aluminum alloys of 2XXX series in the annealed state) [29].

Generally, these joining techniques have presented robust processes and good quality joints [13, 18, 22]. However, the limitations mentioned above have motivated further scientific and engineering developments in the area of joining metal-polymer structures [17].

3.2 Friction Spot Joining (FSPJ)

Friction Spot Joining (FSpJ) is a prize-winning friction-based joining process for metal-polymer and metal-polymer composite hybrid structures [30-

34]. FSpJ has been investigated within a cooperation between UFSCar and HZG since 2008 [8, 9, 35].

The FSpJ uses a three piece, non-consumable tool comprising a pin, a sleeve, and a clamping ring, which have independent axial and rotational actions (Figure 3.1).

Figure 3.1 FSpJ tools used in this study (dimensions in mm). (Adapted from [8]).

Prior to the joining process, the parts are clamped between a backing plate and the clamping ring to ensure intimate contact between them during the process. Moreover, clamping is responsible to avoid (or decrease to a minimum) separation of the joining parts during the cooling stage at the end of the process.

The FSpJ process steps are schematically illustrated in Figure 3.2 [8]. The process has two variants: Sleeve Plunge and Pin Plunge. In the Sleeve Plunge variant, at the first step, the rotating sleeve is driven into the upper sheet (a metal alloy in this work). It is important to note that, in FSpJ, the tool plunging occurs only in the metal part to avoid or reduce polymer degradation and damages to the fibers network, which may decrease the joint performance [8]. The friction between the sleeve and the metal part locally increases the temperature to below the melting point of the metal [9, 10]. A certain volume of the metal around the tool undergoes plastic deformation as a result of high temperature and axial movement and shearing of the tool. Simultaneously, the pin is retracted, forming a keyhole (acting as a reservoir) where the plasticized metal flows into (Figure 3.2-1). At the second step, the sleeve is retracted while the pin pushes the entrapped plasticized metal back, refilling the keyhole

formed during sleeve plunging step (Figure 3.2-2). At the end, the tool is removed and the spot joint is allowed to consolidate under pressure (Figure 3.2-3).

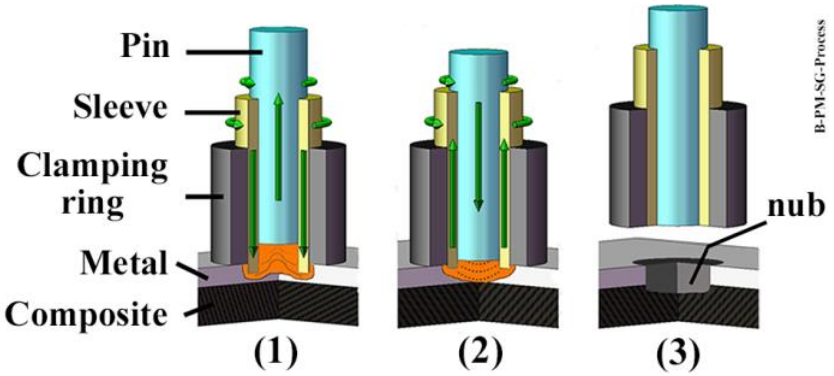

Figure 3.2 Schematic illustration of the FSpJ process steps (sleeve plunge variant) for a metal-composite hybrid structure. (1) Sleeve plunging and metal plasticizing; (2) spot refilling and (3) joint consolidation. (Adapted from [8]).

In the Pin Plunge variant, the pin is driven into the metal part while the sleeve is retracted [8]. The remaining steps of the process are similar to the Sleeve Plunge variant. Because of the larger joining area, and hence higher joint strength [8], the Sleeve Plunge variant has been more widely used. For this reason, the Sleeve Plunge variant was applied in this work.

There are four main FSpJ process parameters: rotational speed (RS), plunge depth (PD), joining time (JT), and joining pressure (JP) [36]. RS and JT are responsible mainly for the heat generation and temperature evolution during the joining process [36]. PD controls the shape and inserted volume of metal into the composite part [36]. JP defines the pressure applied during the FSpJ process to ensure intimate contact between the joining parts, and controls the flow of molten polymer at the metal-composite interface [36]. Other parameters such as clamping pressure, geometry and surface finish of the parts, as well as physicochemical and thermal properties of the materials to be joined, may also influence the joints formation [36].

In FSp metal-polymer composite joints there are two primary bonding mechanisms responsible for the joints strength: mechanical interlocking and adhesion forces [10]. During the joining process, the plasticized metal is

deformed by the tool plunging movement and creates a geometrical undercut feature, called “metallic nub” (indicated in Figure 3.3-A). The nub creates macro-mechanical interlocking between the joining parts, improving the joint strength under shear loading. In addition, micro-mechanical interlocking is established at the joints interface by the entrapment of composite polymer matrix and some of the fibers into the irregularities of the aluminum surface (see Figure 3.3-B) [10]. Furthermore, in the overlap area the frictional heat is conducted from the metal to the composite part. This creates a thin layer of molten/softened polymer matrix at the metal-composite interface. After the consolidation of the joint this layer induces adhesion forces to metal-composite interface [8]. The presence of chemical bonds between Al and composite in Al 2024-T3/CF-PPS FSp joints was recently investigated by Goushegir *et al.* [37]. X-ray Photoelectron Spectroscopy (XPS) analysis showed evidences of Al-C bond formation at the metal-composite interface induced by the joining process.

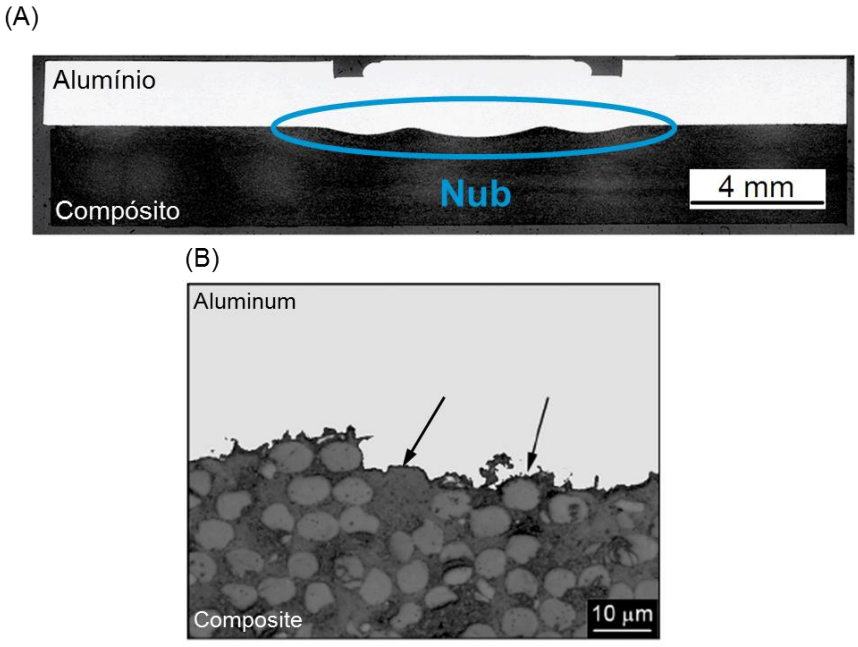

Figure 3.3 (A) A typical cross section of an FSp metal-polymer composite hybrid joint; the ellipse indicates the metallic nub formed at the interface, and (B) detail of the metal-composite interface; the arrows indicate the micro-mechanical interlocking by polymer entrapment and fiber attachment into the aluminum irregularities. (Adapted from [10]).

Moreover, three bonding zones were identified in an FSp joint as described below [10]: Plastically Deformed Zone (PDZ), Adhesion Zone (AZ) and Transition Zone (TZ). These three zones are indicated in Figure 3.4 [10].The PDZ corresponds to the center of the spot, where the metal plastic deformation takes place and the metallic nub is formed. Due to the high temperature achieved in the center of the joint, a thin layer of molten polymer matrix is formed. PDZ is the strongest part of an FSp joint because of the intimate contact between polymer matrix and fibers with the plasticized metal. The AZ corresponds to the outer region of the joint where a solid layer of reconsolidated molten polymer matrix is identified. At AZ, adhesion forces are responsible for holding the joined parts together. Further, the TZ is identified between PDZ and AZ. During the joining process, the high viscosity of the molten polymer allows the entrapment of air next to the internal border of the reconsolidated layer. Thus, the TZ is characterized by the presence of such air bubbles which may decrease the local strength of this zone [10].

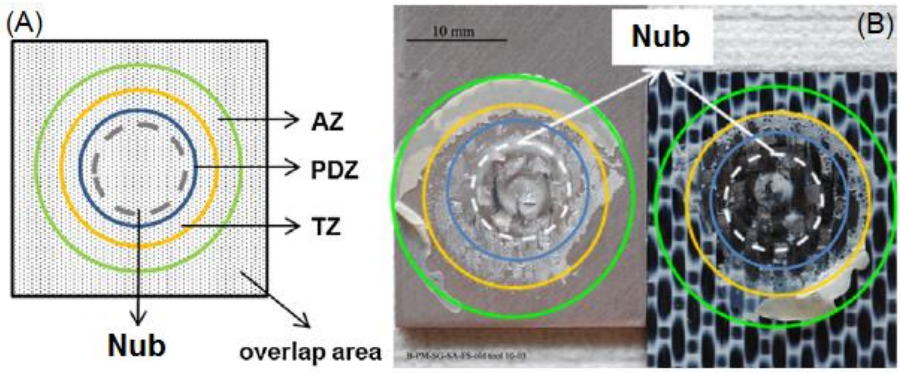

Figure 3.4 (A) Schematic illustration of a fracture surface, and (B) a real fracture surface of an FSp Al 2024/CF-PPS joint. (Adapted from [10]).

Based on the above mentioned bonding zones, Goushegir *et al.* [10] have proposed the following failure mechanism for a FSp metal-polymer composite joint submitted to shear loading. It is believed that, in FSp joints, the crack initiates at the peripheries of the AZ, propagating through the interface of reconsolidated polymer and the metal or composite surface. As the crack achieves the TZ, its path is shifted from the interface into the composite. Then,

the crack propagation occurs at the PDZ through the first plies of the composite, within a volume near to the metallic nub. As a result, part of the composite matrix remains attached to the metal surface after fracture. Therefore, the FSp lap joints typically fail in a mixture of adhesive-cohesive mode. Figure 3.5 presents the proposed mechanism for crack propagation in FSp metal-polymer composite joints under shear loading [10].

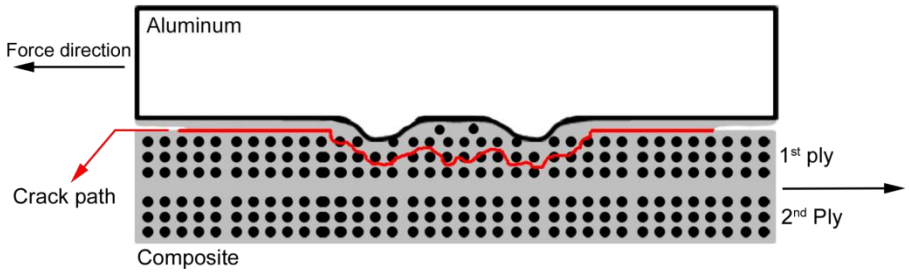

Figure 3.5 Schematically drawing of the proposed crack propagation for FSp metal-polymer composite joints under shear loading. (Reproduced with permission from [10]).

Different combinations of metal-polymer materials have been successfully joined by FSpJ.

Amancio *et al.* [8] addressed the feasibility of the FSpJ technology for AZ31-O/GF- and CF-PPS joints. They demonstrated grain refinement by dynamic recrystallization of the AZ31-O induced by the FSpJ process, whereas the PPS structure was changed by annealing. As a result, changes on the local mechanical performance of metal and composite parts were identified. Average ultimate lap shear strengths of 20 to 29 MPa were achieved for the FSp joints without surface pre-treatment of the parts.

Esteves *et al.* [38] investigated the feasibility of FSpJ of Al 6181-T4/CF-PPS joints. The authors observed a strong influence of the aluminum surface pre-treatments on the mechanical performance of the joints. The aluminum surface was ground (SiC paper, P1200) manually to remove the natural aluminum oxide layer. Additionally, grinding increased the roughness of the aluminum surface by introducing pores and crevices. This has been shown to lead to an increase in micro-mechanical interlocking between aluminum surface and polymer, improving lap shear strength of the joints. Furthermore, acid

pickling was investigated; aluminum was etched with nitric acid for 30 minutes in order to increase the wettability of the aluminum surface with the molten polymer during the joining process [39]. The joints showed lap shear strength of 11 MPa when grinding was used as the surface pre-treatment. The strength increased to 29 MPa when the etching procedure was applied.

Esteves *et al.* [9] studied the effects of the FSpJ parameters on the microstructure and mechanical performance of double lap Al 6181-T4/CF-PPS joints. Taguchi design of experiments (DoE) and analysis of variance (ANOVA) were employed. The authors found out that the rotational speed presents the largest influence on the joint strength, followed by the joining time, plunge depth and joining pressure. Higher strength of the joints was correlated to the larger extension of the bonding area and macro-mechanical interlocking (metallic nub). Larger bonding areas were achieved with higher heat input obtained through intermediate rotational speeds and longer joining times. In addition, higher macro-mechanical interlocking was obtained at larger plunge depths and intermediate joining forces.

Goushegir *et al.* [10] evaluated the microstructural features and mechanical performance of Al 2024-T3/CF-PPS FSp joints. The authors described the bonding mechanisms of the joints as macro- and micro-mechanical interlocking, and adhesion forces. Mechanical strengths up to 43 MPa were achieved with alclad aluminum specimens. In addition, their findings demonstrated that the joints have low elongation at failure (maximum 1.15 mm; 0.8% strain) under lap shear tensile testing.

In another work, Goushegir *et al.* [40] investigated the effects of joining parameters on the bonding area and mechanical performance of Al 2024-T3/CF-PPS FSp joints using full-factorial DoE and ANOVA. The authors explained that in a general trend high heat input (as a result of the selected joining parameters) increases the joining area and hence the mechanical performance of the joints.

3.3 Weld-Bonding Technology

The Weld-Bonding technology combines a welding technique with the adhesive bonding as an advanced hybrid joining technique. Such combination brings the individual advantages of each technique while simultaneously eliminating the disadvantages. Compared to adhesive bonding, increased in-plane shear strength, compressive buckling, and enhanced out-of-plane load-carrying capability and stiffness are achieved [11]. Moreover, improved load and stress distribution, and increased fatigue life and corrosion resistance of the joints are attained compared to welding [11, 12]. Weld-bonding technology has been widely applied in spaceflight and automotive industries and studied in several aspects showing improvements in joint performances, such as shear strength, stress distribution, fatigue life and durability [11, 12, 41, 42].

Ma *et al.* [43] introduced the laser spot weld-bonding (LSWB) for mild steel. The authors reported the process principles, microstructure, and the mechanical behavior of the joints. The study achieved the highest energy absorption (toughness) in tensile shear test compared with the individual laser spot welded and adhesive bonded joints.

Liu *et al.* [44] used different laser weld bonding configurations to achieve higher tensile shear strength compared to the use of individual techniques for AZ61 Mg alloy joints.

Chang *et al.* [11] compared the stress distribution in weld-bonded, spot-welded, and adhesive-bonded generic joints using finite-element method. They demonstrated that the stresses in the overlap zone of weld-bonded joints are uniformly distributed and no high-stress zones were found in weld-bonded joints. The authors concluded that the stress concentration in spot-welded joints was minimized by the use of an adhesive.

As an alternative to weld-bonding, Mitschang *et al.* [13] investigated induction welding of metal-composite hybrid joints with an additional polymeric film interlayer instead of using adhesives. $AlMg_3$/carbon-fiber-reinforced polyamide 66 (CF-PA66) and steel DC01/carbon-fiber-reinforced polyether-ether-ketone (CF-PEEK) joints were produced using 100 µm PA66 and 300 µm PEEK thermoplastic film interlayer, respectively. The addition of film was

reported to increase tensile shear strength of $AlMg_3$/CF-PA66 joint by 15% and DC01/CF-PEEK joint by 55%. Despite the preliminary investigation of the mechanical performance, the authors have not reported any deep analysis on the influence of the additional interlayer on the microstructure and bonding mechanisms of the joints.

3.4 Base Materials Literature Survey

3.4.1 Aluminum Alloy 2024-T3

The aluminum alloy 2024 was introduced by Alcoa in 1931 as an alclad (with a thin surface layer of high purity aluminum) sheet in the T3 temper. It was the first Al-Cu-Mg alloy to have a yield strength of 345 MPa and gradually replaced 2017-T4 (Duralumin) as the predominant 2xxx series aircraft alloy [45].

It is a precipitation hardenable aluminum alloy with Cu and Mg as the main alloying elements. The addition of copper and magnesium provides high strength to the alloy through pinning of dislocations. Cu element acts through solid solution strengthening, while Mg creates precipitates by natural aging [46]. Furthermore, Cu-rich intermetallic is usually distributed in the grains and its boundaries, formed during the alloy processing. The precipitates and intermetallic particles act as cathodes, raising the intergranular and exfoliation corrosion susceptibility of the adjacent areas in the alloy [47].

The T3 designation comprises a combination of solution heat treatment, cold work, and natural aging to obtain a stable condition. This treatment is applied to cold worked products mainly to improve strength after solution heat treatment and for which mechanical properties have been stabilized by room-temperature aging [48].

Table 3.1 displays some of the main properties of the Al 2024-T3 alloy.

Table 3.1 Main properties of Al 2024-T3 [45].

Property		**Value**
Mechanical/Physical	Density	2.78 g cm^{-3}
	Tensile Strength	435 MPa
	Tensile Modulus	70 GPa
	Rupture Elongation	8 – 20 %
	Hardness	137 HV 0.2
Thermal	Thermal Conductivity	121 (W m^{-1} K^{-1})
	Coefficient of Linear Thermal Expansion, 20°C	23.2 µm m^{-1} $°C^{-1}$
	Incipient Melting Point	502 °C
Processing	Annealing Temperature	256 °C
	Solution Heat Treating Temperature	495 °C

This aluminum alloy is widely used in aeronautical industry mainly due to its excellent specific strength and fatigue performance [46]. It also presents a good machinability, conformability, and surface finish capabilities. Plate products are used in fuselage structures, wing tension members, shear webs, ribs and other different structural areas where stiffness and fatigue performance are required [46]. Sheet products, usually alclad, are used extensively in commercial and military aircraft for fuselage skins, wing skins and engine areas where elevated temperatures up to 120°C are often found. Moreover, this alloy has also applications in truck wheels, screw machine products, scientific instruments and rivets [46].

3.4.2 Polyphenylene Sulfide (PPS)

PPS is a thermoplastic homopolymer consisting of linear chains [49], whose structural formula is represented in Figure 3.6.

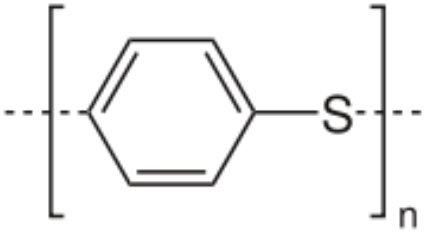

Figure 3.6 Repeat unit of PPS chain [50].

PPS has a glass transition temperature (T_g) of about 90°C, melting temperature (T_m) of about 280°C, and onset thermal decomposition temperature above 500°C [51]. PPS also offers excellent thermal stability and chemical resistance due to the combination of sulfur and aromatic ring in its backbone [52]. Furthermore, the polymer has a low moisture absorption, good mechanical properties, and high service temperature in the range of 160-240°C [52].

PPS is a semi-crystalline polymer with an orthorhombic unit cell. Its intramolecular repeating unit is defined by a planar *zig-zag* conformation of the sulfide groups, as illustrated in Figure 3.7. The dimensions of the unit cell of PPS are a = 0.867 nm, b = 0.561 nm; and c = 1.026 nm [53]. The phenyl groups are disposed alternately to the backbone plane of the crystalline structure in angles between 40-45°. This disposal of the phenyl groups restricts the mobility of the polymeric chains. Therefore, the thermal transitions of PPS occur at relatively high temperatures when compared to aliphatic polymers [54].

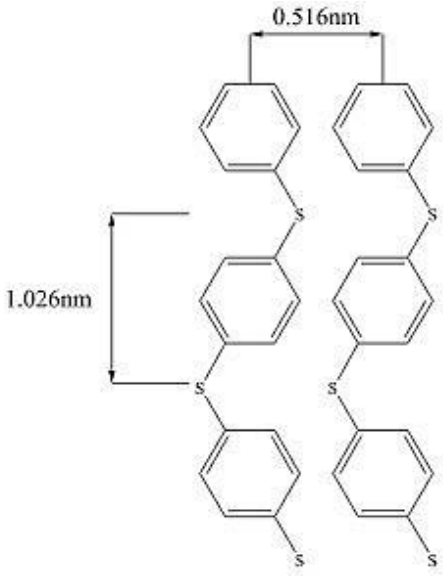

Figure 3.7 Unit cell of PPS. (Adapted from [54]).

Macroscopically, the PPS crystallization process starts with individual nuclei, and then the spherulites are radially developed. In other words, a fine structure of spherical aggregates can be formed, containing thousands of lamellar single crystals oriented in the radial direction from a core [50]. Figure 3.8 illustrates the spherulitic morphology of PPS [54].

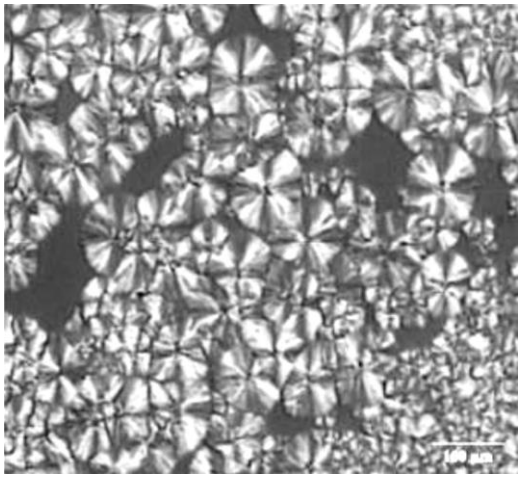

Figure 3.8 Spherulitic morphology of PPS. (Reproduced with permission from [54]).

The thermal decomposition of PPS can be divided into two stages. It initiates at approximately 500°C and up to 550°C, whereby the predominant mechanism of degradation is the random scission of the polymer chains followed by cyclization (crosslinking) [55], as shown in Figure 3.9. At temperatures higher than 550°C depolymerization mechanism (Figure 3.10) dominates the decomposition process, and the molecular weight of the polymer starts to decrease [56].

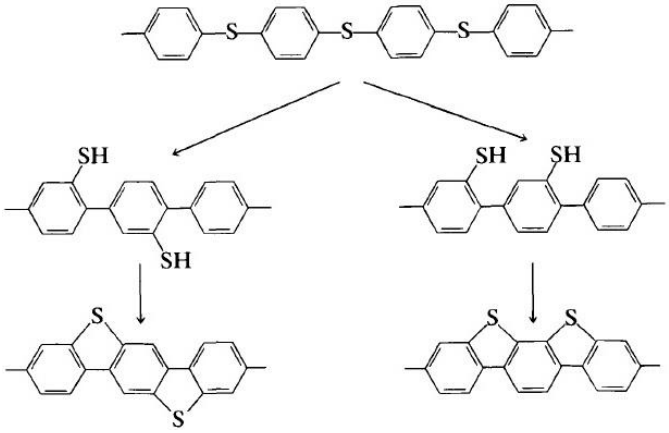

Figure 3.9 Thermal degradation of PPS: up to 550°C the random scission of the polymer chains followed by cyclization is favored. (Reproduced with permission from [55]).

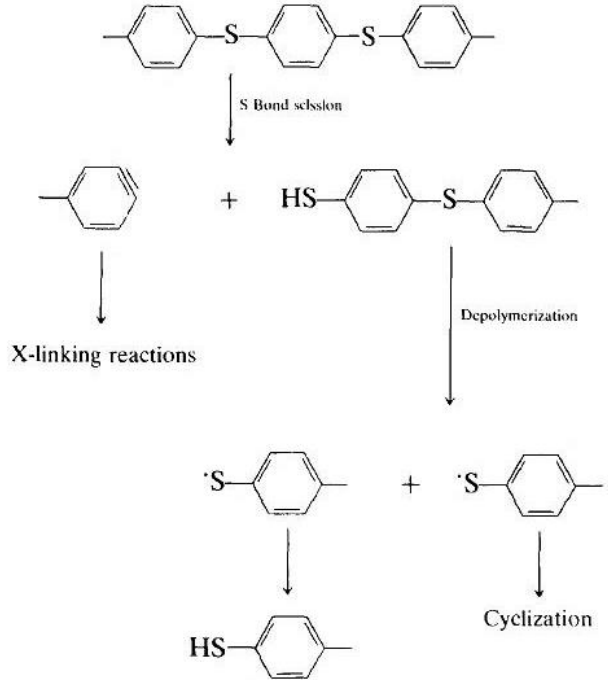

Figure 3.10 Thermal degradation of PPS: at temperatures higher than 550 °C depolymerization mechanism dominates the process. (Reproduced with permission from [56]).

Budgell *et al*. [55] investigated the thermal decomposition of PPS using pyrolysis coupled to gas chromatography and mass spectrometry. They identified - up to 550°C - the presence of cyclic tetramers, linear dimers, and trimers as a result of the cyclization mechanism of degradation. Whereas, in the range of 550-650°C there was the formation of benzothiophenes and

naftotiofenos. These are low molecular weight compounds resulted from depolymerization process of PPS.

These properties makes PPS suitable to be joined with metals using techniques such as FSpJ, where the heat transfer takes place from the metal to polymer, leading to the melting and reconsolidation of the composite matrix. In FSpJ, the heat input can be controlled in order to optimize the melting and recrystallization of the polymer. Thus, little or no significant degradation is induced in the polymeric part of the joint [36].

3.5 Surface Pre-treatments

Surface modification has been extensively explored over the years to enhance adhesion strength and durability in adhesively bonded joints [39, 57]. The influence of metal surface pre-treatments on the mechanical performance of FSp joints was also addressed by Goushegir *et al.* [10] and Esteves *et al.* [38]. In both works, it was demonstrated that the joints lap shear strength is improved when a suitable surface pre-treatment was applied on the metallic surface.

Adhesion results from two principles: mechanical interlocking between the joining parts and adhesion forces [58]. The adhesion forces can be divided into primary covalent bonds, Van der Walls forces, and hydrogen bonds [57]. Promoting adhesion in composite materials is however a challenging issue. Composites often present a very smooth surface full of contaminants (as release and bagging agents) owing to the molding process. Furthermore, most of polymers present low energy surfaces which makes the interaction with the adhesive difficult [58].

In adhesive bonding, several surface pre-treatments have been developed based on mechanical, chemical and energetic methods [58, 59].

Table 3.2 summarizes the main surface pre-treatments applied on composites prior to adhesive bonding.

Table 3.2 Surface pre-treatments commonly used for composites prior to adhesive bonding. (Adapted from [59]).

Mechanical	**Chemical**	**Energetic**
Grinding	Acid Etch	Plasma
Sandblast	Solvent Cleaning	Corona Discharge
Cryoblast	Primer	Flame
Peel Ply	Detergent Wash	Excimer Laser
Silicon Carbide		

Basically, the surface treatments act on eliminating weak layers, such as contaminants and oxides; it creates chemical modification with polar or coupling groups on the surface, which will act as available sites for chemical bonds formation. Surface treatment may also increase the surface roughness, enlarging total surface area for mechanical interlocking and intermolecular bonding. Furthermore, the surface pre-treatments can also improve the wettability of low energy surfaces [58].

Wettability is the ability of a solid to maintain contact to a liquid and describes the balance of superficial and interfacial forces [60]. The wettability can also be described as a competition between adhesive and cohesive forces. The adhesive forces between the solid and the liquid are responsible for the spreading of the liquid over the surface of the solid. The cohesive forces keep the molecules in the liquid together, avoiding the contact to the solid surface [60]. Good adhesion between the joining parts depends on ensuring an effective molecular contact between them, hence, a good wetting of the joining parts for the adhesive should be achieved [60].

The degree of wetting can be measured through the contact angle (θ) formed between the solid and the liquid, i.e, the angle which the liquid–vapor interface finds the solid–liquid interface [60]. Figure 3.11 shows three wetting possibilities for a flat and smooth solid surface in contact with a liquid drop [60].

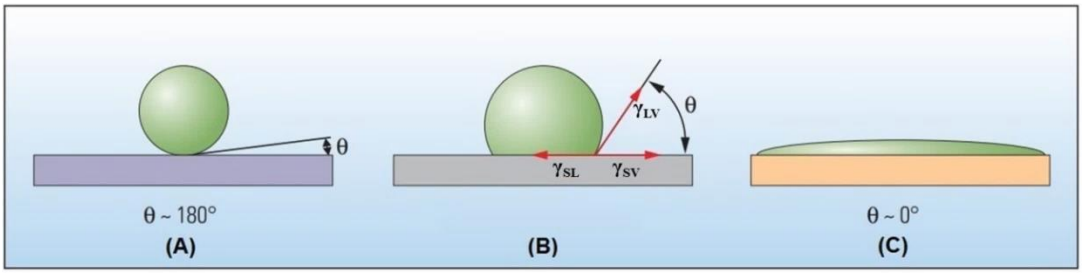

Figure 3.11 (A) Non-wettable, (B) partially wettable and (C) wettable solid-liquid interfaces. (Adapted from [60]).

Contact angle provides an inverse measurement of wettability. The tendency of a drop to spread over the solid surface increases as the contact angle decreases. Usually, a contact angle greater than 90° indicate unfavorable wetting, so the liquid will minimize contact with the surface tending to a compact spherical droplet, as displayed in Figure 3.11-A. Contact angles less than 90° indicate a favorable wetting with the liquid spreading over a large area of the surface (Figure 3.11-C). The phenomenon is described by the Young-Dupre relation (Equation 3.1) and illustrated in Figure 3.11-B, where γ_{SV}, γ_{SL} and γ_{LV} are the interfacial free energy per unit area of solid-vapour, solid-liquid and liquid-vapour interfaces, respectively, and θ is the equilibrium contact angle [61].

$$\gamma_{SV} = \gamma_{SL} + \gamma_{LV} \cos\theta \qquad \text{Equation (3.1)}$$

Mechanical surface treatments are the most simple and effective techniques to modify the surface by increasing roughness. A rough surface allows the adhesive to flow in and around the generated irregularities promoting an effective mechanical interlocking with the substrate [57]. Changes of surface energy may also occur due to the removal of material, creating sites on the substrate for chemical bonds with the adhesive [58].

It is important to point out that metallic and polymeric surfaces behave differently towards induced surface energy changes. These materials have strongly different surface energies. Polymers usually present an inherent low surface energy (10-40 dynes cm^{-1}) compared to metals (200-500 dynes cm^{-1}) [62]. Therefore, polymers present often poor adhesion without any surface pre-

treatment [62]. Although metals have higher surface energies, they are much more prone to interact with contaminants and the atmosphere. Therefore, stable oxides and hydroxides layers are formed on their surfaces immediately after the removal of material [62]. Thus, mechanical treatments may have not a huge influence on the surface energy of metals. The influence of contact area increase is pronounced in case of metals, promoting mechanical interlocking and hence the adhesion. Additionally, both modifications - surface energy and effective contact area - will influence the wettability of the surfaces [57].

Encinas *et al*. [63] tailored the wettability of HDPE, LDPE, PP and silicone through mechanical abrasion. They demonstrated a decrease in the contact angle as the surface roughness was increased.

Wingfield *et al.* [58] studied alumina grit-blasting and SiC abrasion surface treatments on CF-epoxy, CF-PEEK and GF-PP single-lap bonded joints. They reported improvements up to 440% for the bond strength of the pre-treated joints (35 MPa) as compared to the joints produced from as received polymer sheets (8 MPa).

Kim *et al.* [64] investigated the optimal mechanical pre-treatments for carbon/epoxy composite adhesive joints. They used grinding paper and also sandblasting with different sizes of corundum to modify the surface roughness of the composites. The joints have shown an increase in the peel strength from 0.8 up to 7 kN m^{-1} when an optimal roughness was achieved.

Further, energetic surface treatments, such as plasma activation, enhance the adhesion mainly due to the increase of surface energy. The plasma oxidizes the polymer surface, leading to the removal of organic contaminants and introduction of polar functional groups. Thus, more reactive and wettable surfaces are created [62]. Low pressure plasma technology is an environmental-friendly and efficient method to modify polymer surfaces. Such chemical modification occurs in the microscopic level without mechanical or chemical operations and with no changes of the bulk material properties [65, 66]. Plasma is defined as a collection of equal number of positive and negative charged particles. Basically, electrons and ions are produced in the gas phase when electrons or photons with enough energy collide with the neutral atoms

and molecules in the feed gas. There are several ways to supply the necessary energy for the collision: exothermic chemical reactions of the molecules, gas heating using adiabatic compression, and energetic beams [65]. However, the most common technological procedure of generating and supporting plasma is by applying electric field to a neutral gas, for instance, oxygen or argon [65], [66]. Surfaces in contact with the gas plasma are bombarded by these energetic species. During the collisions, their energy is transferred from the plasma to the solid surface and dissipated through several physical and chemical processes, resulting in a higher energetic modified surface. These superficial changes can achieve depths from several hundred angstroms to 10 μm without changing any bulk property of the material [65].

Kim *et al.* [64] demonstrated the effect of plasma treatment on the adhesive bonding of carbon/epoxy composite. The contact angle decreased while the surface energy increased for the plasma treated samples, indicating a more effective wetting of the surface and better adhesion between composite and adhesive.

Iqbal *et al.* [67] investigated the surface modification of high performance polymers, such as CF- and GF-PPS and PEEK, by plasma treatment and its influence on the adhesive bonding of these materials. It was demonstrated that the strength of adhesively bonded joints improved from 6 to 22 MPa due to the formation of functional groups after plasma activation.

4 MATERIALS AND METHODS

4.1 Materials

4.1.1 Aluminum Alloy 2024-T3

Aluminum alloy 2024-T3 was used as the metallic part for producing the joints. The chemical composition of the Al 2024 obtained through chemical analysis is shown in Table 4.1

Table 4.1 Chemical composition of Al 2024-T3.

Element	Cu	Mg	Mn	Si	Fe	Zn	Ti	Cr	Al
%w	4.55	1.49	0.45	0.10	0.17	0.16	0.02	≤ 0.01	Bal.

Rolled sheets of 2 mm in thickness, supplied by the Costellium (France) were used. The microstructure of this alloy in the rolling direction is shown in Figure 4.1. The grains are elongated in the rolling direction of the alloy. The black points are pores from the chemical removal of intermetallic (secondary) particles from the hardening process of the alloy through controlled precipitation. Detailed information regarding the alloy properties and applications can be found in Section 3.4.1.

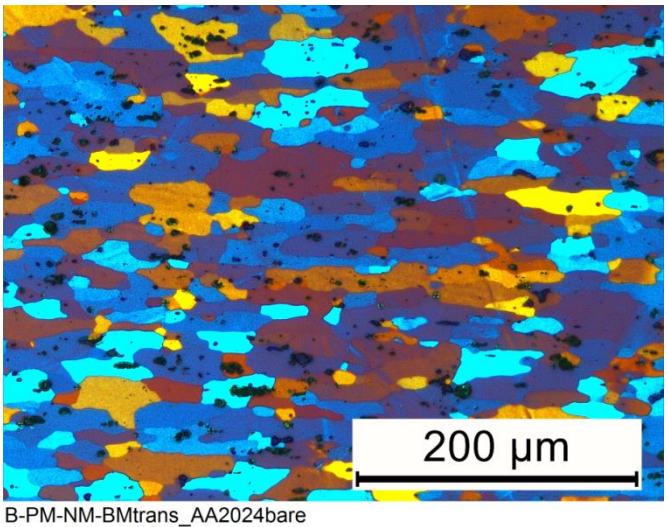

Figure 4.1 Microstructure of Al 2024-T3 parallel to the rolling direction (Keller etching, 1 mL HF, 1.5 mL HCl, 2.5 mL HNO_3 e 95 mL H_2O).

4.1.2 Carbon-Fiber-Reinforced Polyphenylene Sulfide Composite Laminate (CF-PPS)

The composite used in this study (CETEX®, supplied by Tencate, Netherlands) is a 2.17 mm thick laminate comprising an assembly of polyphenylene sulfide (PPS) reinforced with 43 wt% of carbon fiber woven fabrics in the 5H Satin configuration. Figure 4.2 shows the cross-section of CF-PPS composite laminate. This is a high-temperature, high-performance composite qualified by Airbus and Boeing for multiple structural applications, such as “J-Nose” subframe wings of Airbus A340-500/600 [4, 68].

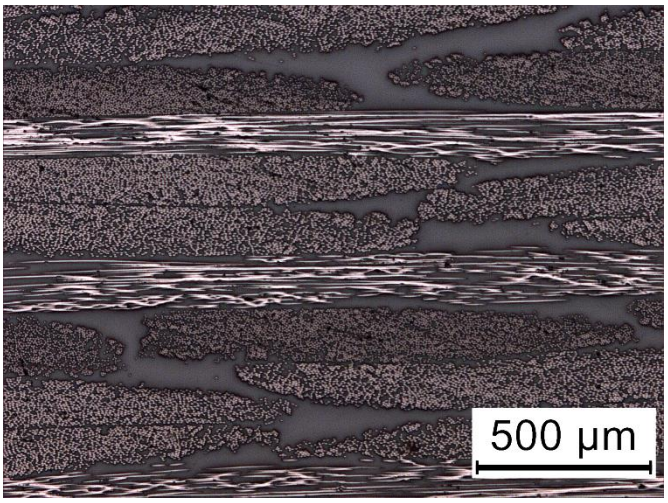

Figure 4.2 Microstructure of CF-PPS in the weft direction.

The lamination process to produce the composite is divided in four stages [68]. First, the layers of PPS and the carbon fiber fabrics are overlapped $[(0/90),(\pm45)]_3,(0/90)$ and heated from 60°C until 310°C at 5°C min^{-1} under pressure of 2 bar. At 310°C, the pressure is held at 2 bar for 30 minutes to pre-consolidate the composite. Thereafter, the pressure is raised to 10 bar for 10 minutes and the composite laminate is consolidated. At the end, the pressure is held at 10 bar while the material is cooled down to 60°C at 5°C min^{-1} [68].

Table 4.2 presents the main properties of the CF-PPS (CETEX®). The physicochemical and thermal properties of PPS combined with high mechanical strength of the carbon fibers result in a tough, rigid, chemical resistant, dimensional stable, and weldable composite laminate [68].

Table 4.2 Main properties of CF-PPS (CETEX®) [68].

Property	Value
Tensile Strength	790 MPa (Warp) / 750 MPa (Weft)
Tensile Modulus	53 GPa
In-plane shear strength	131 MPa
Thermal Conductivity	0.19 (W m^{-1} K^{-1})
T_g (glass) / T_m (melting)	120°C / 280°C
Density	1.35 g cm^{-3}

4.1.3 Polyphenylene Sulfide Film

A 100 µm thick PPS film supplied by LITE P (Austria) was employed as the interlayer polymer. This is a thermoplastic film, with low degree of crystallinity (7%) [69]. It presents high hydrolysis and chemical resistance. The main properties of PPS film used in this work are listed in the Table 4.3.

Table 4.3 Main properties of PPS film [69].

Property	Value
Tensile Strength at 23°C	85 MPa
Tensile Modulus	2.4 GPa
Thermal Conductivity	0.24 (W m^{-1} K^{-1})
T_g (glass)/ T_m (melting)	92°C / 280°C
Density	1.33 g cm^{-3}

4.2 METHODS

4.2.1 Friction Spot Joining Procedure

Single lap FSp joints of Al 2024-T3/PPS/CF-PPS were produced using displacement-controlled joining equipment (RPS 100 - Harms&Wende, Germany) in the sleeve plunge variant. The FSpJ tool used in this work was made of UHB Marax steel ESR (DIN 1.6358).

Prior to the joining, the aluminum surface which is in contact with the tool was slightly ground manually with SiC paper (P1200) to remove the natural

oxide layer. The plates to be joined were then cleaned thoroughly with acetone. The parts were positioned in the overlap configuration in such a way that aluminum was on the top, CF-PPS on the bottom and the PPS film in between. The overlap area was 25.4 x 25.4 mm^2 (Figure 4.3).

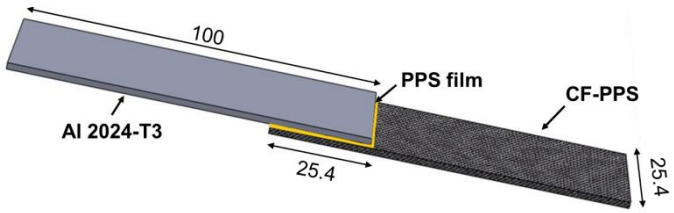

Figure 4.3 Configuration and dimensions (in mm) of the joining parts.

A special sample holder and clamping system were used to ensure an intimate contact between the parts during the joining process as shown in Figure 4.4-B and C.

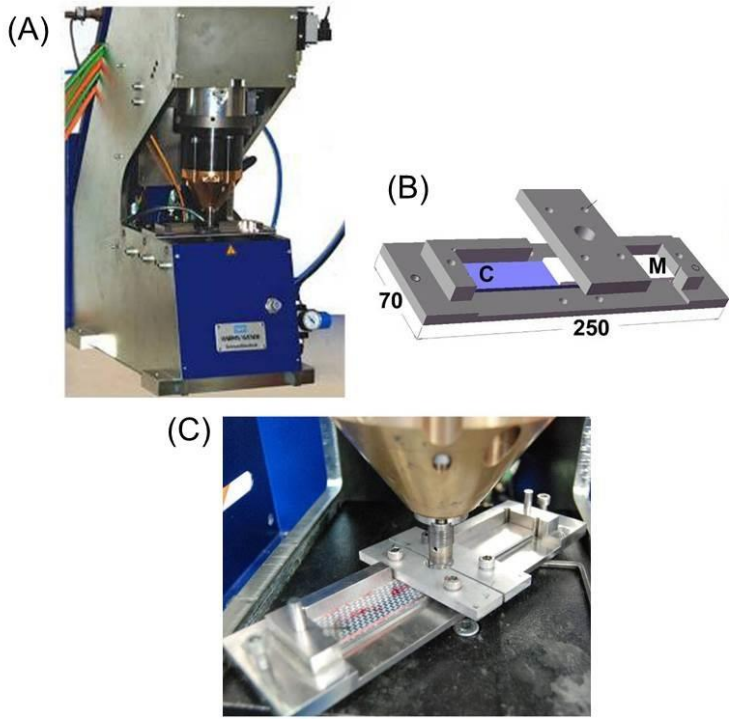

Figure 4.4 (A) RPS 100 equipment, (B) schematic illustration of the sample holder with the positions of the composite part - C and metal part – M, the interlayer is in between, and (C) joining parts and welding head of the RPS100 equipment. (Adapted from [70]).

The controllable joining parameters were tool rotational speed (same speed for sleeve and the pin), sleeve plunge depth, joining time and joining

pressure. The joining parameters in the current work were selected based on previous investigations of Al 2024-T3/CF-PPS joints without PPS film interlayer [36, 40]. Low and high heat input joining conditions were selected to evaluate the effects of heat input on the mechanical strength and microstructural features of joints with film interlayer. Table 4.4 lists the joining conditions employed in this work. The low heat input condition (L) was selected mainly due to the small amount of defects generated in the joints without film whereas the high heat input condition (H) was chosen because it produced joints with the highest lap shear strength [36]. Detailed discussion of the influence of process parameters on the frictional heat generation can be found in [9, 36, 40].

Table 4.4 FSpJ conditions used in this work.

Condition	Rotational Speed (rpm)	Plunge Depth (mm)	Joining Time (s)	Joining Pressure (MPa)
L	1900	0.8	4	0.2
H	2900	0.8	4	0.3

At the end of the joining cycle, an experimental consolidation time of two minutes (well above the required time for the PPS consolidation) was intentionally selected to avoid differential contraction of the joints due to polymer reconsolidation. In a real manufacture environment this can be reduced to a few seconds, for instance by imposing different cooling rates; details of the post-joining time optimization can be found in [71].

4.2.2 Temperature Monitoring

The temperature evolution on the aluminum surface was monitored during the FSpJ process. An infrared thermo-camera (High-end Camera Series ImageIR, Infratech GmbH, Germany) set in the range of 150°C-700°C with a data acquisition frequency of 20 Hz was used for this purpose. The set up for the thermography is schematically illustrated in Figure 4.5. An example of a snapshot of the peak temperature obtained during the process is shown in the figure. The maximum process temperature was taken as the highest temperature measured on the aluminum surface.

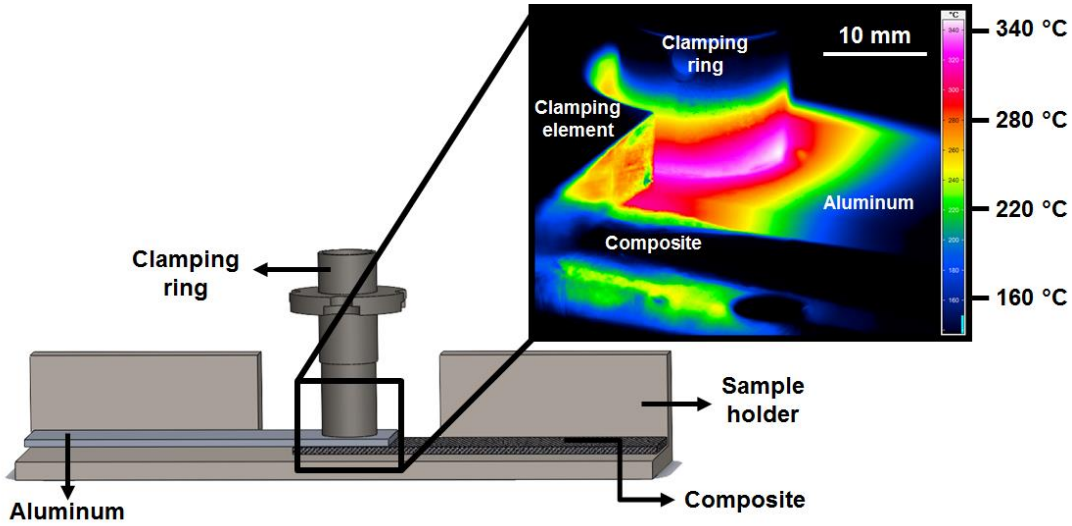

Figure 4.5 Set up for the measurement of temperature evolution during FSpJ using an infrared camera and an example of a snapshot showing the maximum process temperature on the surface of the aluminum.

4.2.3 Thermal Analysis

Differential Scanning Calorimetry (DSC) analysis was performed with a TA Instruments model Q100 equipment at DEMa/UFSCar based on ASTM D 3418-08 standard guidelines. The samples of CF-PPS and PPS film were carefully extracted from fractured joints from the regions indicated in Figure 4.6. Samples weighting approximately 9-10 mg with precision of ± 0.01 mg were used. Aluminum crucibles were used as sample holder. The experiments were carried out under nitrogen atmosphere with a flow rate of 50 mL min^{-1}. The temperature was stabilized at 25°C and then raised to 350°C at the rate of 10°C min^{-1}. The samples were hold for 3 minutes at 350°C to ensure a complete melting of the crystallites and then cooled down to 25°C at 10°C min^{-1}. DSC was applied to determine the enthalpy of fusion (ΔH_f) as well as the glass transition (T_g), melting (T_m), and crystallization (T_c) temperatures of the CF-PPS and the PPS film extracted from the joints. The polymeric base material samples were also analyzed for comparison. Three replicates were used for each joining condition and base material.

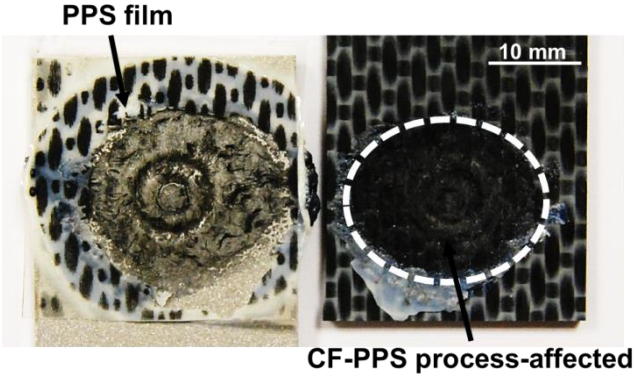

Figure 4.6 Fracture surface of FSp joints indicating the regions from where CF-PPS and PPS film samples were extracted for thermal analysis.

The crystallinity degree (X_C) of PPS in the samples was calculated according to Equation 4.1 [72].

$$Xc = \frac{\Delta H_m - \Delta H_{cc}}{\Delta H_m^0 (1 - W_f)} \qquad \text{Equation (4.1)}$$

where:

ΔH_m: enthalpy of fusion (J g^{-1})

ΔH_{cc}: enthalpy of cold crystallization event that takes place at around 120°C during the heating (J g^{-1}) [73]

ΔH^0_m: enthalpy of fusion for 100% crystalline PPS = 150.4 J g^{-1} [68]

W_f: weight percentage of carbon fibers in the sample

Thermogravimetric Analysis (TGA) was performed using a TA Instruments model Q50 equipment at DEMa/UFSCar based on ASTM E 1131–08 standard guidelines. Samples of the PPS film and CF-PPS composite weighting between 12 and 15 mg with a precision of ± 0.01 mg were extracted from the joints (in the regions indicated in Figure 4.6) and the base materials. Platinum crucibles were used as sample holder. The experiments were carried out under nitrogen atmosphere with a flow rate of 90 mL min^{-1}. Samples were heated from room temperature to 800°C at 20°C min^{-1}. The onset temperatures of mass loss were determined using the tangent method. The maximum rates of mass loss were determined by the derivative of the TG curve (DTG). Three replicates were used for each joining condition.

Analysis of Variance (ANOVA) was applied to statistically evaluate the DSC and TGA responses through comparisons of variances and means. Changes in T_g, T_m, degree of crystallinity, supercooling and possible thermo-mechanical degradation in the polymeric components of FSp joint were investigated. The results were compared to the respective base material. The software *Minitab® 16* was employed to perform the statistical analysis.

4.2.4 Microstructural Analysis

Interface Analysis

The joints were cut close to the middle of the spot, parallel to the aluminum rolling direction using a low-speed saw with diamond blade. The samples were then embedded in cold curing epoxy resin (Epoxycure) followed by standard grinding and polishing materialographic procedures. The cross-section of the joints was analyzed using an optical microscope (OM) (DM IR microscope, Leica, Germany) under reflective light. Interfacial features such as micro-mechanical interlocking as well as defects induced during the joining process were examined.

Microstructural Analysis

The cross-section of the joints was etched in order to reveal the microstructure of the aluminum after the joining process. Keller reagent (1 mL HF, 1.5 mL HCl, 2.5 mL HNO_3 e 95 mL H_2O) was employed. The etched samples were analyzed through OM (DM IR microscope, Leica, Germany).

4.2.5 Local Mechanical Properties

Hardness measurements were performed to study the influence of FSpJ process on the local mechanical properties of the parts in the joined area.

The hardness of the aluminum part was measured using a Zwick/Roell-ZHV microhardness equipment at Helmholtz-Zentrum Geesthacht, Germany. The analyses were conducted based on ASTM E384-10 standard procedure. A series of indents were performed on half of the specimen (from the edge of the joint to the middle of the spot) since the joints are symmetrical. An indentation

force of 1.96 N (200 g) was applied for 10 s. The distance between indentations was 0.3 mm. The analyzed region is schematically illustrated in Figure 4.7-B. By the analysis of the indents, an aluminum hardness map was obtained.

For the composite part, nanohardness measurements were conducted. The presence of carbon fibers as well as defects close to the interface with the aluminum makes it difficult to obtain reliable measurement through microhardness method, which in turn would result in very large indentations. Different regions across the joint were carefully selected to perform nanohardness. Three indentations were conducted in each region. A force of 10 mN was applied for 30 s with a loading rate of 30 mN min^{-1}. Figure 4.7-C schematically illustrates the position of the indents (green solid circles). The measurements were carried out with a Nanovea equipment at the Materials Engineering Department of USP-São Carlos.

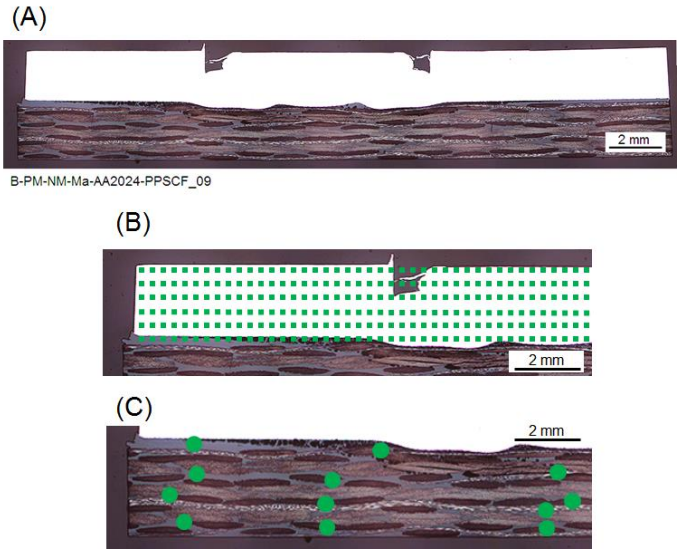

Figure 4.7 Cross-section of a joint (A) showing the schematics details of the indents in (B) for aluminum and (C) composite parts.

4.2.6 Surface Preparation

Surface pre-treatments on both aluminum and composite were carried out in order to enhance the adhesion between the joining parts.

Aluminum and composite were cleaned followed by surface pre-treatments prior to joining process. For the aluminum, only sandblasting was

performed based on the successful past investigations [10]. In case of the composite, three different pre-treatments were applied: mechanical grinding, sandblasting and plasma activation. Details of the performed surface pre-treatments are described as follow.

Aluminum

Sandblasting was carried out using a Normfinish® equipment (Holland) at HZG. Corundum (Al_2O_3) with average particles size of 100-150 µm was employed as the blasting medium. The distance between the samples and the pistol was fixed at 20 cm. The angle between the aluminum surface and the pistol was 45°. The sandblasting was applied for 10 seconds with a pressure of 0.6 MPa.

Composite

A set of composite samples was ground manually in 0°, 90° and ±45° directions. Two SiC papers were used to perform mechanical grinding on the composite surfaces: P320 and P1200.

Another set of composite samples was sandblasted. Two angles between the surface and the pistol were tested: 90° and 45º. In case of blasting angle of 90º, the blasting time was 5 or 10 s. In case of blasting angle of 45° the blasting time was 5 s to avoid excessive removal of the composite matrix. A blasting pressure of 0.3 MPa was applied to avoid excessive damage of the carbon fibers. The equipment, the blast medium and the distance between samples and the pistol were the same employed for aluminum samples.

The surface pre-treated specimens were then cleaned with compressed air followed by ethanol cleaning in an ultrasonic bath for 3 minutes. This was performed to remove debris and particles from the mechanical pre-treatments.

In addition, a set of sandblasted composite samples sandblasted at 45° was subsequently plasma-treated. Low pressure plasma pre-treatment was performed at Hamburg University of Technology (TUHH), Germany. The power and the pressure were set at 100 W and 0.5 mbar, respectively. Oxygen was used as the chamber gas. Two different treatment times were tested: 5 and 10

minutes. In this case, a set of PPS films was also plasma-treated with the identical parameters used for the composite.

Table 4.5 summarizes the surface pre-treatments carried out on the joining parts.

Table 4.5 Summary of surface pre-treatments on the joining parts.

Material	**Surface Pre-treatment**	**Symbol**	**Parameters**
Aluminum	Sandblasting	S1	Al_2O_3, 100 – 150 µm, 20 cm distance, 45°, 10 s, 0.6 MPa
Composite	Sandblasting	S2	Al_2O_3, 100 – 150 µm, 20 cm distance, 90°, 5 s, 0.3 MPa
		S3	Al_2O_3, 100 – 150 µm, 20 cm distance, 90°, 10 s, 0.3 MPa
		S4	Al_2O_3, 100 – 150 µm, 20 cm distance, 45°, 5 s, 0.3 MPa
	Mechanical Grinding	M1	P1200, 0°/90°/±45°
		M2	P320, 0°/90°/±45°
	Plasma Activation	S4 + P1	S4 + O_2, 100 W, 0.5 mbar, 5 min
		S4 + P2	S4 + O_2, 100 W, 0.5 mbar, 10 min

4.2.7 Surface Characterization

The surface of the specimens after pre-treatments and prior to joining procedure were analyzed as described in the following.

Surface Roughness Analysis

The pre-treated surfaces of the joining parts were analyzed with a Laser Scanning Confocal Microscope (Keyence, Japan) at HZG. The roughness of the

pre-treated surfaces was evaluated based on EN ISO 25178-2 standard in order to correlate the mechanical performance of the joints with the surface features of the joining parts.

The arithmetic average surface roughness parameter (R_a) was calculated from three different areas on each surface. Five randomly treated samples were examined per surface pre-treatment. The average of the 15 measured values was taken as the average surface roughness for each surface pre-treatment.

Contact Angle Measurements

The sessile drop method was applied to measure the static contact angle of the pre-treated surfaces. The main premise of the method is to place a droplet of a pure liquid on a static solid substrate [74]. A high resolution camera is used to capture the profile of a liquid drop on a solid substrate.

For this purpose, a Krüss DSA 100 equipment (Germany) at HZG was employed. The measurements were performed using a water droplet with volume of 10 µL on the pre-treated composite surfaces. The contact angle was measured from each area after approximately 30 s to stabilize the water droplet. Three different areas were investigated. The average of the measured values of the three areas was considered as the average contact angle for each surface pre-treatment.

X-ray Photoelectron Spectroscopy (XPS)

XPS technique was employed for identification of functional groups generated on the surface of CF-PPS composite and PPS film parts after plasma activation. The analyses were performed at HZG using a Kratos DLD Ultra Spectrometer operated at 225 W under ultrahigh vacuum using a monochromatic Al-Kα X-ray as the excitation source.

4.2.8 Global Mechanical Properties

The mechanical performance of the single lap shear joints under static loading was evaluated through lap shear testing under tensile loading based on the ASTM D3163-01 standard guidelines. The tests were performed at HZG

using a universal testing machine Zwick/Roell 1478 with a cell load capacity of 100 kN, cross-head speed of 1.27 mm/min, at room temperature. Specimens of 100 x 25.4 mm^2 with 25.4 mm^2 overlapped area were used (Figure 4.3). Three replicates were tested for each joining condition. The average value of ultimate lap shear force (ULSF) of the three measurements was taken as the lap shear force of the joints. To calculate the strength, the nominal joining area of the joints was considered as the area circumscribed by the external sleeve diameter (9 mm). The tool area is commonly used to estimate the bonded area of the joints produced by other techniques such as ultrasonic welding [29].

Fatigue experiments were carried out in order to evaluate mechanical performance of the single lap joints under dynamic loading. The experiments were performed using MTS Bionix® equipment at DEMa/UFSCar. The fatigue life of the joints was investigated under load levels corresponding to 35%, 50% and 75% of the respective lap shear strength. A frequency of 5 Hz and load ratio of R = 0.1 (tension-tension) were used. This ratio is usually selected to evaluate the fatigue life of aircraft structures. Three replicates per joining condition were tested to obtain the S-N curve for each joining condition. Single lap shear configuration similar to those illustrated in Figure 4.3 was used for fatigue experiments. The fitting procedure to obtain the S-N curves was established through the exponential model (lin-log model) based on ASTM E739-10 standard procedure. Details of the fitting procedure are described in Appendix A.

The joints surviving one million cycles without failure were subsequently tested under lap shear testing to evaluate their residual strength using a MTS Bionix® equipment according to the procedure described previously in this section.

4.2.9 Hydrothermal Accelerated Aging

Hydrothermal accelerated aging was used to evaluate the influence of harsh environments, i.e., the combination of high temperature and humidity on the joints mechanical performance. The accelerated aging was carried out in a closed chamber (ATLAS BCX equipment) with 100% relative humidity at 71°C

for 7 days (short term) and 28 days (long term) based on ASTM D3762. These analyses were performed at Hamburg University of Technology (TUHH). The weight of the joints was measured before and after the aging to evaluate the moisture absorption. Lap shear testing according to the procedure described in the Section 4.2.8 was used to evaluate the residual mechanical strength of the joints after hydrothermal accelerated aging.

4.2.10 Fractography

To understand the failure micro-mechanisms of the joints under shear loading, fracture surfaces were analyzed through Scanning Electron Microscopy (SEM) (FEI, QUANTA FEG 650). To analyze the fracture surfaces, accelerating voltage of 10 kV, spot size of 3 and working distance of 15 mm were used. The samples were sputter coated with a thin layer of gold prior to SEM examination.

5 RESULTS AND DISCUSSION

5.1 Temperature Evolution

The process temperature was monitored on the aluminum surface in the joining area during the FSpJ process, as schematically shown in Figure 4.5. Figure 5.1 demonstrates the process temperature evolution on the surface of aluminum for the joints produced under low (L) and high (H) heat input conditions.

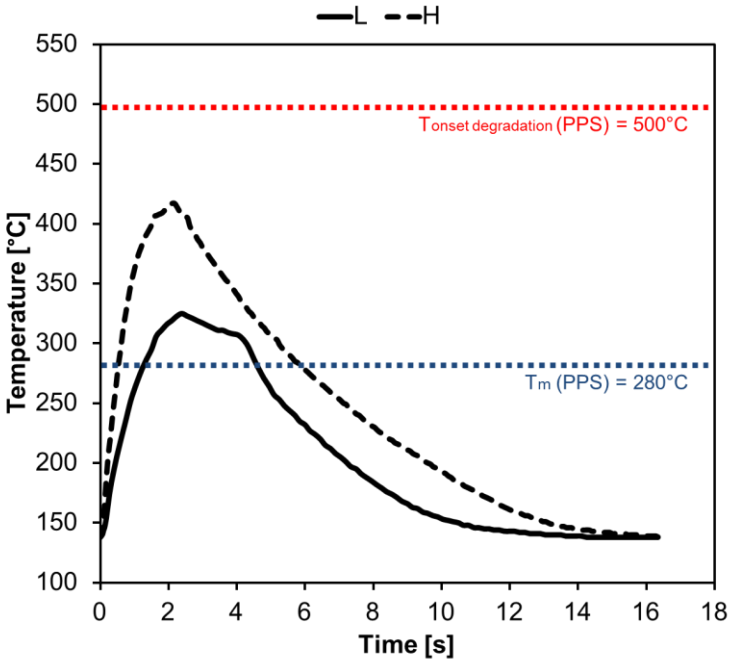

Figure 5.1 Process temperature evolution on the surface of aluminum for low heat input (L) and a high heat input (H) joints. The temperatures of the onset of thermal degradation and melting point of PPS matrix are schematically shown in the figure.

The average peak temperature identified on the aluminum surface was 325°C for the low (L) heat input condition, and 417°C for the high (H) heat input condition. The peak temperatures measured on the surface of the aluminum for the L and H conditions represent, respectively, 65% and 83% of the incipient melting point of the Al 2024-T3 [45] . As discussed by Amancio *et al.* [75] the aluminum is dynamically recrystallized in the spot area due to the high tool rotational speed and temperature during the FSpJ process. The microstructural

effects induced for the joining process in the joining parts will be discussed in Section 5.4.

Furthermore, the obtained peak temperatures are above the melting point of the PPS matrix of the CF-PPS and the PPS film (T_m = 280°C). As a result of the high process temperature, the PPS film and a thin layer of the PPS composite matrix were melted during the joining process in a volume around the tool. After reconsolidation, this layer provides adhesion forces between the joining parts, as will be discussed in Section 5.3.

Moreover, the identified process temperatures (maximum 417°C) are below the onset temperature for PPS degradation (crosslinking at 500°C) [76]. Therefore, extensive thermal degradation of PPS during the FSpJ process is not expected to occur in such conditions. The process-related physicochemical changes of the polymeric parts will be discussed in Section 5.2.

5.2 Process-Related Physicochemical Changes of Polymeric Parts

The physicochemical changes of the polymeric parts induced by the FSpJ process were investigated through DSC and TGA analysis. The understanding of the physicochemical alterations of the polymeric joining parts is important because these changes may influence the local and global mechanical performance of the joints. This is particularly important in case of FSp joints, because the failure occurs usually in the polymer composite at the overlapped interface [10].

5.2.1 Degree of Crystallinity and Transition Temperatures

Figure 5.2 shows examples of DSC curves of samples extracted from CF-PPS composite laminate and PPS film. Data from base materials and FSp joints produced with high heat input (H) and low heat input (L) conditions are presented. Table 5.1 displays the average glass transition temperature (T_g), degree of crystallinity (X_c), melting temperature (T_m), crystallization temperature (T_c) and supercooling degree ($T_m - T_c$) obtained from the DSC curves.

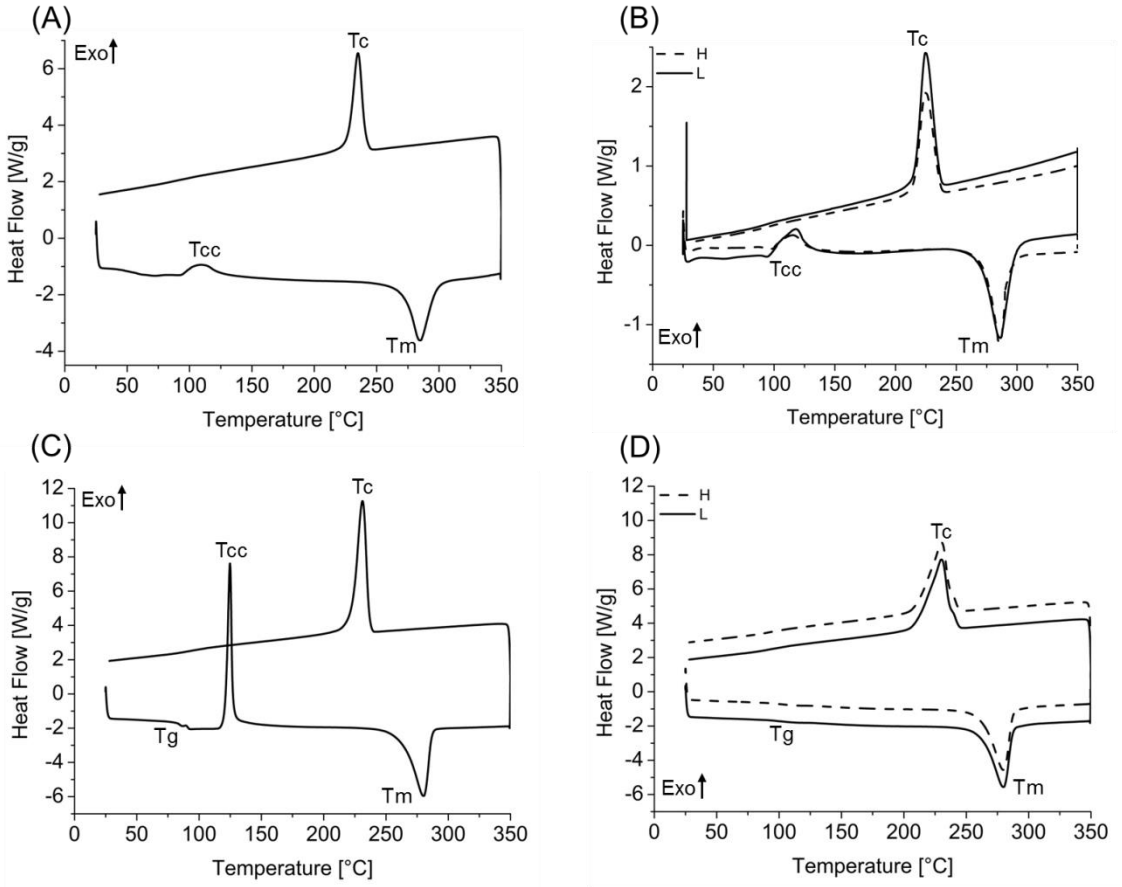

Figure 5.2 Examples of DSC curves of the base materials and the joint samples, respectively in (A) and (B) for CF-PPS and (C) and (D) for PPS film. The transition temperatures are indicated.

Table 5.1 Thermal properties obtained by DSC analysis for samples of CF-PPS and PPS film extracted from base materials and joints.

Sample	CF-PPS				PPS film				
	X_c [%]	T_m [°C]	T_c [°C]	$T_m - T_c$ [°C]	T_g [°C]	X_c [%]	T_m [°C]	T_c [°C]	$T_m - T_c$ [°C]
Base Material	22±3	285±1	232±1	53±3	91±1	7±1	280±1	226±5	54±5
L	18±2	285±1	230±1	55±1	99±1	26±2	280±1	228±2	53±3
H	12±2	285±1	232±2	54±2	102±4	27±1	280±1	221±4	59±5

The CF-PPS samples extracted from the joints presented lower values of degree of crystallinity (X_c) - 18% and 12% for, respectively, low (L) and high (H) heat input joining conditions - as compared to the base material (X_c = 22%).

The analysis of the process temperature discussed in Section 5.1 demonstrates that the joints underwent a rapid cooling rate of approximately 1145°C min^{-1} and 1300°C min^{-1}, for the L and H conditions, respectively. Calculations are shown in Appendix B. These cooling rates are much faster than the cooling rate applied during the manufacturing process of CF-PPS (5°C min^{-1} [68]). Thus, the PPS in the joint has a lower degree of crystallinity due to the shorter time available for crystallization during the FSpJ process [73].

Furthermore, thermal curing of PPS may be induced by the manufacturing process of the composite. As described in Section 4.1.2, the PPS experienced 30 min under 310°C during the pre-consolidation of the composite [68]. Port *et al.* [77] reported the crosslinking of a 1 mm thick PPS film at 300°C demanded 1 hour. Therefore, the PPS matrix may be partially crosslinked during the manufacturing process. The network of PPS chains may impair the macromolecules mobility and makes the reorganization of the chains into the crystalline structure difficult during the cooling phase. In addition to the high cooling rates applied, it may cause a lower degree of crystallinity for the composite samples after the joining process.

The supercooling of CF-PPS samples from the joints showed slightly higher values than the base material. It is important to note that the increase in supercooling of the joints is due to the decrease of T_c values, whereas T_m values remained virtually constant in comparison to the base material. The relevance and influence of this variable will be discussed later in this section.

The T_g of the PPS in the CF-PPS composite showed a high temperature of 120°C which overlaps the peak of cold crystallization of PPS [68]. This makes the analysis of variation in T_g difficult and therefore it was not evaluated for the CF-PPS in this study.

Statistical analysis was carried out to evaluate the significance of the variation in the degree of crystallinity and supercooling of CF-PPS samples from the joints and base material. For this purpose, the Analysis of Variance (ANOVA) and the Tukey test were used. Additional information about these statistical analyses can be found in Appendix C. The results of the statistical analysis are presented in Table 5.2.

Table 5.2 ANOVA and Tukey test for CF-PPS (confidence level of 95%).

Specimen	**X_c** **p = 0.025**		**Supercooling** **p = 0.177**
Base Material	A		A
L		B	A
H		B	A

The ANOVA for the degree of crystallinity (X_c) was performed with a confidence level of 95% (i.e., α = 0.05). The p-value obtained according to ANOVA was 0.025. A p-value less than α means that the selected response (in this case changes in X_c) is statistically significant. Further, the Tukey test was applied showing that the samples are divided into two groups (Table 5.2). The variation of degree of crystallinity is statistically significant between the CF-PPS base material and the joints, because they do not share identical letters [78]. However, among the FSpJ conditions the variation is not statistically significant. This means that the degree of crystallinity is significantly affected by the FSpJ process, which induces a decrease of the degree of crystallinity in the CF-PPS composite. However, the different heat inputs (L or H) applied during the FSpJ is not an influential parameter on this property of the CF-PPS in the studied process parameter range.

Statistical analysis was also applied to evaluate the significance of changes in the supercooling degree of CF-PPS samples from base material and joints. According to ANOVA a p-value of 0.177 (larger than α = 0.05) was obtained. Further, the Tukey test resulted in identical letters for the base material and the joints (Table 5.2). Therefore, it is concluded that there is no statistically significant variation in the supercooling of the CF-PPS samples in the base material and the joints. This means that the FSpJ process did not adversely influence this property.

The supercooling phenomenon states the additional energy required to precipitate crystal nuclei during the cooling of the molten polymer [50]. Higher values for supercooling of the CF-PPS from the joints would be associated to the crosslinking of PPS induced by FSpJ process, which is the main

degradation mechanism of PPS until 550°C [55, 76]. The formation of a network of PPS chains would impair the chain mobility and makes the reorganization of the chains into the spherulitic structures difficult during the cooling phase [50]. This means higher energy would be required for crystallization, which would lead to higher supercooling degree. On the other hand, degradation by chain scission, which is the main degradation mechanism of PPS above 550°C [55, 76], would decrease the supercooling degree, since shorter chains have higher mobility and crystallize faster. Additionally, if any kind of degradation had occurred, changes in the T_m values would be also expected. However, it is worth to note that the T_m of the CF-PPS samples extracted from the joints remained virtually constant in comparison to the base material (Table 5.1).

Therefore, the statistical similarity between the values of T_m, T_c and supercooling (T_m – T_c) indicates that no evidence of extensive thermo-mechanical degradation of PPS in the CF-PPS composite neither by crosslinking nor chain scission have occurred in the FSpJ conditions adopted in this study. This agree with the study of Port *et al.* [77], who demonstrated that at temperatures as high as 450°C the crosslinking of a 1 mm thick film would demand 30 minutes. Considering that the FSpJ process lasts just few seconds (4 s in this work) and the process temperature are below 450°C, the occurrence of crosslinking is an outlying hypothesis. Additionally, Port *et al.* [77] reported that the crosslinking of PPS, also known as thermal curing, improves the physical properties of the polymer. Thus, the occurrence of PPS crosslinking during FSpJ would not represent harm for the mechanical performance of the joints.

The PPS film from the base material presented a peak of cold crystallization (T_{cc}) at approximately 120°C, which was not identified for the film extracted from the joints (Figure 5.2-C and D). The degree of crystallinity of the film base material was 7 ± 1% (Table 5.1). The PPS films extracted from the joints demonstrated a higher degree of crystallinity of 26 ± 2% and 27 ± 1%, respectively, for the low (L) and high heat (H) input conditions (Table 5.1). These values suggest that the PPS film was crystallized during the FSpJ process, as the parts were subjected to the heating-cooling cycle. The PPS film

interlayer - initially with a low degree of crystallinity - undergoes cold crystallization and melting during the heating phase of the joining process. As a semi-crystalline polymer, the PPS film recrystallizes during the cooling phase, even under the high cooling rate experienced. Nohara *et al.* [54] demonstrated the presence of PPS crystals at temperatures up to 340°C, though the melting temperature of PPS is reported in the range of 280-285°C. Therefore, the presence of crystals that were not completely melted during the fast FSpJ cycle (4 s) may act as nucleation sites, supporting the recrystallization of the PPS film. This might be the reason that the PPS film after FSpJ showed a substantially greater degree of crystallinity than the base material.

ANOVA and Tukey test were applied to statistically evaluate the variation in the degree of crystallinity (X_c) among the PPS film in the base material and in the joints. The results of the statistical analysis are shown in Table 5.3. Considering the confidence level of 95%, ANOVA stated that the variation of the degree of crystallinity among the specimens was statistically significant (p-value = 0). The Tukey test concluded that the degree of crystallinity of the PPS film in the joints is significantly higher than the base material, since they do not share identical letters. On the other hand, the variation is not significant among the joining conditions. This means that the degree of crystallinity of the PPS film was not affected by different heat inputs applied during FSpJ studied in this work.

Table 5.3 ANOVA and Tukey test for PPS film (confidence level of 95%).

Specimen	**X_c** **p = 0**		**T_g** **p = 0.137**	**Supercooling** **p = 0.968**
Base material	A		A	A
L		B	A	A
H		B	A	A

As a consequence of increasing the degree of crystallinity of the PPS film in the joints, an increase of up to 11°C in the T_g was observed compared to the base material (see Table 5.1). An increase in the crystalline phase of the PPS constrains the movement of PPS chains in the amorphous phase. Thus, the

energy required for the mobility of the chains is increased. Therefore, a higher glass transition temperature will be observed in such cases [50]. The temperatures of melting (T_m), crystallization (T_c) and the supercooling (T_m - T_c) of the PPS film of the joints remained practically unchanged compared to the base material (Table 5.1).

The glass transition temperature and the supercooling degree of the PPS film in the joints were compared to the base material values through ANOVA and Tukey test. From Table 5.3, no statistically significant variation was identified among the specimens of PPS film from the base material and both joints. Therefore, the FSpJ process did not influence T_g, T_m and supercooling degree (T_m - T_c) of the PPS film. This indicates that no evidence of extensive thermo-mechanical degradation of PPS film was observed in the FSpJ conditions adopted in this work, as shown earlier for the CF-PPS.

5.2.2 Thermo-Mechanical Degradation

Thermogravimetric analysis (TGA) was performed on samples of CF-PPS composite and PPS film extracted from the base materials and FSp joints produced under high heat input (H) and low heat input (L) conditions. Figure 5.3 depicts examples of TGA curves for (A) CF-PPS and (B) PPS film. The onset temperature and the maximum rate of mass loss were evaluated by plotting DTG curves. Table 5.4 summarizes these results.

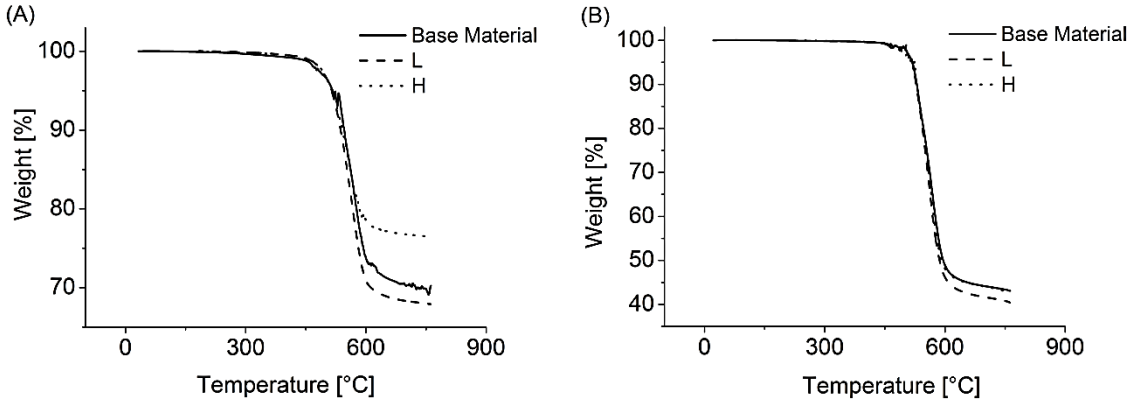

Figure 5.3 Example of TGA curves for samples of (A) CF-PPS; and (B) PPS film extracted from base material and an FSp joint. The base material curve overlaps the H curve in B.

Table 5.4 Thermal properties obtained by TGA and DTG for samples of CF-PPS and PPS film extracted from the base materials and the joints.

Specimen	CF-PPS		PPS film	
	Onset temperature of mass loss [°C]	Maximum rate of mass loss [%/°C]	Onset temperature [°C]	Maximum rate of mass loss [%/°C]
Base material	520±2	0.4±0.1	521±2	0.7±0.1
L	514±1	0.4±0.1	521±2	0.8±0.1
H	519±3	0.3±0.1	523±2	0.8±0.1

The onset temperature of mass loss for CF-PPS obtained in this work (above 500°C) is in agreement with those reported in the literature [55]. The onset temperature of mass loss slightly varied for the CF-PPS and PPS film samples from the joints in comparison to the respective base materials. A statistical evaluation was conducted using a confidence level of 95% ($\alpha = 0.05$). ANOVA resulted in p-values of 0.284 and 0.422 in case of CF-PPS and PPS film, respectively (Table 5.5). Therefore, the onset temperature of mass loss of both composite and film interlayer from the joints and respective base materials did not show any statistically significant variation. Similar results were observed for the maximum rate of mass loss. P-values of 0.063 and 0.471 were obtained through ANOVA for the composite and the film, respectively. Therefore, statistically significant differences were not identified for the composite and the film from the joints and respective base materials (Table 5.5). Finally, the highest average process temperature achieved (417 °C for the high heat input condition - Section 5.1) was still much lower than the onset temperature of mass loss measured for CF-PPS and PPS film. Therefore, based on the TGA and statistical analyses, no evidence of extensive thermo-mechanical degradation induced by the FSpJ was observed, which agrees with DSC results (Section 5.2.1).

Table 5.5 ANOVA and Tukey test for CF-PPS and PPS film samples (confidence level of 95%).

Specimen	CF-PPS		PPS film	
	Onset temperature p = 0.284	**Maximum mass loss rate max p = 0.063**	**Onset temperature p = 0.422**	**Maximum mass loss rate max p = 0.471**
Base material	A	A	A	A
L	A	A	A	A
H	A	A	A	A

5.3 Analysis of Joint Interface

This section presents the analysis of a joint interface produced under low heat input as a representative example of the FSp joints with interlayer. The joint produced under high heat input condition has similar characteristics and it is presented in Appendix D. For this analysis, sandblasting was selected as surface pre-treatment (S1 for aluminum and S4 for composite, refer to Table 4.4).

Figure 5.4 shows (A) the top view of a sound Al 2024-T3/CF-PPS FSp joint with PPS film interlayer along with (B) the cross sectional microstructure in the spot area. The metallic nub, a slight insertion of the aluminum into the composite part in the form of an undercut, is highlighted by an ellipse in Figure 5.4-B. The nub is responsible for the macro-mechanical interlocking between the joining parts, which contributes to the joint strength under shear loading, as also reported by Goushegir *et al.* [10], Esteves *et al*. [9], Amancio *et al.* [8] and André *et al.* [35].

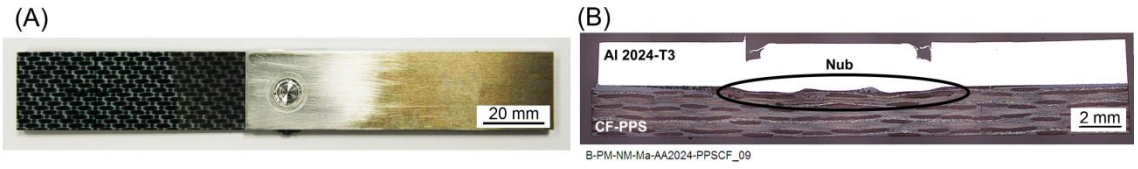

Figure 5.4 (A) Top view of a single lap Al 2024-T3/CF-PPS FSp joint with PPS interlayer and (B) corresponding cross section in spot area. (Joining Condition L, Table 4.4).

Different features could be observed at the joint interface through a detailed optical microscopy analysis of the cross-section of the joints, as illustrated in Figure 5.5. As discussed earlier, temperatures above 400°C were achieved during the joining process (Section 5.1). As a result of such high process temperatures, the PPS interlayer is molten and its viscosity is reduced. The molten interlayer is therefore squeezed out from the spot center to the edges of the joint due to the joining pressure applied by the tool. Accordingly, the PPS interlayer boundaries could not be identified between the aluminum and CF-PPS composite in the plastically deformed area in the center of the joint (Figure 5.5 A-C).

As a result of sandblasting performed on the joining parts prior to FSpJ, the aluminum part showed a surface roughness of $R_a = 5.5 \pm 0.3$ µm, while the surface roughness was $R_a = 5.3 \pm 0.6$ µm for the composite part. Crevices and irregularities were formed on the surfaces of the aluminum and composite. Due to the intimate contact between the joining parts because of the axial force applied by the tool, the crevices on the rough surface of the aluminum were filled with the molten PPS (Figure 5.5-B, black arrows). Simultaneously, the exposed carbon fibers were entrapped by the plasticized aluminum (Figure 5.5-C, black arrows). The fibers were exposed due to the removal of PPS matrix as a result of two phenomena: firstly, sandblasting removed a part of the PPS matrix, and secondly, during the joining cycle, part of the PPS matrix was molten at the center of the joint, and dislocated along with the PPS film interlayer to the sides of the joint. The second phenomenon was also observed by Goushegir *et al.* [10] and Esteves *et al.* [9] with FSpJ of aluminum/CFRP.

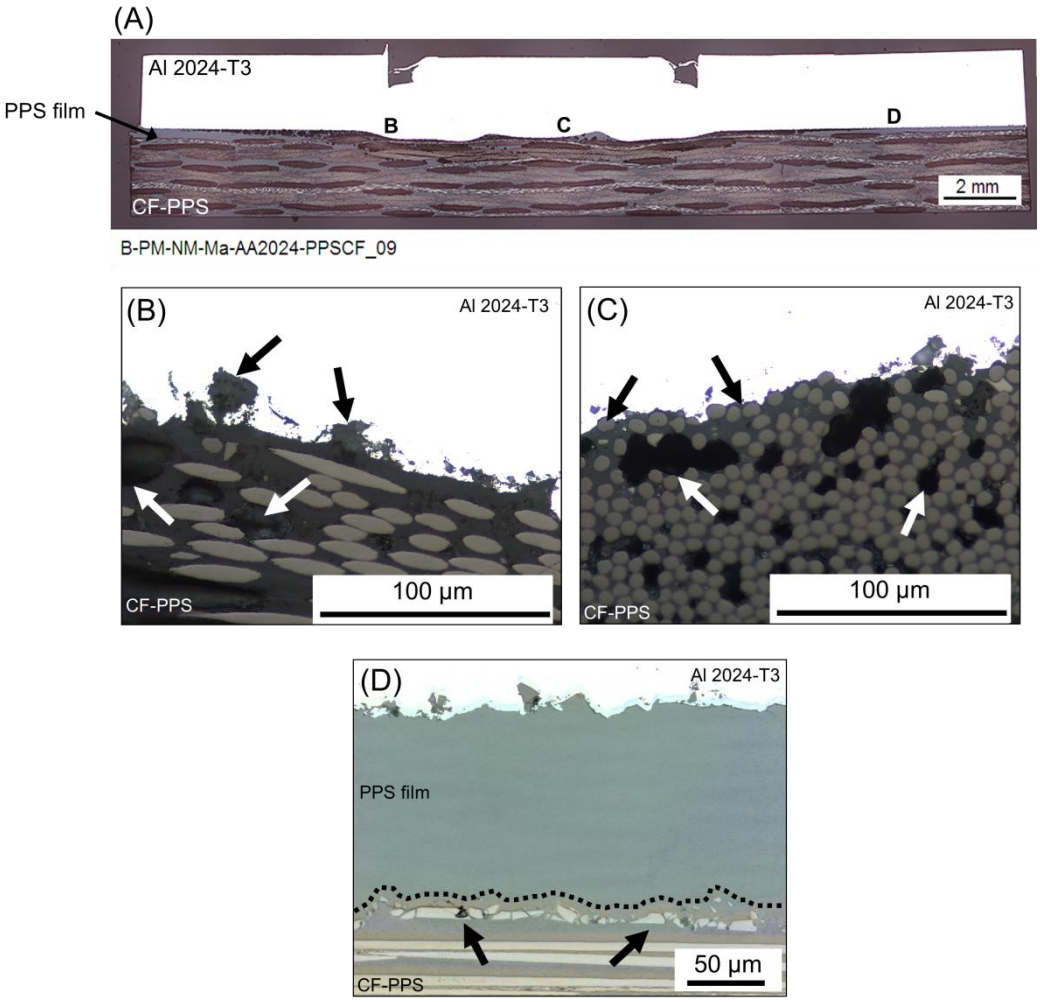

Figure 5.5 Microstructural details of the joint interface: (A) cross section of an FSp joint with interlayer; (B) entrapped molten polymer into the crevices of sandblasted aluminum surface; (C) carbon fibers embedded by the aluminum (black arrows), and microvoids (white arrows); (D) interface of aluminum/interlayer/composite at the edge of the joint.

Figure 5.5-B and C (white arrows) show the formation of microvoids in the PPS matrix at the center of the joint. The high frictional heat generated in a volume around the tool melted the PPS matrix. Therefore, air is entrapped into the molten PPS due to its outward flow, forming microvoids after the joint consolidation, as will be discussed in Section 5.4.2. The formation of microvoids was also addressed by Goushegir *et al.* [10] for Al 2024-T3/CF-PPS FSp joints.

Figure 5.5-D illustrates the cross-section at the edge of the joint. Firstly, an increase in the thickness of the PPS film interlayer is observed from the initial 100 µm to approximately 120-130 µm. The reason is the outward flow of the PPS film from the center of the joints, accumulating at the edges of the joint. Furthermore, one can observe that in both interfaces (i.e. aluminum/interlayer and interlayer/composite) an effective micro-mechanical interlocking was achieved as a result of the PPS entrapment in the crevices of both sandblasted aluminum and CF-PPS composite. Particularly, it is possible to identify that the PPS film has adopted the shape of the sandblasted surface of the composite at the interface between interlayer and composite (interface emphasized by a dash line in Figure 5.5-D). This observation demonstrated that the film was also softened at the interface with the composite, even though the thermal conductivity of the film is low. Further, some of the fibers were damaged, probably during the sandblasting of the composite surface, as indicated by the black arrows in Figure 5.5-D.

Therefore, from the evaluation of the interfaces two bonding micro-mechanisms were identified: the entrapment of PPS into the crevices of the aluminum and composite surfaces, and carbon fiber entrapment by the deformed aluminum. In addition, the metallic nub is responsible for the macro-mechanical interlocking between the joining parts, as discussed in details by Goushegir *et al.* [40].

5.4 Process-Related Microstructural Effects and Local Mechanical Performance

5.4.1 Aluminum 2024-T3

Figure 5.6-A presents a representative example of the cross section of an FSp joint with interlayer along with the aluminum microhardness profile. Because the spot joint is symmetric, only one half of the hardness map is displayed here. Similar to other friction-based joining processes, such as Friction Spot Welding (FSpW) [75], Friction Stir Welding (FSW) [79] and Friction Stir Spot Welding (FSSW) [80] of metals, three microstructural zones were identified in the aluminum part in this work. These are stir zone (SZ), thermo-

mechanically affected zone (TMAZ) and heat affected zone (HAZ), as indicated in Figure 5.6-A.

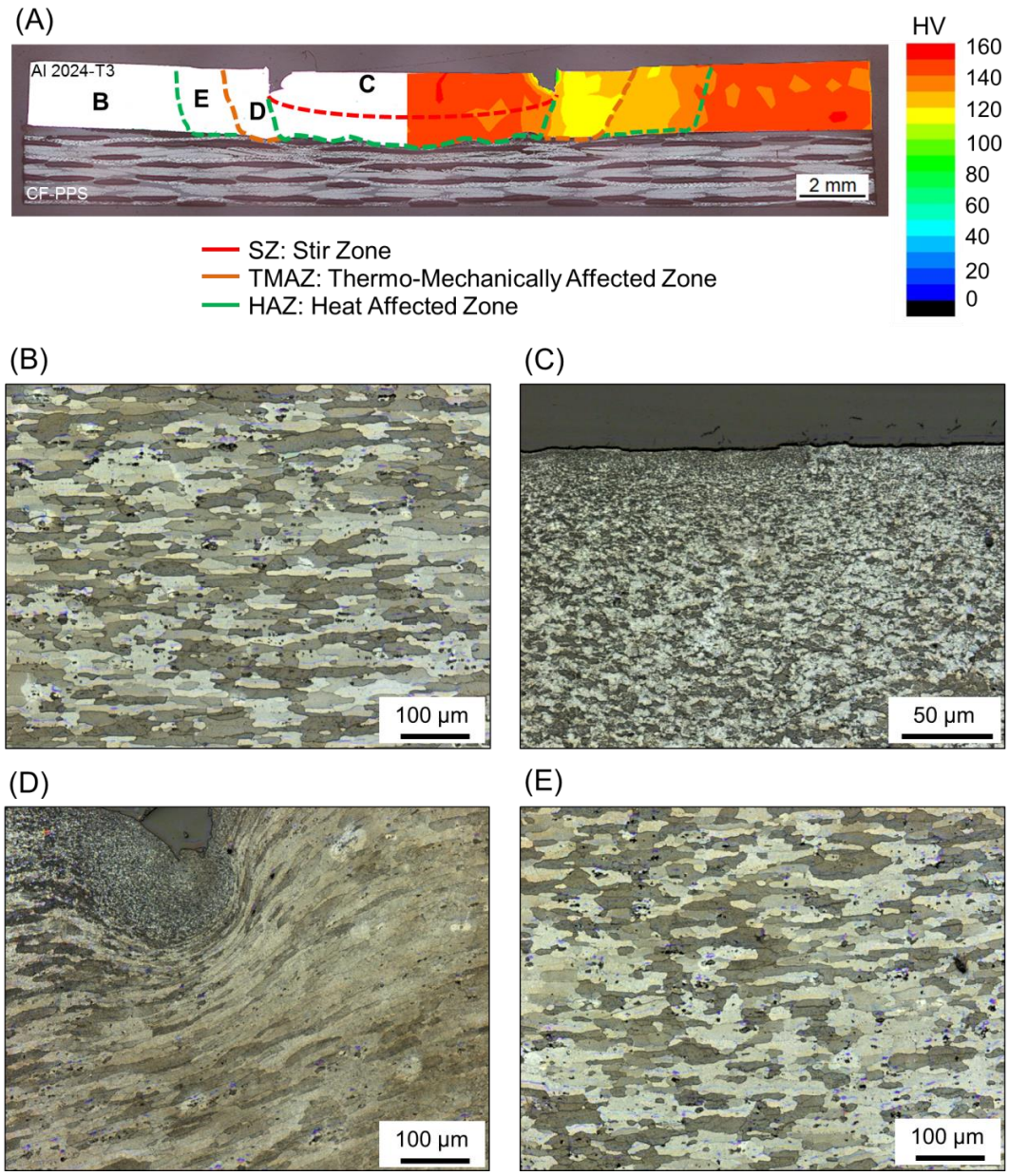

Figure 5.6 (A) Cross section and hardness profile of an FSp joint with interlayer as well as microstructural details of (B) base material, (C) SZ, (D) elongated and rotated grains of TMAZ (direction of rotation from top-right to bottom-left in the figure), and (E) HAZ. (Joining Condition H, Table 4.4)

The SZ comprises the upper region of the aluminum, which was in intimate contact with the tool during FSpJ. This region of aluminum undergoes

the highest shear rates imposed by the rotation of the plunging sleeve. In addition, the highest process temperature was achieved in this zone, exceeding the 60% of the incipient melting point of the Al 2024-T3 (502°C) required for the occurrence of recrystallization [81] (Section 5.1). The combination of such high temperatures and shear rate leads to the dynamic recrystallization of the aluminum in the SZ, as also described by Amancio *et al.* [75] in FSpW of Al 2024-T3. While the base material (BM) (Figure 5.6-B) demonstrates large grains oriented in the rolling direction of the aluminum, the SZ (Figure 5.6-C) shows grain refinement due to the development of dynamic recrystallization phenomenon. The grain refinement increases the local strength of the alloy as a result of the Hall-Petch effect.

Furthermore, the thermo-mechanical cycle imposed by the FSpJ process may strongly influence the type, distribution and size of the precipitates, and hence the local mechanical performance of the alloy. Genevois *et al.* [82] investigated the microstructure of Al 2024-T351 friction stir welds. They demonstrated the precipitation of metastable S'(S) phases as a result of the dissolution of the Guinier Preston Bagaryatskii (GPB) zones in this alloy at temperatures above 300°C. It is important to note that GPB zones consist of coherent precipitates, whereas S'(S) are incoherent precipitates. Such incoherent precipitates may decrease the local strength of the alloy [81]. On the other hand, the authors showed that in the center of the joints the temperatures were sufficiently high (350°C-450°C) to promote the re-precipitation of GPB zones, leading to precipitation hardening [82]. The re-precipitation process may also occur in the SZ of Al 2024-T3 FSp joined as well, once the alloy and the maximum process temperatures (325°C for L condition and 417°C for H condition) are very similar to those in [82].

As a result of grain refinement (Hall-Petch effect) and re-precipitation phenomenon an increase in hardness of SZ (154 HV) was observed compared to the BM (148 HV) (Figure 5.6-A).

TMAZ is the transition zone between the SZ and the HAZ. In TMAZ the metal is subjected to relatively high process temperatures and shear rates [75]. Due to the high deformation rate at the adjacent SZ, the grains in TMAZ are

elongated and rotated, as displayed in Figure 5.6-D. The deformation rate is not enough to promote the onset of dynamic recrystallization at this zone. However, recovering and grain growth processes may occur due to the high process temperature at this region. In addition, dissolution of GPB zones and subsequent precipitation of incoherent S'(S) phases may also occur [82]. Due to such softening mechanisms, a decrease in the hardness of this zone (116-120 HV) compared to BM was observed, as can be seen in Figure 5.6-A.

The HAZ, as the name implies, is only subjected to frictional heat generated during FSpJ. The HAZ is found between BM and TMAZ, as well as the area below the SZ (Figure 5.6-A). Static recovery may occur in this zone due to the high temperature achieved [81]. Dissolution of GPB zones and subsequent precipitation of incoherent S'(S) phases are also likely to occur [82]. Therefore, the local hardness was continuously reduced along the HAZ, starting from 140 HV near the BM and reaching 120 HV close to the TMAZ. Nevertheless, no visual changes in the microstructure were observed in this zone (Figure 5.6-E).

On the other hand, in the HAZ below SZ an increase in the hardness was identified (152 HV) compared to BM (Figure 5.6-A). In this region of HAZ, high temperature is achieved (similar to SZ) during the joining process due to the proximity to the heat source (the tool). Therefore, this region may be also affected by the re-precipitation phenomenon, as also described for SZ. The competition between static recovery and re-precipitation may occur. However, an increase in hardness (152 HV) compared to the BM was identified in this region. Therefore, it is believed that the re-precipitation mechanism dominates. This may be also the reason for the higher hardness observed in this area in comparison to the HAZ adjacent to the TMAZ (120 -140 HV).

5.4.2 CF-PPS Composite Laminate

Figure 5.7 shows a representative example of the cross section of an FSp joint with interlayer. A polymer heat affected zone (PHAZ) was identified by OM on the composite part of the joint.

Figure 5.7 Representative example of the microstructure of an FSp joint with additional interlayer indicating the PHAZ in the composite part of the joint. (Joining Condition L, Table 4.4).

In PHAZ temperatures above T_g and T_m were achieved, particularly close to the interface with the aluminum. The melting of the PPS allows it to recrystallize upon cooling in this zone, as discussed earlier in Section 5.2.1. Furthermore, the viscosity of the PPS matrix and film was reduced due to the high frictional heat generated. The film was squeezed out of the joint center, as previously discussed in Section 5.3. Simultaneously, air was entrapped in the molten matrix due to its outward flow, forming microvoids after the consolidation of the joint. The formation of microvoids was also addressed by Goushegir *et al.* [10] for Al 2024-T3/CF-PPS FSp joints without interlayer. As discussed in Section 5.1, the high heat input condition resulted in higher process temperature (417°C) than the low heat input condition (325°C). Therefore, the volume of polymer affected by the frictional heat is extended and the microvoids are more pronounced in this joining condition compared to the low heat input condition. Figure 5.8 illustrates details of the PHAZ containing volumetric defects in the center of the joints for low and high heat input conditions. Since thermal analyses (DSC and TGA) did not indicate extensive PPS thermal degradation during FSpJ process (Section 5.2), the volumetric defects are believed to be the result of entrapped air pockets. Some of the defects may be also a result of local delamination owing to differential thermal contraction between fibers and matrix [36]. Other static phenomena such as recovery, stress relaxation and physical aging may also occur at the PHAZ. However, such investigations were not in the scope of this thesis. For the detailed description of microstructural zones, please refer to Goushegir [36].

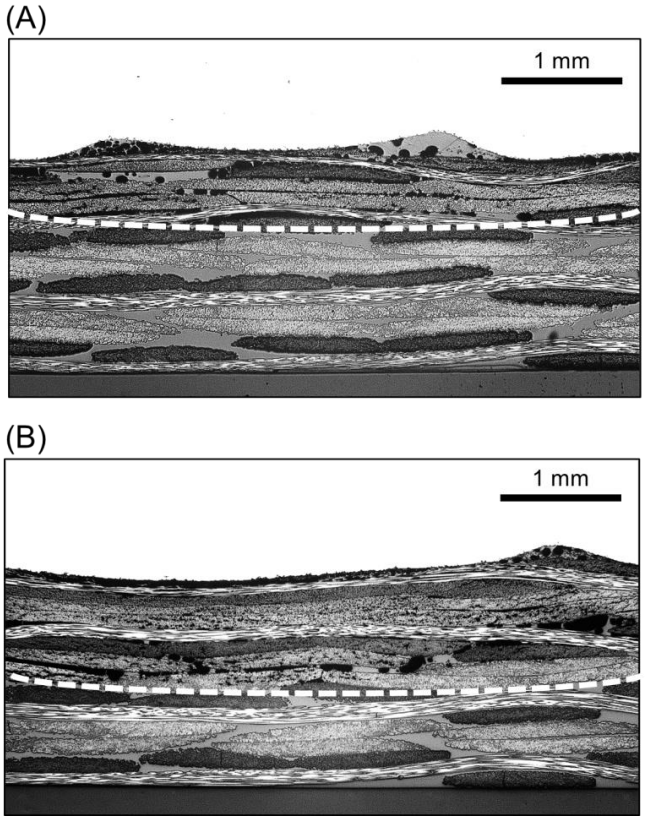

Figure 5.8 Microstructure of the joints in the center of the spot area for (A) low and (B) high heat input conditions. The dash lines indicate the PHAZ limit.

Nanohardness was employed to evaluate the local mechanical properties of the polymeric parts in an FSp joint produced with high heat input condition. Different regions were selected in a way that the PHAZ and base material (BM) were indented and analyzed, as indicated in Figure 5.9. The nanohardness results along with the statistical analysis (to evaluate the statistical significance of the results) are presented in Table 5.6.

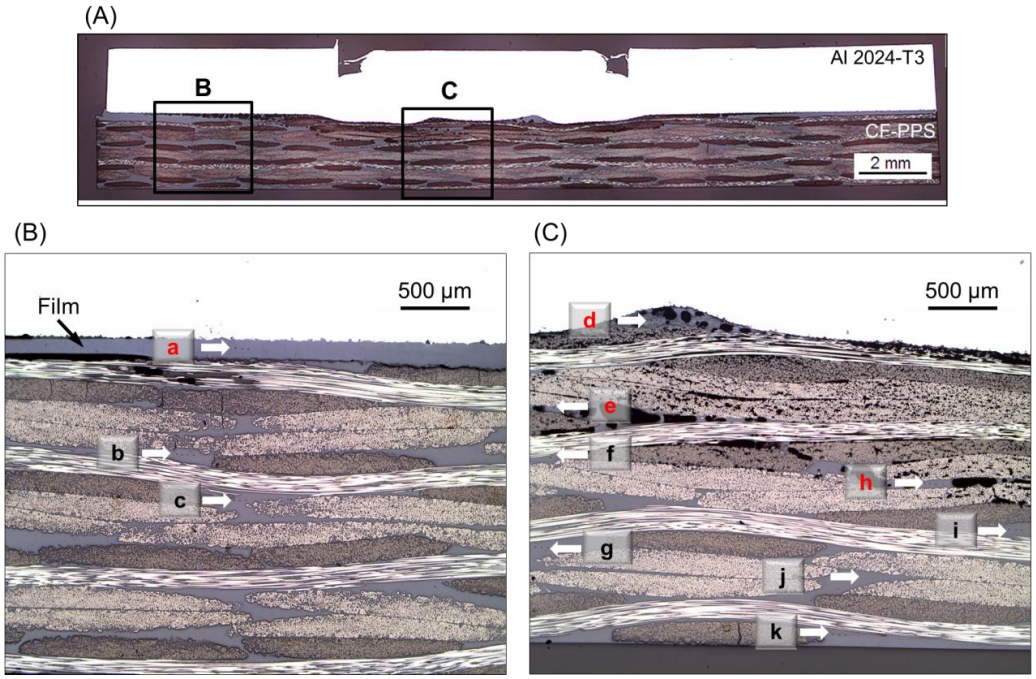

Figure 5.9 (A) Cross section of an FSp joint and (B) and (C) details of the regions analyzed by nanohardness.

Table 5.6 ANOVA and Tukey test for nanohardness evaluation (confidence level of 95%).

Region		**Nanohardness [GPa]**	**Tukey p = 0.000**	
g	CF-PPS Base Material	0.409 ± 0.008	A	
b		0.403 ± 0.008	A	
j		0.394 ± 0.004	A	
k		0.393 ± 0.003	A	
c		0.393 ± 0.007	A	
i		0.392 ± 0.003	A	
f		0.390	A	
e	PHAZ	0.329		B
h		0.325 ± 0.007		B
d		0.307 ± 0.007		B
a	Recrystallized film	0.326 ± 0.004		B

The average nanohardness of each region was compared by ANOVA and Tukey test considering a confidence level of 95% (α = 0.05). The p-value obtained from ANOVA was 0.000 (< α), i.e., the means under comparison presented a statistically significant difference. Further, the Tukey test demonstrated the existence of two groups of regions based on the nanohardness values.

The indents within the CF-PPS base material (Regions b, c, f, g, i, j and k, Figure 5.9-B and C) showed an average nanohardness of 0.39 - 0.40 GPa (Table 5.6). They were labeled by letter A in the Tukey test.

The indents selected from the PHAZ (Regions d, e and h, Figure 5.9-B and C) as well as the PPS film interlayer (Region a, Figure 5.9-B) showed an average nanohardness of approximately 0.32 GPa (Table 5.6). They were labeled by letter B in the Tukey test.

The lower values of nanohardness observed in PHAZ in comparison to the BM are probably related to the recrystallization process which this region undergone during FSpJ. As discussed in Section 5.2.1, the PPS matrix of the composite in the joint region has lower degree of crystallinity in comparison to the base material due to the high cooling rate during the consolidation phase. The crystalline phase is responsible for anchoring the amorphous phase. Therefore, the mobility of the macromolecules is increased with the decrease of the crystalline phase. Thus, it is easier to deform the material and the yielding is facilitated, decreasing the hardness of the composite [50]. Therefore, the decrease of hardness in the PHAZ is believed to be a result of the reduction in the degree of crystallinity. Besides the crystallinity, the formation of voids as well as the relief of stresses from the manufacturing process of the composite may also influence the local mechanical property of this zone.

It is worth to note that the recrystallized film (Region a, Figure 5.9-B) and the PPS matrix at the PHAZ (Regions e, d and h, Figure 5.9-B and C) shared the same letter (B) in the Tukey test (Table 5.6). After the FSpJ, the degree of crystallinity of the PPS film increased to a similar level as CF-PPS base material (Section 5.2.1). The increase in the degree of crystallinity contributes to the

local mechanical performance of the film, achieving similar hardness as the heat affected composite (0.32 GPa).

5.5 Composite Surface Pre-Treatments: Surface Properties and Quasi-Static Mechanical Performance

5.5.1 Surface Properties: Influence of Composite Surface Pre-Treatments

The surface modifications induced by the pre-treatments applied on the composite parts were analyzed by roughness and contact angle measurements. Tables 5.7 and Table 5.8, as well as Figures 5.10 to 5.14 summarize these results.

Table 5.7 Roughness and contact angle values of the surface of the aluminum in the as received condition and after the applied pre-treatments.

Material	Surface Pre-treatment	Symbol	Roughness (R_a) [µm]	Contact angle [°]
Aluminum	As received	AR	0.4 ± 0.1	77 ± 2
	Sandblasting	S1	5.5 ± 0.3	19 ± 2

Table 5.8 Roughness and contact angle values of the surface of the composite in the as received condition and after the applied pre-treatments.

Material	Surface Pre-treatment	Symbol	Roughness (R_a) [µm]	Contact Angle [°]
Composite	As received	AR	0.4 ± 0.1	69 ± 2
	Sandblasting	S2	3.8 ± 0.2	95 ± 3
		S3	4.3 ± 0.4	98 ± 1
		S4	5.3 ± 0.6	106 ± 4
	Mechanical Grinding	M1	0.6 ± 0.1	75 ± 1
		M2	1.2 ± 0.1	88 ± 2
	Plasma Activation	S4 + P1	5.3 ± 0.6*	8 ± 2
		S4 + P2	5.3 ± 0.6*	11 ± 2

*Measured before plasma activation

As can be seen in Table 5.8, sandblasting was the most effective surface pre-treatment in increasing the composite surface roughness. The topographical view of the mechanically pre-treated surfaces is presented in Figure 5.10. The sandblasted specimens exhibit a more rough and modified surface with hills and valleys compared to the mechanically ground specimens.

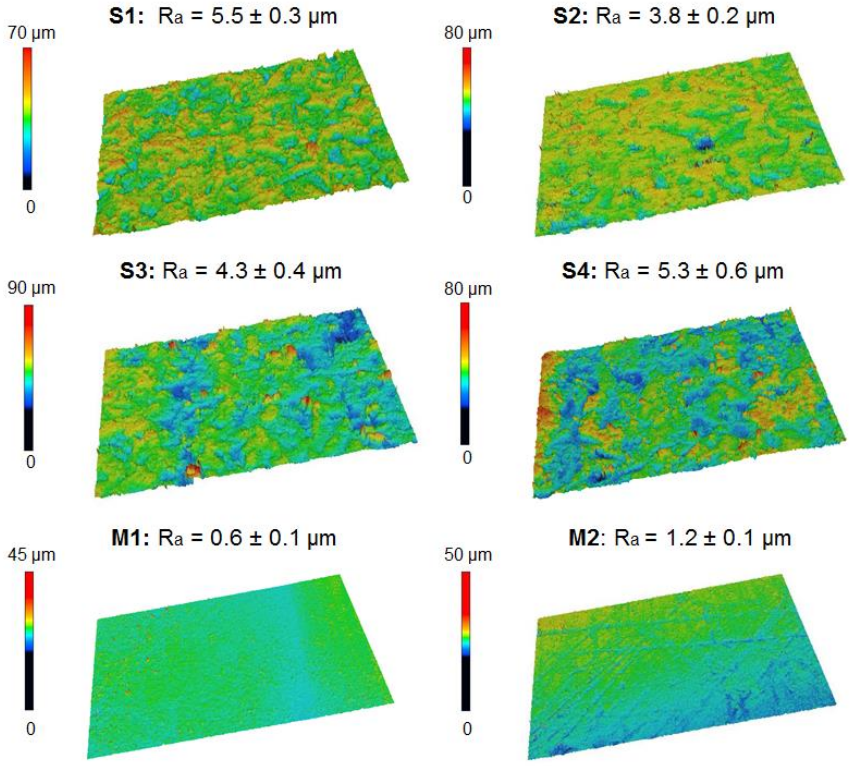

Figure 5.10 Topographical view and the arithmetic average roughness (R_a) of the aluminum and composite surfaces after mechanical pre-treatments, prior to the joining process. Refer to Table 4.5 for details of surface pre-treatments.

The sandblasting condition S4 (on the composite) removed most of the PPS matrix on the composite surface, thereby the treated surface shows exposed carbon fibers as can be seen in Figure 5.11-A. During FSpJ, the molten interlayer embeds these fibers, improving the mechanical anchoring between the parts (Section 5.3). In addition, a few damaged carbon fibers appear on the surface of the composite as a result of the sandblasting (Figure 5.11-B).

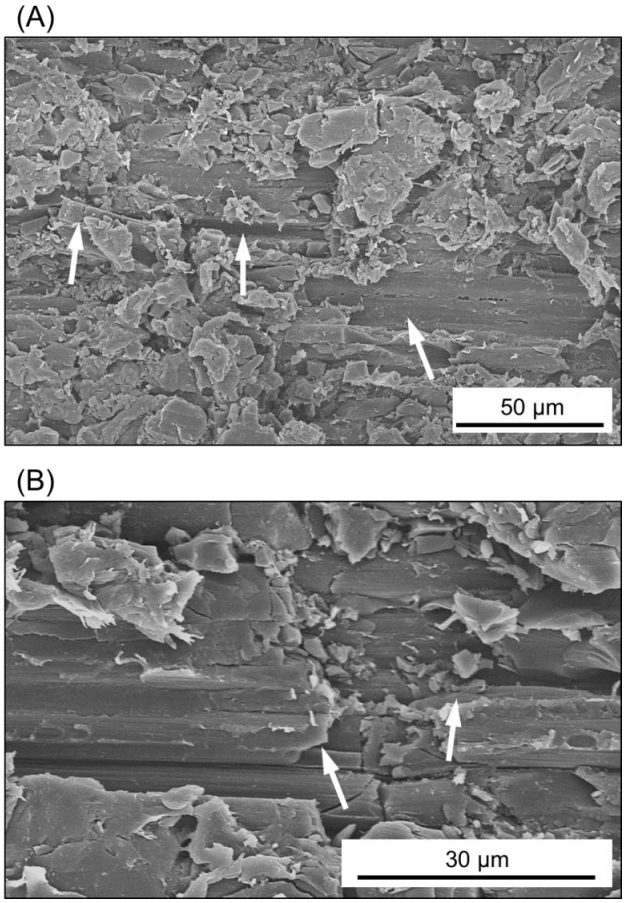

Figure 5.11 SEM images showing (A) the topography of sandblasted CF-PPS composite showing the partial removal of PPS matrix and some exposed carbon fibers and (B) the sandblasted composite surface, where the arrows indicate damaged fibers.

The wettability of the surfaces was monitored using contact angle measurements. For the aluminum part, the contact angle decreased continuously by increasing the surface roughness as seen in Table 5.7 and illustrated in Figure 5.12. The increase of the effective surface area and the removal of surface contaminations are known to increase the surface energy of the metal, reducing the water contact angle [60]. Therefore, an improved wettability on the aluminum surface was achieved through sandblasting. The molten polymer can flow into the crevices of the aluminum surface during the joining process. This causes micro-mechanical interlocking between the parts, leading to an increased mechanical performance.

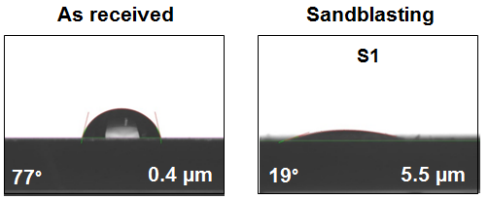

Figure 5.12 Example of contact angle measurements, along with the roughness (R_a), comparing as received and sandblasted aluminum surfaces.

A different trend was identified for the composite surface. For the mechanically-treated surfaces, the higher the surface roughness is, the larger is the contact angle, as shown in Figure 5.13. In contrast to a metal surface, the behavior of contact angle of a rough and hydrophobic polymer surface, such as the sandblasted PPS [83], is different. The liquid droplet does not make a full contact with the rough surface due to the hydrophobic forces present on the surface of the polymer. Therefore, water contact angle measurement does not correctly reflect the wettability of this sort of surfaces and has only a qualitative character for the current study [83]. Whereby, a detailed analysis of the influence of each individual treatment on the wettability of the composite surfaces could not be addressed. More information on these phenomena can be found in the following studies [74, 83-85].

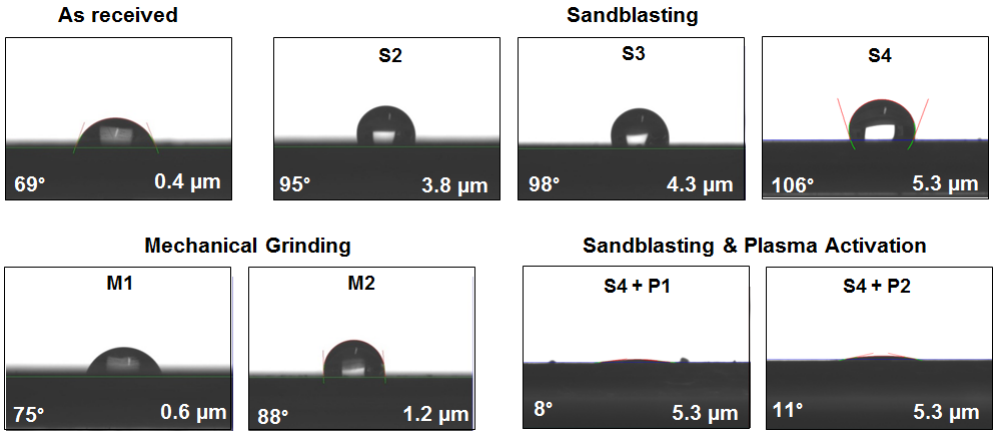

Figure 5.13 Example of contact angle measurements, along with the roughness (R_a), comparing as-received condition and different surface pre-treatments on the composite.

In case of the combination of sandblasting and plasma activation (S4+P1 and S4+P2) the water contact angle on the surface of the composites drastically decreased as shown in Figure 5.13. To better understand the combined effects of the selected surface pre-treatments, XPS analysis was performed in the treated specimens. Figure 5.14 shows the high resolution XPS spectra from oxygen bonds O1s region obtained for the sandblasted pre-treatment, as well as sandblasted followed by the plasma post-activation (using oxygen gas).

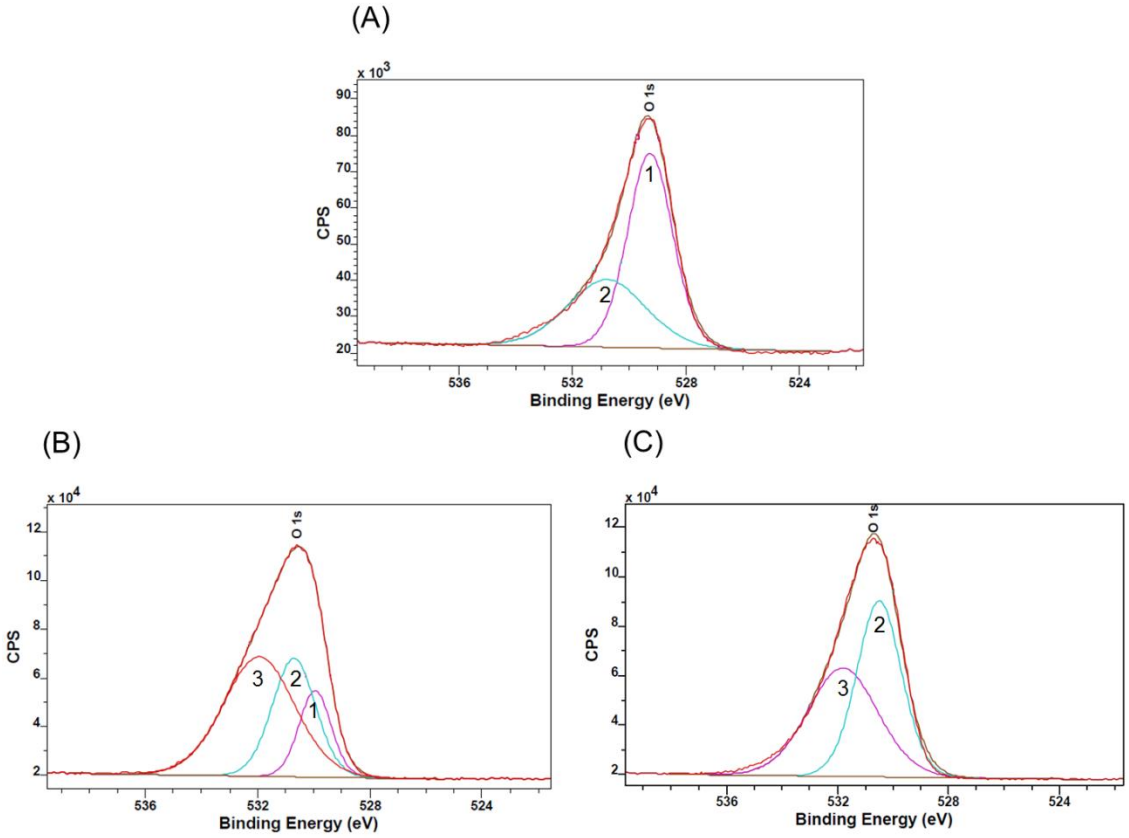

Figure 5.14 High resolution XPS spectra from O1s region on the CF-PPS composite surface for (A) sandblasted (S4), (B) S4 + P1 (5 min), and (C) S4 + P2 (10 min). (1: C–O–H, 2: C–O, 3: C=O).

From deconvolution of O1s peak, three chemical groups where identified at the specimens surfaces: (1) C–O–H, (2) C–O and (3) C=O. The C–O–H and C–O groups are found in all specimens and may be related with water and oxygen absorption from the atmosphere, respectively. Nevertheless, the intensity of C–O groups progressively increased as the specimens were plasma-treated, while the C–O–H groups were eliminated (Figure 5.14). On the

other hand, the C=O group was identified only for the plasma-treated specimens.

In the whole spectrum, the intensity of oxygen significantly increased from 85 $x10^3$ CPS (for sandblasting) to 11.5 $x10^4$ CPS and 11.8 $x10^4$ CPS for the post-activated surfaces S4 + P1 and S4 + P2, respectively. These results suggest that the surface free energy of the PPS was increased for the induced strong bonds of oxygen atoms, as a result of the plasma post-treatment. Therefore an increased wettability of the surface in comparison to sandblasted specimens was achieved (Figure 5.13). This is in agreement with the increase in wettability also observed for PPS plasma-activated in adhesively bonded joints by Anagreh *et al.* [86]. Contact angle measurements demonstrated that the surface energy of the PPS increased with the time of plasma treatment [86].

5.5.2 Quasi-Static Mechanical Performance of FSp joints with interlayer: Influence of Composite Surface Pre-Treatments

The influence of composite surface pre-treatments on the mechanical performance of the joints was addressed in this section. The joint produced under low heat input (L) condition was selected as a representative example of FSp joints with interlayer to perform this analysis. Sandblasting (S1) was applied for all aluminum parts, while the composite parts were treated with mechanical grinding (M1 and M2), sandblasting (S2, S3 and S4), as well as sandblasting combined with plasma activation (S4+P1 and S4+P2), as shown in Table 4.5. Figure 5.15 presents the ultimate lap shear force (ULSF) of FSp joints produced with different composite surface pre-treatments and its correlation with surface roughness.

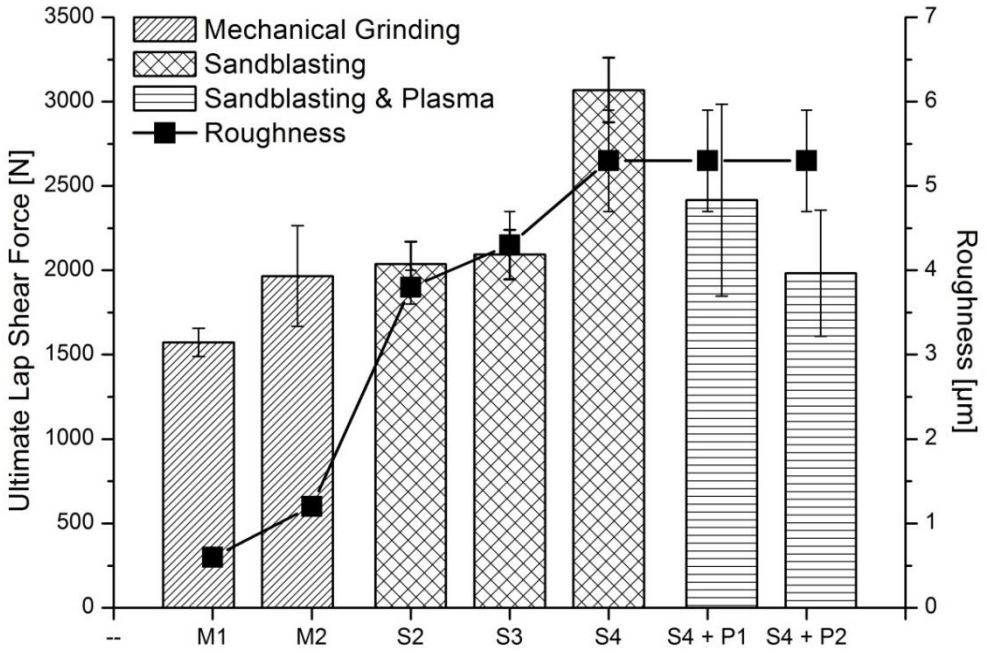

Figure 5.15 Ultimate lap shear force of FSp joints produced with different composite surface pre-treatments and the respective roughness. (Joining Condition L, Table 4.4).

One observes from Figure 5.15 that an increase in surface roughness increases the lap shear strength of the joint up to average levels of R_a = 5.3 µm. The composite surface with the highest roughness (S4: R_a = 5.3 ± 0.6 µm, Table 5.8) led to a joint approximately 95% stronger (S4: ULSF = 3068 ± 192 N) than the joint with the smallest roughness (M1: R_a = 0.6 ± 0.1 µm, Table 5.8; ULSF = 1573 ± 84 N).

The increase in roughness generates crevices on the surface and enlarges the effective contact area. This leads, firstly, to a better micro-mechanical interlocking between the CF-PPS composite and the PPS film. Secondly, a larger contact (surface) area increases the possibility of intermolecular diffusion between the composite's PPS matrix and PPS film at the joint interface due to the high temperatures achieved during the joining process. The intermolecular diffusion was also discussed by André *et al*. [87] for Al 2024-T3/CF-PPS FSp joints with interlayer and Jung *et al*. [88] for CFRP and PET laser direct joints. Therefore, the larger the surface roughness, the higher the micro-mechanical interlocking and adhesion forces between the joining

parts will be, leading to stronger joints in the joining parameters range and selected surface treatments.

The plasma activation, on the other hand, does not seem to contribute to the mechanical strength of the FSp joints (Figure 5.15) in this work. The sandblasted (S-) joints showed an ULSF of up to 3068 ± 192 N. After the plasma activation (i.e., S4 + P1 and S4 + P2) a decrease of 21% (2416 ± 568 N) was observed for S4 + P1 (5 min activation) and 35% (1983 ± 373 N) for S4 + P2 (10 min activation). During the plasma treatment, temperatures up to 110°C were achieved due to the power of plasma generation. Therefore, one possible explanation for this observation may be the exposition of the sandblasted composite to these temperatures. The local softening of the PPS matrix may induce closure of some crevices on the sandblasted surface. Thus, the effective contact area between composite and interlayer may be decreased as well as the micro-mechanical interlocking between the parts. Hence, a reduction in joint lap shear strength is observed. The decrease in ultimate lap shear force was pronounced for S4 + P2 because of the longer time of plasma treatment. Another plausible argument for the losses in mechanical performance for plasma-treated specimens can be associated to the FSpJ process. Because the composite in the center of the joint was melted during the FSpJ process, it is believed that the plasma activation was lost. Further investigations should be carried out to prove these two hypotheses.

The efficiency of surface pre-treatments on the joints strengthening was also evaluated through the overview of fracture surfaces presented in Figure 5.16.

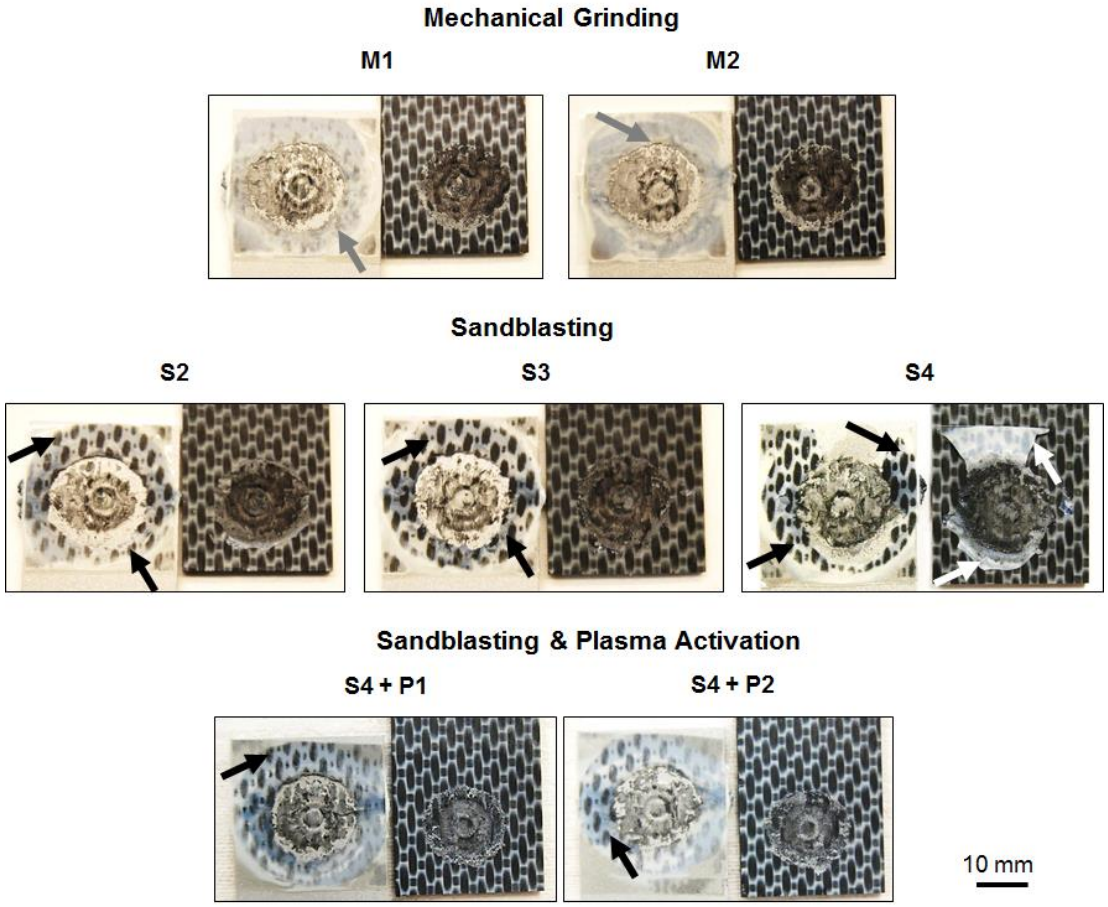

Figure 5.16 Examples of fracture surface of FSp joints from Figure 5.15 produced with different composite surface treatments.

It is worth to note that, for all treatments, the interlayer remains mostly attached to the aluminum surface (Figure 5.16) after lap shear tests. The rough sandblasted aluminum surface (S1 treatment, Table 4.5) appears to be effectively wet by the molten PPS interlayer during the joining process, as also suggested by the contact angle measurements (Figure 5.12). As it was discussed in Section 5.3, the irregularities on the aluminum surface were filled with the molten PPS leading to effective micro-mechanical anchoring between the aluminum and PPS interlayer.

By comparing the fracture surfaces of mechanically ground (M-) and sandblasted (S-) specimens in Figure 5.16, a pronounced difference can be observed between their adhesive zones (refer to Figure 3.4 for FSpJ bonding zones). An impression of the composite (in the form of black spots resembling the weave pattern of fiber reinforcement) was identified on the surface of the

interlayer for the sandblasted specimens (indicated by black arrows in S2, S3 and S4 specimens, Figure 5.16). However, this was not the case for the mechanically ground specimens (indicated by gray arrows in M1 and M2 specimens, Figure 5.16). Detailed evaluation of these impressions by SEM analysis is presented in Section 5.6.4. Briefly, the impressions contain pieces of carbon fibers extracted from the PPS matrix, which remained attached to the interlayer. This can be considered an indication of a more effective micro-mechanical interlocking at the interlayer-composite interface achieved for the sandblasted specimens. The higher efficiency of sandblasting treatment was also addressed by Wingfield *et al.* [58] in adhesively bonded GF-PP joints. The authors reported lap shear strength of 2 MPa for the joints produced with mechanical ground specimens, whereas the sandblasted specimens resulted in joints with lap shear strength of 4 MPa.

In addition, part of the consolidated interlayer material was identified in the fracture surface of the composite part of S4 specimens (white arrows in Figure 5.16). This is an indication that the adhesion of the interlayer-composite interface is better compared to the metal-interlayer interface in these regions. The S4 pre-treatment generated the highest roughness on the composite surface among all specimens, and consequently led to the highest mechanical strength of the joints.

The fracture surface of S4 + P1 and S4 + P2 joints also presented the black impressions on the interlayer surface since they were subjected to sandblasting prior to the plasma activation. However, the intensity of the black spots is not as visually pronounced as the S4 fracture surface (Figure 5.16). The less pronounced black impressions might be an indication of less effective micro-mechanical interlocking. As previously discussed in Section 5.5.1, the exposure to high temperature during plasma treatment might cause softening of the PPS matrix and closure of some of the crevices. It can also be observed from Figure 5.16 that the fracture surface of the S4 + P2 specimen visually presents even smaller amount of black impressions compared to the S4 + P1 specimen. This is probably due to the longer plasma-treated time used for S4 + P2. As a result, S4 + P2 joints presented lower average ultimate lap shear

forces (1983 ± 373 N, Figure 5.15) than S4 + P1 joints (2416 ± 568 N, Figure 5.15).

5.6. Global Mechanical Performance and Failure Mechanisms

Based on the mechanical results presented in Section 5.5, the best-performance lap shear joints produced with the combined S4 (composite) - S1 (aluminum) surface treatments were selected for detailed quasi-static and dynamic mechanical testing .

5.6.1. Quasi-static Mechanical Behavior of Single Lap FSp Joints with Interlayer

The quasi-static mechanical performance of the FSp joints was investigated through lap shear testing following the procedure described in Section 4.2.8. Representative shear force-displacement curves are presented in Figure 5.17. The curves for all mechanical testing can be found in Appendix E. The joints produced under both high (H) and low (L) heat input conditions exhibit an elastic behavior with small elongation at failure.

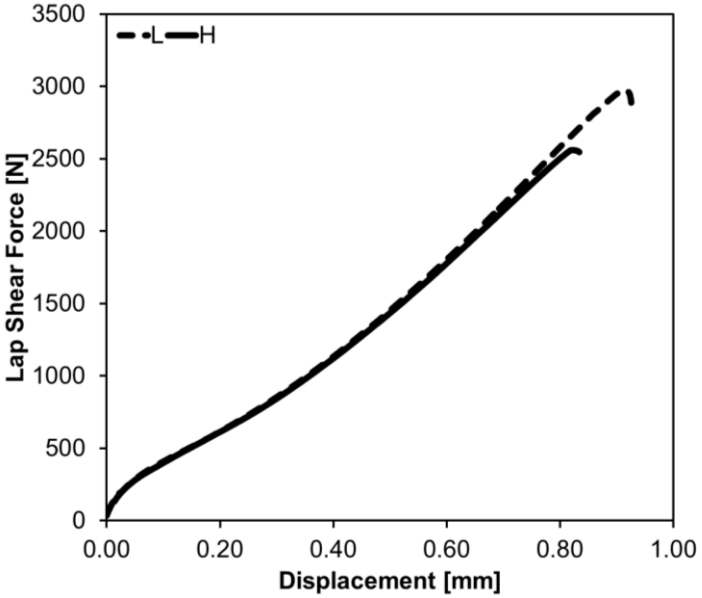

Figure 5.17 Representative example of shear force-displacement curves of FSp joints with interlayer under high (H) and low (L) heat input conditions.

The FSp joints with interlayer showed an ultimate lap shear force of 2703 ± 114 N for high heat input and 3069 ± 166 N for low heat input conditions. The joints produced with low heat input presented an average bonding area of 588.4 ± 48.4 mm^2 similar to those produced with high heat input condition (589.4 ± 25.2 mm^2), as indicated by dash lines in Figure 5.18. It is worth to mention that the bonding area comprises a circular zone in the center of the overlap area. Un-bonded regions close to the corners of the joint could be also identified as a result of the circular heat distribution in FSpJ. Due to the generation of excessive frictional heat in the high heat input condition, the decrease in the viscosity of the molten PPS film was more pronounced. Hence, a qualitatively larger amount of the molten interlayer was squeezed out of the bonding area as flash in this joining condition. The solid-line ellipses in Figure 5.18 indicate the larger amount of squeezed out molten interlayer for the high heat input compared to the low heat input condition. Therefore, the contribution of adhesion forces provided by the film interlayer on the mechanical performance of the joints was probably reduced for the high heat input condition, decreasing the lap shear strength of the joint.

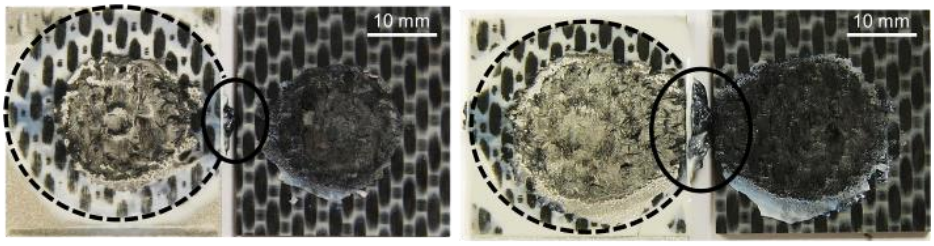

Figure 5.18 Example of fracture surfaces of FSp joints with interlayer: (A) condition L and (B) condition H.

Furthermore, comparing to the joints without interlayer [40] an increase of 55% in ultimate lap shear force was observed in this work for the joints with interlayer produced with low heat input condition (Figure 5.19). It was 1981 ± 106 N [40] for the joints without interlayer, increasing to up 3069 ±166 N for the interlayer joints (Figure 5.19). In case of the high heat input condition an average improvement of 19% was reached; 2280 ± 88 N [40] for joints without and 2703 ± 99 N for joints with film (Figure 5.19). Such increase in lap shear

force indicates the effective contribution of adhesion forces from the interlayer to improve the mechanical performance of FSp joints. Moreover, superior lap shear strength of the joints with interlayer can be related to the larger bonding area and the better load distribution usually found in weld-bonding techniques [89], as well as the bonding mechanisms which will be explained next.

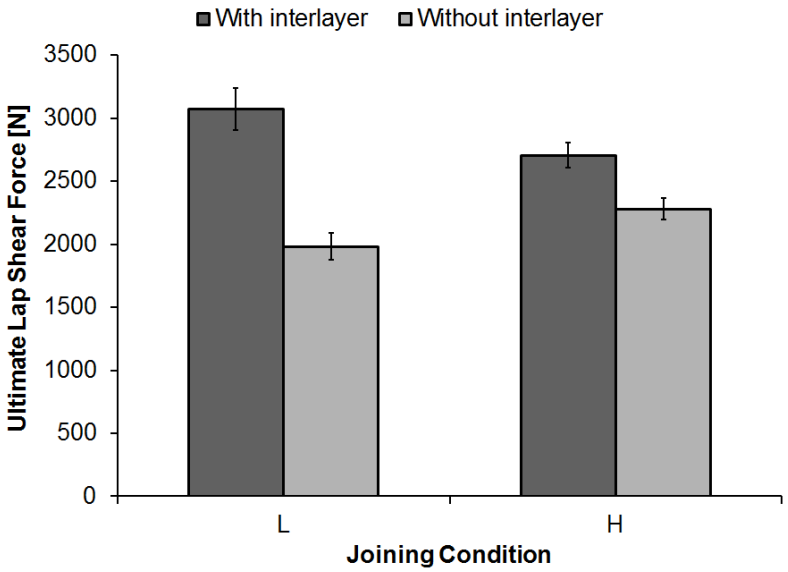

Figure 5.19 Ultimate lap shear strength of FSp joints with interlayer compared to those without interlayer [40]. A comparison of the shear force-displacement curves for joints with and without interlayer is given in Appendix F.

Figure 5.20 demonstrates a representative example of the fracture surface of FSp joints with and without interlayer; the total bonding area is depicted as dash-line circles. The joints with interlayer produced under low heat input condition presented an average bonding area of 588.4 ± 48.4 mm^2 (Figure 5.18-A) while this was 356.9 ± 10.1 mm^2 [40] for the joints without interlayer. It suggests that the use of interlayer led to an increase of approximately 65% in the bonding area of the joints produced with low heat input condition. The increase of bonding area was 25% in case of the joints produced under high heat input joining condition. It changed from 470.3 ± 15.9 mm^2 [40] for the joints without interlayer to 589.4 ± 25.2 mm^2 for the joints with interlayer (Figure 5.18-B). In addition to the larger bonding area, the fracture surface of the joints

produced in this study presented other differences compared to those joints without film. Black spots were identified on the interlayer inside the bonding area as it can be seen in Figure 5.20-A (yellow arrows). These spots could not be found on the fracture surfaces of the joints without film (Figure 5.20-B). The black spots were identified as parts of carbon fibers and PPS matrix from the composite that remained attached to the film after failure. It is a result of an effective micro-mechanical interlocking between the interlayer and the composite. Such strong micro-mechanical interlocking also contributes to higher shear strength of the joints with interlayer compared to the joints without interlayer (Figure 5.19). The impression of the composite left behind on the PPS interlayer as referred to black spots will be discussed in Section 5.6.4.

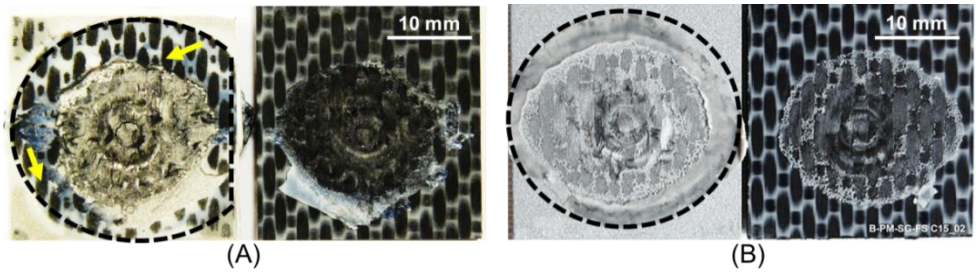

Figure 5.20 Representative example of fracture surfaces of FSp joints (A) with interlayer and (B) without interlayer [40]. (Condition H, Table 4.4)

To assess the mechanical performance of the joints, a qualitative comparison of the lap shear strength was made between FSp joints and those produced with the state-of-the-art and concurrent joining technologies. The current material combination was not found in other works in the literature, excepting for friction spot joints without interlayer. Thus, similar metal-polymer composite joints with different materials but similar thicknesses (see Table 5.9) whose failure mechanisms are similar to the FSp joints were selected. Figure 5.21 displays this comparison. For this purpose, the ultimate lap shear force of the FSp joints were converted to ultimate shear strength (refer to Section 4.2.8). Table 5.9 summarizes the main details of the surface preparation and joining procedure for those literature joints presented in Figure 5.21.

Table 5.9 Details of surface preparation and joining procedure of the hybrid joints presented in Figure 5.21.

Joining Technique	Metal Part (thickness)	Polymer / Composite Part (thickness)	Surface Pre-Treatment	Shear Strength	Joining Time	Reference
Adhesive Bonding	$AlMg_3$ (2 mm)	CF-PA66 (2 mm)	Metal: chemical etching with H_2SO_4 and NaOH	17 MPa	30 min (180°C)	[90]
Resistance Welding	Al7075-T6 (2 mm)	CF-PEEK (2 mm)	Metal: cleaning with trichloroethane, anodizing with phosphoric acid and recovering with PEI	20 MPa	30 s to 5 min	[17]
Ultrasonic Welding	Al 5754 (1 mm)	CF-PA66 (2 mm)	Metal: sandblasting and nitric acid etching for 15 min	50 MPa	3.5 s	[29]
Induction Welding	$AlMg_3$ (1 mm)	CF-PA66 (2 mm)	Metal: cleaning with acetone and sandblasting with corundum	11 MPa	53 s	[13]
Induction Welding with interlayer	$AlMg_3$ (1 mm)	CF-PA66 (2 mm) with PA66 interlayer (100 µm)	Metal: cleaning with acetone and sandblasting with corundum	13 MPa	53 s	[13]
FSpJ	Al 2024-T3 (2 mm)	CF-PPS (2 mm)	Metal: sandblasting with corundum	31 MPa	4 s	[40]
FSpJ with interlayer	Al 2024-T3 (2 mm)	CF-PPS (2 mm) with PPS interlayer (100 µm)	Metal: sandblasting with corundum Composite: sandblasting with corundum	47 MPa	4 s	Current work

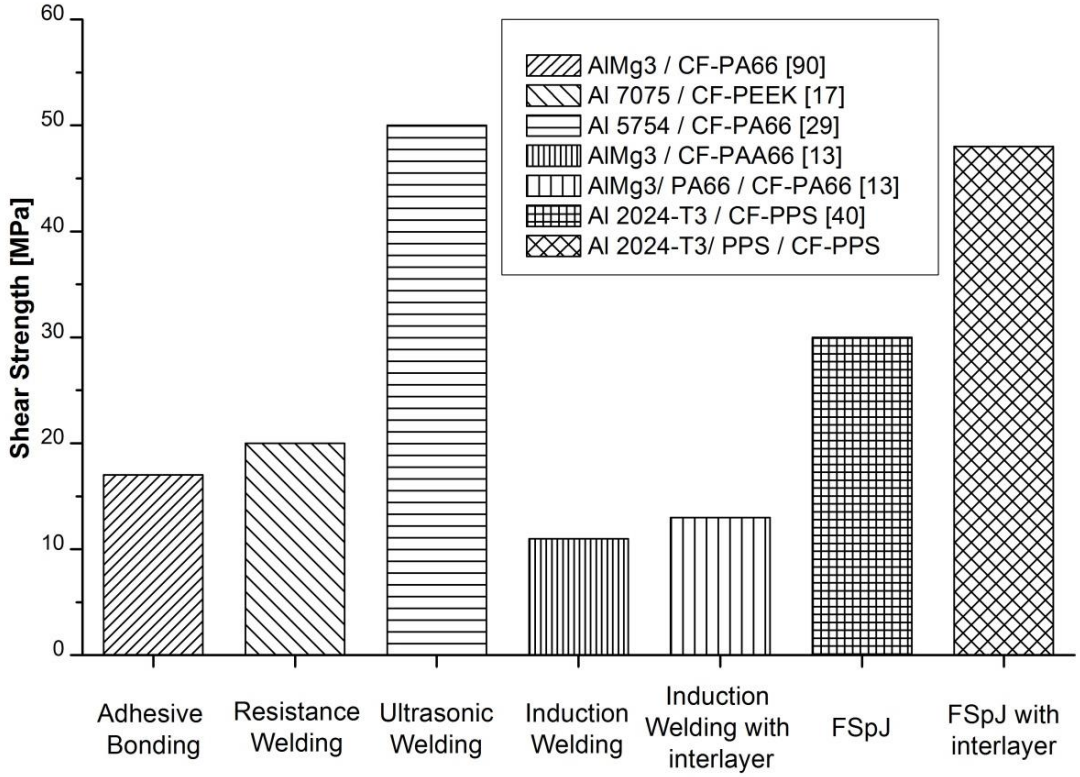

Figure 5.21 Qualitative comparison of quasi-static mechanical performance of Al 2024-T3/PPS/CF-PPS FSp joints with similar metal-thermoplastic composite joints produced by state-of-the-art joining techniques.

Figure 5.21 shows that the Al 2024-T3/CF-PPS FSp joints with PPS interlayer have exhibited superior or similar strength than other joints produced with currently available joining technologies. Moreover, as listed in Table 5.9, the surface pre-treatment used in this study for FSp joints was easier to apply and more environmentally friendly in comparison to chemical treatments (for adhesive bonding and ultrasonic welding) and anodizing (for resistance welding) reported for the state-of-the-art techniques.

Besides providing equal or superior mechanical performance than state-of-the-art joining techniques, there is a great benefit related to the process time with FSpJ. The FSpJ process requires only a single joining step, which lasts a few seconds (4 s in this work). Therefore, FSpJ is much faster than induction welding (53 s) [13] and adhesive bonding which shortest reported time is 30 min [90]. In addition to the process time, the curing of adhesive is usually performed

at high temperature (180°C) which is another limitation of adhesive bonding, particularly for large components. In its current state of development the FSpJ with interlayer has still slightly longer joining cycles than ultrasonic welding (3.5 s [29]); however, comparable times are expected to be achieved with the forthcoming developments of the FSpJ technique.

Such advantages in terms of process time, ease of handling and excellent joint mechanical performances turn the FSpJ process with film interlayer a potential technology to join metal-composite hybrid structures.

5.6.2 Cyclic Mechanical Behavior (Fatigue Performance) of Single Lap FSp Joints with Interlayer

The fatigue performance of FSp joints with interlayer was investigated and the results are discussed in this section. Figure 5.22 presents the S-N curves for the Al 2024-T3/CF-PPS FSp joints with PPS film interlayer produced under low and high heat input conditions. Force (load) values were used in the fatigue analysis for a simple and direct comparison between joints. However, the term S-N curve (strength-life) is used because of its common used in the literature. The fatigue life of the joints was investigated under load levels corresponding to 35%, 50% and 75% of the respective ultimate lap shear force (ULSF). An exponential model typically adopted in the literature [91-93], and detailed in Appendix A, was used to produce the fitting curves.

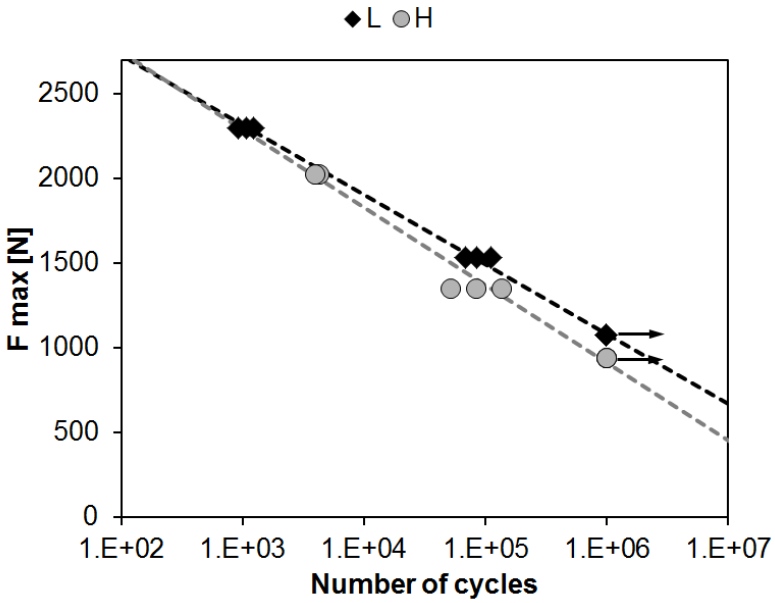

Figure 5.22 Derived S-N curves based on the exponential model for Al 2024-T3/CF-PPS FSp joints with PPS film interlayer. The maximum force (F_{max}) corresponds to the applied fatigue load levels derived from the quasi-static lap shear tests.

It can be observed in Figure 5.22 that the heat input did not strongly influence the fatigue life of the FSp joints with interlayer. However, the low heat input joint showed slightly better fatigue performance. At high cycle fatigue regime (HCF) above 10^4 cycles the difference between the fatigue strength of the joining conditions is more pronounced. It was discussed in Section 5.6.1 that the joining with low heat input condition resulted in joints with higher static shear strength than the high heat input condition. The fatigue strength of the joints followed the same trend. The fatigue strength of the joints produced under low heat input is higher, and the fatigue life was extended.

Roesler *et al.* [94] found out that the fatigue strength of a material is much more sensitive to defects and manufacturing process than the static strength particularly in the HCF regime. Section 5.4.2 and Figure 5.8 showed that the high heat input condition leads to a joint with more defects and microvoids. Such microvoids may act as initiation sites for micro-cracks. The coalescence of micro-cracks will lead to the formation of macro-cracks and the final failure of the joint. Besides the lower quasi-static strength, this is believed

to be another reason contributing to the lower fatigue strength of the high heat input joint in HCF regime.

The joints produced with both joining conditions survived one million cycles without failure at a force level corresponding to 35% of their respective quasi-static strength. These joints were then subjected to quasi-static lap shear testing to evaluate their residual strength. Figure 5.23 exhibits the residual strength of the joints after one million cycles in comparison with the initial quasi-static strength.

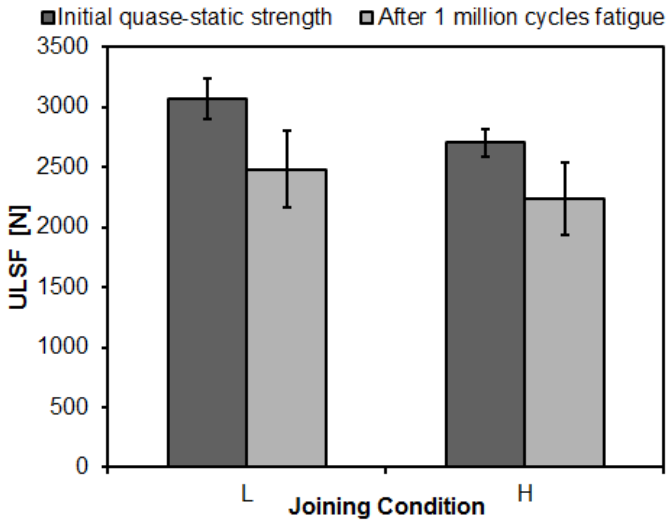

Figure 5.23 Comparison between initial and residual quasi-static strength of Al 2024-T3/CF-PPS FSp joints with PPS film interlayer after one million cycles for specimens tested with 35% of F_{max}. (L: low and H: high heat input conditions, Table 4.4).

The reduction of quasi-static strength after one million cycles was very similar for both joining conditions. The joints produced with low heat input condition showed a reduction of 19% after one million cycles; 3069 ± 166 N before and 2483 ± 321 N after fatigue testing. Similarly, the joints produced under high heat input condition showed a decrease of 17% after one million cycles; 2703 ± 114 N before and 2240 ± 320 N after fatigue testing. This reduction in strength is an indication of fatigue damage accumulation in the joints. Shear and peel stresses developed at the edges of the joint may contribute to the damage accumulation in FSp joints during cyclic loading [36].

Dubé *et al.* [92] also observed this trend in resistance welding of thermoplastics. Despite the observed damage accumulation, the fatigue damage of Al 2024-T3/CF-PPS FSp joints with PPS film interlayer is less extensive than those reported for high-performance composite joints in the literature. For instance, CF-epoxy (IM6/3501–6) and CF-PEEK adhesively bonded joints showed a decrease of 40% of initial strength after 10^6 cycles [95]. Moreover, a decrease of 35% of initial static strength after one million cycles was reported by Dubé *et al.* [92] for resistance welding of CF-PEEK.

A comparison of the fatigue performance of the Al 2024-T3/CF-PPS FSp joints with and without interlayer was carried out for joints produced with high heat input (which correspond to the strongest FSp joints without interlayer). The data of joints without interlayer were obtained from the work of Goushegir [36]. Figure 5.24 addresses this comparison based on the normalized load levels (%ULSF - ratio of maximum applied fatigue load over quasi-static strength of the joint).

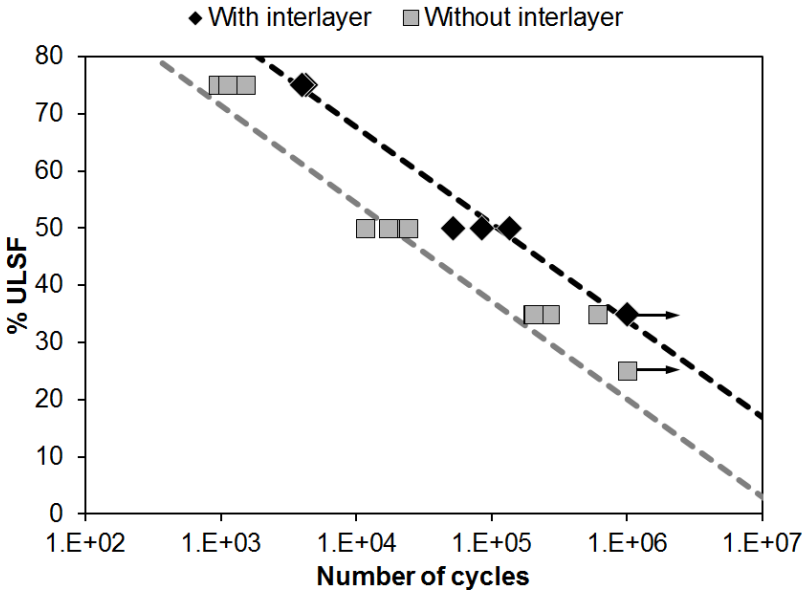

Figure 5.24 Derived S-N curves based on the exponential model of high heat input Al 2024-T3/CF-PPS FSp joints with and without additional PPS film interlayer. Data of joints without PPS film interlayer were obtained from [36].

Al 2024-T3/CF-PPS FSp joints with additional PPS interlayer presented superior fatigue strength in comparison with the joints without interlayer (Figure

5.24). For instance, at 10^5 cycles - the typical application requirement for testing different joint designs in the aircraft industry [96] - the interlayer joint showed fatigue strength of 51% of ULSF, whereas the fatigue strength of the joint without interlayer was 37% of ULSF. In a general trend and in the whole spectrum, the joint with additional interlayer showed a fatigue life approximately 4 times higher than the joint without interlayer.

The better fatigue performance of the joint with additional PPS interlayer is probably related to the larger bonding area and the bonding mechanisms. As discussed in Section 5.6.1, the joint with interlayer presented an average bonding area of approximately 25% larger than the joint without film for the selected joining condition (Figure 5.20). Additionally, inside the bonding area some black spots were identified on the interlayer as shown in Figure 5.20-A. The black spots are a result of an effective micro-mechanical interlocking between the PPS interlayer and the CF-PPS composite. Such strong micro-mechanical interlocking at the interface was not found for the joints without interlayer (see Figure 5.20-B). The larger bonding area may allow a better distribution of stress over the joints as they are overloaded. Furthermore, the additional contribution of micro-mechanical interlocking (represented by the black spots, Section 5.6.4) may help the joint to withstand the applied stresses. Therefore the increase in micro-mechanical interlocking in the whole bonding area seems not only increased the quasi-static strength of the joint with interlayer but also its fatigue strength compared to the joint without interlayer.

The FSp joints with interlayer survived one million cycles without failure at a force level corresponding to 35% of their respective quasi-static strength, whereas the joints without interlayer achieved this fatigue life at only 25% of their quasi-static strength [36]. These joints were then subjected to quasi-static lap shear testing to evaluate their residual strength. Figure 5.25 exhibits the residual strength of the joints after one million cycles in comparison with the initial quasi-static strength.

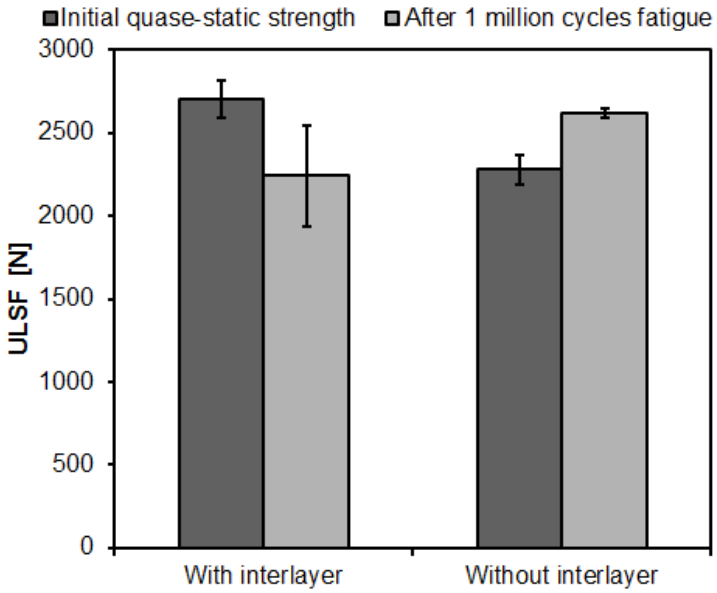

Figure 5.25 Comparison between initial and residual quasi-static strength of Al 2024-T3/CF-PPS FSp joints with and without interlayer [36] after one million cycles for specimens. (Joining condition H, Table 4.4).

As mentioned earlier, the joints with interlayer (condition H) showed a decrease of 17% in quasi-static strength after one million cycles due to fatigue damage accumulation. Surprisingly, the joints without interlayer presented an increase of 15% in the quasi-static strength after fatigue, suggesting that no damage was accumulated in the joints during the cyclic loading [36]. However, the analysis was not conclusive [36]. Advanced studies must be performed to better understand the different trends in fatigue damage accumulation for FSp joints with and without interlayer.

5.6.3 Durability of FSp Joints with Interlayer

Figure 5.26 compares the residual strength after short-term hydrothermal aging of 7 days for joints produced under low (L) and high (H) heat input joining conditions.

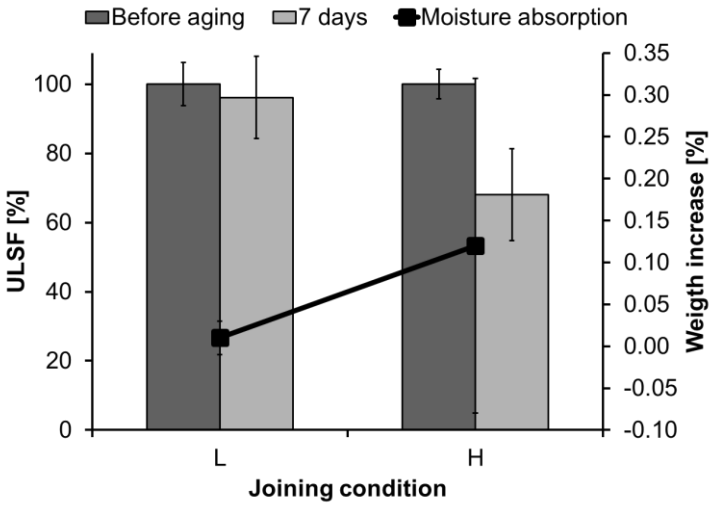

Figure 5.26 Residual strength and moisture absorption of Al 2024-T3/CF-PPS FSp joints with PPS film interlayer produced under high and low heat input joining conditions after short-term hydrothermal aging (100% relative humidity at 71°C).

Although still within the standard deviation of the joints tested prior the accelerated test, joints produced with low heat input presented a decrease of 3.8% in ULSF. The high heat input condition joints showed an average reduction of 32% in ULSF after short-term accelerated aging. The pronounced decrease in strength for joints produced with high heat input condition can be explained based on the moisture absorption. The weight increase due to water absorption was nearly zero (0.01 ± 0.02 %) for the low heat input joint, whereas it was 0.12 ± 0.20 % for the high heat input joint.

It is well known from the accelerate aging from adhesive bonding that overlap joints are prone to absorb moisture from the environment, which will depreciate quasi-static strength [97]. At high temperature the absorption phenomena is thermodynamically facilitated [98]. As discussed in Section 5.4.2, during the joining process microvoids are formed close to the joint interface. These microvoids may facilitate the absorption of moisture. Once the moisture is absorbed, several phenomena may occur at the joint interface. The polymeric parts may swell due to the water absorption [99], resulting in local decoupling from the adjacent part. Furthermore, in the case of the aluminum, the chemical reaction with environmental moisture may form a weak layer of hydroxide [46],

deteriorating the aluminum-PPS bonding at the interface. Thus, the larger amount of microvoids produced in the high heat input condition (as described in Figure 5.8) seems to facilitate the absorption of environmental moisture.

For the joints produced with high heat input, the amount of interlayer squeezed out as flash was larger (see Figure 5.18). Consequently, the sealing contribution of the interlayer against water diffusion inside the joint was probably decreased. Therefore, higher amount of water absorption and a less contribution of the PPS interlayer against diffusion of the water are believed to be the reasons for a larger decrease in the joint strength for high heat input joint. These assumptions should be further confirmed through a detailed investigation of the fracture surface, such as chemical composition and micro-mechanisms of failure. Nevertheless this was out of the scope of this MSc thesis.

Since the joints produced under low heat input joining condition presented better durability under short-term hydrothermal accelerated aging, this joining condition was studied under long-term (28 days) hydrothermal accelerated aging. The residual quasi-static mechanical strength of the joints after accelerated aging and the moisture absorption of the joints are presented in Figure 5.27.

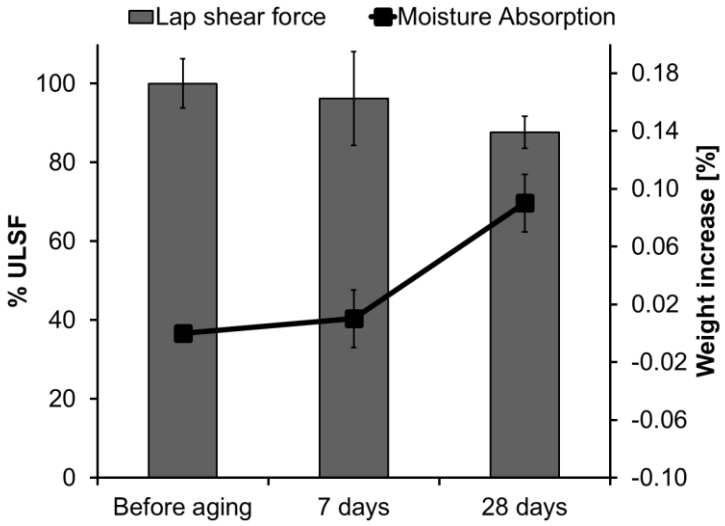

Figure 5.27 Residual strength and moisture absorption of low heat input Al 2024-T3/CF-PPS FSp joints with PPS interlayer after hydrothermal accelerated aging (100% relative humidity at 71°C).

The joints subjected to long-term aging demonstrated a decrease of 12.4% in ultimate lap shear force in comparison to as-joined specimens. The weight increase as a result of moisture absorption was 0.09 ± 0.02 %. The higher reduction in the joints strength when the aging time increased from 7 days to 28 days is probably due to the higher moisture absorption since the joints were exposed longer to the harsh environment. Such results are comparable to the performance of adhesively bonded joints in the literature. For instance, Zhang *et al.* [100] reported a decrease of 20% in lap shear force (from 5.7 kN to 4.6 kN) for Al 6114-T4 bonded joints aged for 20 days under 80°C and 95% of relative humidity.

5.6.4 Failure Mechanisms of Single Lap FSp Joints with Interlayer

The fracture surface of the joints was investigated by SEM to better understand the failure micro-mechanisms involved in FSp joints with interlayer. Goushegir *et al*. [10] has introduced a model to elucidate the bonding mechanisms in FSp joints without interlayer. The bonding area of the FSp joints was divided into three zones: Plastically Deformed Zone (PDZ), Adhesion Zone (AZ) and Transition Zone (TZ) [10] (refer to Section 3.2). Based on this model, two zones were identified in FSp joints with interlayer: PDZ and AZ, as depicted in Figure 5.28. However, in contrast to the proposed model for FSp joints without interlayer a TZ, which has been characterized with a high volume of entrapped air bubbles between AZ and PDZ, was not identified in this work.

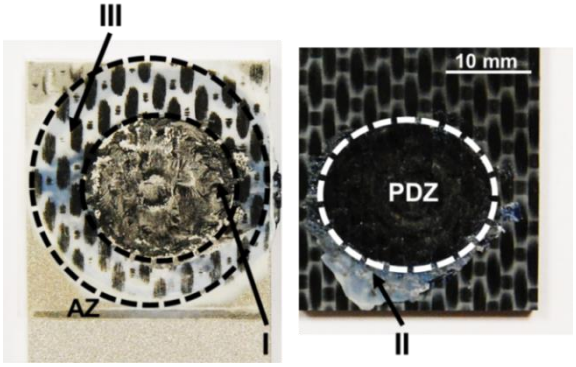

Figure 5.28 Fracture surface of an Al 2024-T3/CF-PPS FSp joint with PPS interlayer indicating the bonding zones and the regions analyzed by SEM.

The PDZ corresponds to the central area of the joint where the mechanically deformed nub is formed and inserted into the interlayer and composite. In this zone the highest process temperature was achieved and the molten film interlayer was squeezed out from the center of the joint (see Figure 5.28). Thus, an intimate contact between soften PPS matrix and carbon fibers with the aluminum surface was observed, increasing micro-mechanical interlocking as one of the main bonding mechanisms. Figure 5.29-A shows the PPS matrix and parts of carbon fibers remained attached to the aluminum surface in the PDZ after mechanical testing.

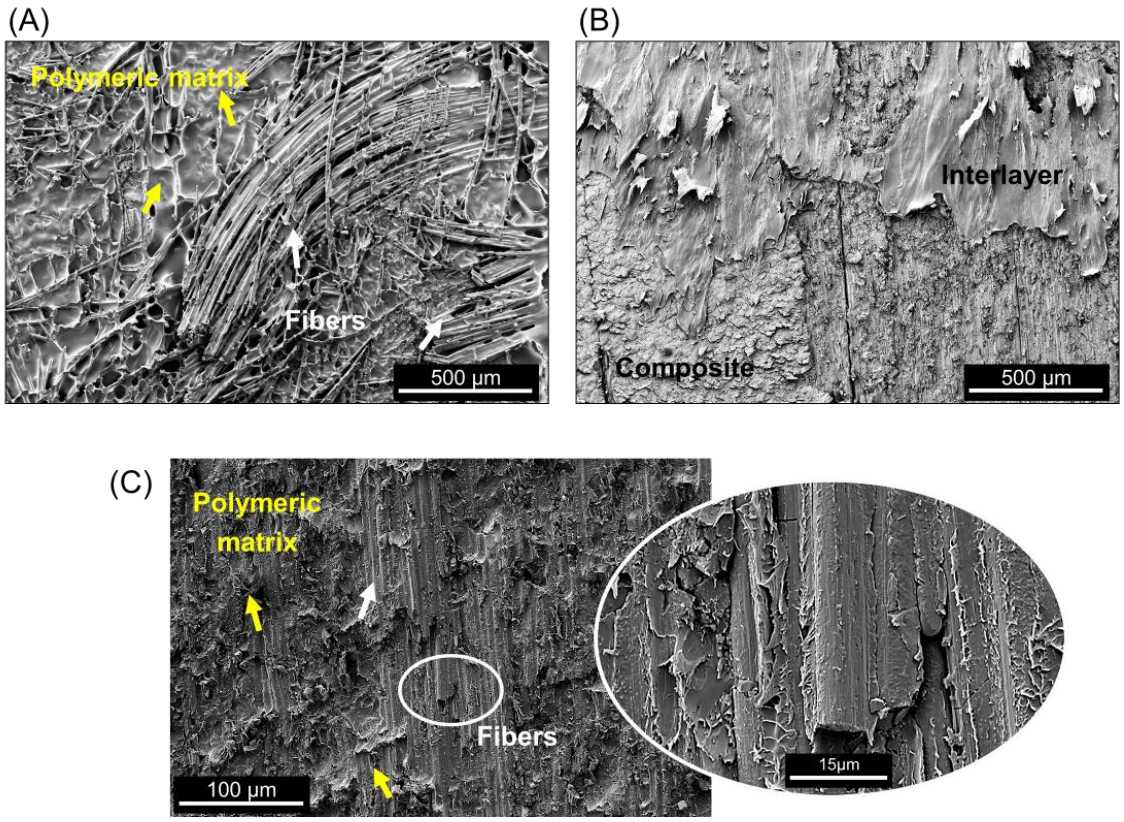

Figure 5.29 (A) Fiber and matrix attachment to the aluminum surface in the PDZ, Region I in Figure 5.28; (B) attached interlayer on the composite surface in the AZ, Region II in Figure 5.28; and (C) PPS matrix and part of carbon fibers remained attached to the interlayer (from black impressions) in the AZ, Region III in Figure 5.28.

The AZ corresponds to the outer region of the joint where the interlayer is identified mostly attached to the aluminum (see Figure 5.28). This is due to the higher process temperature on the aluminum surface; thereby the molten interlayer filled completely the irregularities of the aluminum surface leading to a strong micro-mechanical interlocking. An effective micro-mechanical interlocking was also detected between the PPS interlayer and sandblasted composite in this zone. Therefore, a part of the interlayer was identified attached to the composite part as can be observed in Figure 5.28 and in details in Figure 5.29-B.

Further, impressions (or black spots) from the composite part were identified and analyzed on the surface of the interlayer in the AZ (see Figure 5.28). Figure 5.29-C reveals the SEM image of such impressions (Region III in Figure 5.28). One observes that PPS matrix (yellow arrows in Figure 5.29-C) and part of carbon fibers (indicated by the white ellipse and shown in high-magnification inset image in Figure 5.29-C) remained adhered to the interlayer after failure. It clearly shows the effective micro-mechanical interlocking between the PPS interlayer and the sandblasted composite. Furthermore, this is an opposed behavior in comparison to FSp joints without interlayer. As reported by Goushegir *et al.* [10], the AZ did not demonstrate any indication of mechanical interlocking between the consolidated molten layer and composite as well as attached fibers and has rather less contribution to the global mechanical strength of the joints. The additional micro-mechanical interlocking achieved at the interface of interlayer/composite in the AZ contributes to the superior mechanical strength of the joints with interlayer over those without interlayer, as previously presented in Sections 5.6.1 and 5.6.2.

As also reported by Goushegir *et al*. [10], the PDZ shows a cohesive failure mode. In this region the crack propagates through the first plies of the composite part rather than at the interfaces of the joint (refer to Section 3.2). As a result, fiber and matrix are found attached to the aluminum surface in this zone (Figure 5.29-A). The interlayer remained attached to the composite surface around the PDZ (Figure 5.28) is also an evidence of cohesive failure. In AZ, although the black impressions on the interlayer surface indicate

occurrence of cohesive failure, there are regions with no evidence of black spots. In such regions the crack propagates through the interlayer/composite interface, i.e., adhesive failure. Therefore, similar to the Al 2024-T3/CF-PPS FSp joints without interlayer [10], the joints with interlayer showed a mixed adhesive-cohesive failure mode, however cohesive failure dominates at the interface.

6 CONCLUSIONS

This master thesis was devised to investigate the feasibility of FSpJ of metal-composite structures with additional film interlayer. The scope of the study included the evaluation of the bonding mechanisms for the joints with interlayer, as well as the microstructural and physicochemical changes of the joining parts induced by the process. The influence of composite's surface pre-treatments and accelerated environmental aging on the mechanical performance of the joints were also addressed. Moreover, the mechanical performance of the single lap FSp joints under static and dynamic loading and the respective failure mechanisms were investigated.

Friction spot joints of aluminum alloy 2024-T3 and carbon-fiber-reinforced polyphenylene sulfide laminate composite with additional PPS film interlayer were successfully produced. The highest peak temperature achieved during the joining process was 325°C for low heat input and 417°C for high heat input condition. The peak temperature measured on the surface of the aluminum represented 65% and 83% of the incipient melting point of the Al 2024-T3, for the low and high heat input conditions respectively. The obtained peak temperatures were above the melting point of the PPS matrix of the composite and the PPS film (T_m = 280°C) but below the degradation temperature (starting with crosslinking at 500°C).

The recrystallization of the PPS in both polymeric parts (composite and film interlayer) were analyzed by DSC analysis. The composite in the joint presented a decrease in the degree of crystallinity from 22% for the BM to 18% and 12% for low and high heat input conditions, respectively. Furthermore, the PPS film, initially with very low degree of crystallinity (7%), recrystallized during FSpJ reaching 26% and 27% for the low and high heat input conditions, respectively. Statistical analysis showed that the melting point (T_m) of the PPS (both from the matrix and film interlayer) remained virtually constant to the base material. Additionally, the TGA results compared the onset temperature and the maximum rate of mass loss for specimens from the joints and the respective base materials. No significant changes were observed. Therefore, no evidence

of extensive thermo-mechanical degradation induced by the joining process was identified for the investigated joints.

The evaluation of the interfaces demonstrated two bonding micro-mechanisms: the entrapment of PPS into the crevices of the aluminum and composite surfaces, and carbon fiber entrapment by the deformed aluminum. In addition, the metallic nub is responsible for the macro-mechanical interlocking between the joining parts. Adhesion forces may also act at the interface interlayer/composite as a result of possible intermolecular diffusion of PPS film and matrix.

In a similar way to other friction-based joining processes, three microstructural zones were found in the aluminum part of the joints in this work: SZ, TMAZ and HAZ. Metallurgical phenomena such as dynamic recrystallization (grain refinement), dynamic and static recovery, as well as dissolution and re-precipitation of coherent and incoherent phases may occur as a result of the high temperatures and shear rates imposed by the FSpJ. The local mechanical property of the aluminum part was affected accordingly to the metallurgical phenomena induced by the joining process in each microstructural zone.

It was possible to identify a PHAZ on the composite part of the joint. At the PHAZ temperatures above T_m were achieved allowing the PPS recrystallization. The PHAZ was also characterized with the presence of volumetric defects as microvoids and delamination. A decrease of hardness was identified in this zone (0.32 GPa) compared to the base material (0.39 GPa). Such reduction in hardness is believed to be a result of the reduction in crystallinity (observed with the DSC analysis) and microvoids presence. In addition, the PPS film showed similar level of hardness compared to the PHAZ (0.32 GPa) as a result of the increase in crystallinity during FSpJ.

Mechanical grinding, sandblasting and plasma activation as surface pre-treatments were performed on the composite to enhance the adhesion between the joining parts. A correlation between mechanical performance and surface properties - roughness and wettability - was established. The roughest surface (as a result of sandblasting) led to a better micro-mechanical interlocking between the molten PPS film and the composite surface, leading to the highest

level of strength as well. The plasma activation was performed on a part of the sandblasted composite specimens. However, combination of sandblasting and plasma activation did not show any relevant improvement of the joint strength. All in all, sandblasted specimens showed the best mechanical performance among the surface pre-treatments and were used for the further investigations.

The mechanical performance of the joints with interlayer was evaluated under quasi-static and cyclic loading. The joints with interlayer showed average lap shear strength of 2703 ± 114 N for the high heat input and 3069 ± 166 N for the low heat input joining conditions. The addition of interlayer resulted in increases of up to 55% in the ultimate lap shear force compared to the FSp joints without film. Superior fatigue life of the joints with interlayer in comparison with those without interlayer was also observed. For instance, at 10^5 cycles - the typical application requirement of aircraft industry - the interlayer joint showed fatigue strength of 51% of ULSF, whereas the fatigue strength of the joint without interlayer was 37% of ULSF. In a general trend and in the whole spectrum, the joint with additional interlayer showed a fatigue life approximately 4 times higher than the joint without interlayer.

The durability of the FSp joints with interlayer was evaluated through hydrothermal accelerated aging conditions. The low heat input joints presented a decrease in ULSF of 3.8%, whereas the high heat input joints showed falls of 32% after 7 days in harsh environment. It is assumed that the larger amount of microvoids produced in the high heat input condition facilitates the absorption of environmental moisture. Moreover, the amount of squeezed out interlayer as flash was larger for the joints produced under high heat input, decreasing the sealing contribution of the interlayer in the joints. Since the low heat input joining condition showed a better durability under short-term aging, they were selected for the evaluation of residual strength under the long-term aging conditions (28 days). The aged joints demonstrated a reduction in initial strength of 12.4%, indicating better mechanical performance after hydrothermal aging of FSp joints with interlayer in comparison to Al 6114-T4 adhesively bonded joints (20% of decrease in ULSF).

The failure mechanisms of the joints with interlayer were briefly discussed. Two zones could be identified in this work: PDZ and AZ. PDZ is the central region of the joint where an intimate contact between the aluminum and composite was achieved. PPS matrix and carbon fibers were identified adhered to the aluminum surface in this region by SEM analysis. The AZ is the outer region of the joints, where the interlayer is mostly attached to the aluminum surface as a result of the strong micro-mechanical interlocking between both parts. In addition, some black spots were identified on the surface of the interlayer as attachment of carbon fibers and PPS matrix. These features are an indication of effective micro-mechanical interlocking between the PPS interlayer and composite part in the AZ, which is not found for joints without interlayer. Finally, the joints showed a mixed adhesive-cohesive failure mode while cohesive failure dominates.

The results obtained in this work addressed for the first time the use of film interlayer in friction spot joints. By analyzing the relationship between joining process, microstructure and mechanical properties, this work was able to explain the fundamentals of bonding mechanisms and mechanical performance of friction spot joints with interlayer in comparison to traditional friction spot joints. The mechanical performance of specimens with interlayer was qualitatively demonstrated to be equal or better than state-of-the-art joining techniques for metal-thermoplastic composites. This indicates the potential of the use of film interlayer to improve the mechanical performance of friction spot joints. Therefore, this master thesis has accomplished its scientific and engineering objectives.

7 RECOMMENDATIONS FOR FUTURE WORK

Although this master thesis fulfilled the proposed objectives, some topics remain open for future investigations. This may include:

- The metallurgical phenomena occurring in the FSp joints should be carefully analyzed, for instance through Electron Backscatter Diffraction (EBSD), Energy Dispersive Spectroscopy (EDS) and Transmission Electron Microscopy (TEM). Thus, the recovery, dynamic recrystallization and re-precipitation mechanisms can be better understood.
- The mixing and interdifusion of the PPS matrix and PPS film during FSpJ require further assessments. Raman microscopy and FT-IR are recommended to elucidate these phenomena
- Further analysis of the influence of other usual composite's surface pre-treatments (e.g. acid pickling and anodizing), on the mechanical strength (quasi-static and cyclic) of the joints should be investigated.
- Corrosion resistance (galvanic corrosion) and residual stresses due to the high dissimilar physical properties (e.g. thermal expansion, diffusivity, specific heat, thermal conductivity) of metal and composites are important joint properties to be investigated.

8 REFERENCES

[1] AMANCIO-FILHO, S. T.; DOS SANTOS, J. F. Joining of Polymers and Polymer-Metal Hybrid Structures: Recent Developments and Trends. *Polym. Eng. Sci.*, vol. 49, 8, pp. 1461–1476, 2009.

[2] MALLICK, P. K. *Materials, design and manufacturing for lightweight vehicles*. 1st ed. Cambridge. UK: Woodhead Publishing Limited, 2010.

[3] Boeing 787: From the Ground Up. <www.boeing.com/commercial/aeromagazine/articles/qtr_4_06/article_04_2>. Access: June/2015.

[4] FLIGHT AIRWORTHINESS TECHNOLOGY. Airbus Technical Magazine, vol. FAST 48, 2011.

[5] TenCate Advanced Armour will provide ballistic solutions for the Embraer KC-390, Composites World. <http://www.compositesworld.com/news/tencate-advanced-armour-will-provide-ballistic-solutions-for-the-embraer-kc-390>. Access: June/2015.

[6] BMW i3, the inside story: what it's made of, how it's made, SAE International. <http://articles.sae.org/12056/>. Access: June/2015.

[7] AMANCIO-FILHO, S. T.; DOS SANTOS, J. F. European Patent 2329905B1, 2012.

[8] AMANCIO FILHO, S. T. et al. On the feasibility of friction spot joining in magnesium/fiber-reinforced polymer composite hybrid structures. *Materials Science and Engineering: A*, vol. 528, 10–11, pp. 3841–3848, 2011.

[9] ESTEVES, J. V. et al. Friction spot joining of aluminum AA6181-T4 and carbon fiber-reinforced poly(phenylene sulfide): Effects of process parameters on the microstructure and mechanical strength. *Materials & Design*, vol. 66, pp. 437–445, 2015.

[10] GOUSHEGIR, S. M.; DOS SANTOS, J. F.; AMANCIO-FILHO, S. T. Friction Spot Joining of Aluminum AA2024 / Carbon-Fiber Reinforced Poly(phenylene sulfide)composite single lap joints: microstructure and mechanical performance. *Materials & Design*, vol. 50, pp. 196–206, 2014.

[11] CHANG, B.;SHI, Y.;SHIJIE, D. Comparative studies on stresses in weld-bonded, spot-welded and adhesive-bonded joints. *Journal of Materials Processing Technology*, pp. 230–236, 1999.

[12] FUJII, T. et al. Fatigue Properties of Spot Welded and Spot Weld-Bonded Joints of Steel Sheet. *Procedia Engineering*, vol. 10, pp. 1075–1080, 2011.

[13] MITSCHANG, P.; VELTHIUS, R.; DIDI, M. Induction Spot Welding of Metal/CFRPC Hybrid Joints. *Advanced Engineering Materials*, vol. 15, pp. 804–813, 2013.

[14] CAMPILHO, R. D. S. G. et al. Optimization study of hybrid spot-welded/bonded single-lap joints. *International Journal of Adhesion & Adhesives*, vol. 37, pp. 86–95, 2012.

[15] MCKNIGHT, S. H.; MCBRIDE, M. G.; GILLESPIE, J. W. Joining of Polypropylene and Aluminum: Evaluation of Environmental Durability In INTERNATIONAL SAMPE TECHNICAL CONFERENCE, 25., Covina, 1993, pp. 26 – 28.

[16] CHEN, M.-A.; LI, H.-Z.; ZHANG, X.-M. Improvement of shear strength of aluminium-polypropylene lap joints by grafting maleic anhydride onto polypropylene. *International Journal of Adhesion and Adhesives*, vol. 27, 3, pp. 175–187, 2007.

[17] MARINELLI, J. M.; LAMBING, C. L. T. Advancement in Welding Technology for Composite-to-Metallic Joints. *Journal of Advanced Materials*, vol. 25, pp. 20–27, 1994.

[18] WAGNER, G.; BALLE, F.; EIFLER, D. Ultrasonic Welding of Hybrid Joints. *JOM*, vol. 64, 3, pp. 401–406, 2012.

[19] ROTHEISER, J. *Joining of Plastics 3E: Handbook for Designers and Engineers*. 3rd ed. Munich; Cincinnati, Ohio: Hanser, 2009.

[20] HABENICHT, G. *Applied Adhesive Bonding: A Practical Guide for Flawless Results*. 1st ed. Weinheim: Wiley-VCH, 2009.

[21] MESSLER, R. W. *Joining of Materials and Structures: From Pragmatic Process to Enabling Technology*. 1st ed. Butterworth-Heinemann, 2000

[22] AGEORGES, C. Ageorges; YE, L. Resistance Welding of Metal/Thermoplastic Composite Joints. *Journal of Thermoplastic Composite Materials*, vol. 14, 6, pp. 449–475, 2001.

[23] WESTGATE, S. A. Resistance Welding - State of the Art. *Welding and Cutting*, vol. 55, 5, pp. 256–260, 2003.

[24] JUNG, K. W.; KAWAHITO, Y.; TAKAHASHI, M.; KATAYAMA, S. Laser direct joining of carbon fiber reinforced plastic to zinc-coated steel. *Materials & Design*, vol. 47, pp. 179–188, 2013.

[25] JUNG, K. W.; KAWAHITO, Y.; KATAYAMA, S. Laser direct joining of carbon fibre reinforced plastic to stainless steel. *Science and Technology of Welding and Joining*, vol. 16, 8, pp. 676–680, 2011.

[26] TAMRIN, K. F.; NUKMAN, Y.; ZAKARIYAH, S. S. Laser Lap Joining of Dissimilar Materials: A Review of Factors Affecting Joint Strength. *Materials and Manufacturing Processes*, vol. 28, 8, pp. 857–871, 2013.

[27] KATAYAMA, S.; KAWAHITO, Y. Laser direct joining of metal and plastic. *Scripta Materialia*, vol. 59, 12, pp. 1247–1250, 2008.

[28] BALLE, F. et al. Improvement of Ultrasonically Welded Aluminum/Carbon Fiber Reinforced Polymer-Joints by Surface Technology and High Resolution Analysis: Improvement of Al/CFRP-Joints by Surface Technology. *Advanced Engineering Materials*, vol. 15, 9, pp. 814–820, 2013.

[29] BALLE, F.; WAGNER, G.; EIFLER, D. Ultrasonic Metal Welding of Aluminium Sheets to Carbon Fibre Reinforced Thermoplastic Composites. *Adv. Eng. Mater.*, vol. 11, 1–2, pp. 35–39, 2009.

[30] '2015 GHTC ALUMNI IN DALLAS', award in Lightweight Design, prize of Germany Trade & Invest (GTAI) for GHTC® Alumni to present the Friction Spot Joining. Dallas, USA, 2015.

[31] 'Rising Star, Category Joining Techniques'. Automotive Circle International, award in the Automotive Engineering Expo 2015, Nürnberg, Germany, 2015.

[32] 'Georg-Sachs-Preis', German Society for Materials Science (Deutsche Gesellschaft für Materialkunde –DGM), award in the DGM-Forum 2014, Darmstadt, Germany.

[33] 'German High Tech Champions 2013 in Lightweight Design', award in the category joining technology. Munich, Germany.

[34] 'Raiser Innovation Award for Friction Welding« Category: Auszeichnung. Friction Spot Joining of Lightweight Metals and Fiber-Reinforced Polymer Hybrid Structures, award in the Klaus Raiser GmbH, Munich, 2011.

[35] ANDRÉ, N. M. et al. On the microstructure and mechanical performance of Friction Spot Joining with additional film interlayer. In: ANTEC - SOCIETY OF PLASTICS ENGINEERS, Las Vegas, USA, 2014, pp. 1791–1797.

[36] GOUSHEGIR, S. M. *Friction Spot Joining of Metal-Composite Hybrid Structures*. PhD Thesis, Technical University of Hamburg (TUHH), Hamburg, Germany, 2015.

[37] GOUSHEGIR, S. M. et al. XPS analysis of the interface between AA2024-T3/CF-PPS friction spot joints. *Surf. Interface Anal.*, 2015. doi:10.1002/sia.5816.

[38] ESTEVES, J. V. et al. Friction Spot Joining of aluminum 6181-T4 and carbon fiber reinforced poly(phenylene sulfide). In: ANTEC - SOCIETY OF PLASTICS ENGINEERS, Orlando, FL, USA, 2012.

[39] CRITCHLOW, G. W.; BREWIS, D. M. Review of surface pretreatments for aluminium alloys. *International of Journal Adhesion and Adhesives*, vol. 16, pp. 255–275, 1996.

[40] GOUSHEGIR, S. M.; DOS SANTOS, J. F.; AMANCIO-FILHO, S. T. Influence of process parameters on mechanical performance and bonding area of AA2024/carbon-fiber-reinforced poly(phenylene sulfide) friction spot single lap joints. *Materials & Design*, vol. 83, pp. 431–442, 2015.

[41] WANG, P. C.; MABERY, P.; CHISHOLM, C. K. Degradation of Fatigue Properties of Weld-Bonded Aluminum Exposed to Moisture and Elevated Temperature. *The Journal of Adhesion*, vol. 43, 1–2, pp. 121–137, 1993.

[42] DARWISH, S. M.; AL-SAMHAN, A. Thermal stresses developed in weld-bonded joints. *Journal of Materials Processing Technology*, vol. 153–154, pp. 971–977, 2004.

[43] MA, Y. et al. Laser spot weld bonding of mild steel. *Adhesion & Adhesives*, vol. 34, pp. 1–5, 2011.

[44] LIU, L.; REN, D.; LI, Y. Static mechanics analysis of different laser weld bonding structures in joining AZ61 Mg alloy. *Adhesion & Adhesives*, vol. 31, pp. 660–665, 2011.

[45] Costellium, Technical Datasheet of Alloy 2024, France, 2009.

[46] DAVIS, J. R. Davis. *Aluminum and Aluminum Alloys*. Materials Park, OH: ASM International, 1993.

[47] GHOSH, K. S.; HILAL, M.; BOSE, S. Corrosion behavior of 2024 Al-Cu-Mg alloy of various tempers. *Transactions of Nonferrous Metals Society of China*, vol. 23, 11, pp. 3215–3227, 2013.

[48] ASM Handbook. Properties and Selection: Nonferrous Alloys and Special-Purpose Materials. Vol. 2, 1992.

[49] LAGE, L. G.; KAWANO, Y. Estudo sobre a cinética de decomposição térmica do poli(sulfeto de fenileno). *Polímeros: Ciência e Tecnologia* , vol. 9, pp. 82 – 85, 1999.

[50] CANEVAROLO, S. V. Canevarolo. *Ciência dos Polímeros*. 2nd ed. São Paulo: Artliber, 2006.

[51] MA, C.-C. M. et al. Thermal and Rheological Properties of Poly(Phenylene Sulfide) and Poly(Ether Etherketone) Resins and Composites. *Polymer Composites*, vol. 8, 4, pp. 256–264, 1987.

[52] TANTHAPANICHAKOON W. et al. Mechanical degradation of filter polymer materials: Polyphenylene sulfide. *Polymer Degradation and Stability*, vol. 91, 11, pp. 2614–2621, 2006.

[53] LOVINGER, A. J.; PADDEN, F. J.; DAVIS, D. D. Structure of poly(p-phenylene sulphide). *Polymer*, vol. 29, 2, pp. 229–232, 1988.

[54] NOHARA, L. B. Nohara et al. Study of crystallization behavior of poly(phenylene sulfide). *Polímeros*, vol. 16, 2, pp. 104–110, 2006.

[55] BUDGELL, D. R. et al. Thermal degradation of poly(phenylene sulfide) as monitored by pyrolysis—GC/MS. *Polymer Degradation and Stability*, vol. 43, 1, pp. 109–115, 1994.

[56] JACHOWICZ, J.; KRYSZEWSKI, M.; SOBOL, A. Thermal degradation of poly(2-methylphenylene oxide), poly(2,5-dimethylphenylene oxide) and poly(1,4-phenylene oxide). *Polymer*, vol. 20, 8, pp. 995–1002, 1979.

[57] BALDAN, A. Adhesively-bonded joints in metallic alloys, polymers and composite materials: Adhesives, adhesion theories and surface pretreatment. *Journal of Materials Science*, vol. 39, pp. 1–49, 2004.

[58] WINGFIELD, J. R. J. Treatments of Composite Surfaces for Adhesive Bonding. *International Journal of Adhesion & Adhesives*, vol. 3, pp. 151 – 156, 1993.

[59] PARKER, B. M; WAGHORNE, R. M. Surface pretreatment of carbon fibre-reinforced composites for adhesive bonding. *Composites*, vol. 13, 3, pp. 280–288, 1982.

[60] ABDALLAH, W. et al. Fundamentals of Wettability. In: Oilfield Review, Bahrain, 2007, pp. 46–61.

[61] SHAFRIN, E. G.; ZISMAN, W. A. Constitutive relations in the wetting of low energy surfaces and the theory of the retraction method of preparing monolayers. *J. Phys. Chem.*, vol. 64, 5, pp. 519–524, 1960.

[62] EBNESAJJAD, S. *Surface Treatment of Materials for Adhesive Bondin.* 2nd ed. Oxford: William Andrew Publishing, 2014.

[63] ENCINAS, N. Control of Wettability of Polymers by Surface Roughness Modification. *Journal of Adhesion Science & Technology*, vol. 24, 11-12, pp. 1869–1883, 2010.

[64] KIM, J. K.; LEE, D. G. Investigation of optimal surface treatments for carbon/epoxy composite adhesive joints. *Journal of Adhesion Science and Technology*, vol. 3, pp. 329–352, 2003.

[65] Medical Device & Diagnostic Industry (MDDI). *Surface Modification Using Low-Pressure Plasma Technology*, 2000.

[66] CONRADS, H.; SCHMIDT, M. Plasma generation and plasma sources. *Plasma Sources Science and Technology*, vol. 9, 4, pp. 441–454, 2000.

[67] IQBAL, H. M. S.; BHOWMIK, S.; BENEDICTUS, R. Surface modification og high performance polymers by atmospheric pressure plasma and failure mechanism of adhesive bonded joints. *International Journal of Adhesion & Adhesives,* pp. 418–424, 2010.

[68] Tencate Advanced Composites, Technical Datasheet of CETEX® PPS, Netherlands, 2009.

[69] LITE P, Technical Datasheet of PPS film, Austria, 2009.

[70] BUENO, C. *Estudo de viabilidade técnica de novo processo de união pontuall por fricção de metais a compósitos termoplásticos*. Dipl. Thesis, Federal University of São Carlos (UFSCar), São Carlos, Brazil, 2010.

[71] ESTEVES, J. V. Esteves. *União Pontual por Fricção da Liga de Alumínio 6181-T4 e Compósito Laminado de Poli(Sulfeto de Fenileno) Reforçado com Tecido de Fibra de Carbono*. Master thesis, Universidade Federal de São Carlos, São Carlos (UFSCar), São Carlos, Brazil, 2015.

[72] Composite Materials Handbook: Polymer matrix composites guidelines for characterization of structural materials, vol. 1. United States of America, 2002.

[73] LEE, T. H.; BOEY, F. Y. C.; KHOR, K. A. On the determination of polymer crystallinity for a thermoplastic PPS composite by thermal analysis. *Composites Science and Technology*, vol. 53, 3, pp. 259–274, 1995.

[74] TADMOR, R. Line Energy and the Relation between Advancing, Receding, and Young Contact Angles. *Langmuir*, vol. 20, 18, pp. 7659–7664, 2004.

[75] AMANCIO-FILHO, S.T. et al. Preliminary investigation of the microstructure and mechanical behaviour of 2024 aluminium alloy friction spot welds. *Materials Transactions*, vol. 52, pp. 985–991, 2011.

[76] GAVALYAN, V. B. et al. Thermal degradation mechanism of poly-p-phenylene sulphides. *Polymer Science U.S.S.R.*, vol. 22, 9, pp. 2327–2338, 1980.

[77] PORT, A. B.; STILL, R. H. Synthesis and characterisation of poly(arylene sulphides)—Part 4. Curing and degradation studies. *Polymer Degradation and Stability*, vol. 2, 1, pp. 1–22, 1980.

[78] MONTGOMERY, D. C.; RUNGER, G. C. *Estatística Aplicada e Probabilidade para Engenheiros*. 5th ed. Rio de Janeiro, RJ: LTC Editora, 2009.

[79] SUHUDDIN, U. F. H. R. et al. Grain structure evolution during friction-stir welding of AZ31 magnesium alloy. *Acta Materialia*, vol. 57, 18, pp. 5406–5418, 2009.

[80] BOZZI, S. et al. Influence of FSSW parameters on fracture mechanisms of 5182 aluminium welds. *J. Mater. Process. Technol.*, vol. 210, 11, pp. 1429–1435, 2010.

[81] REED-HILL, R. E.; ABBASCHIAN, R. *Physical Metallurgy Principles*. 4th ed. Cengage Learning India, 2008.

[82] GENEVOIS, C. et al. Quantitative investigation of precipitation and mechanical behaviour for AA2024 friction stir welds. *Acta Materialia*, vol. 53, 8, pp. 2447–2458, 2005.

[83] NISBET, D. R. et al. Surface and bulk characterisation of electrospun membranes: Problems and improvements. *Colloids and Surfaces B: Biointerfaces*, vol. 71, pp. 1–12, 2009.

[84] NISBET, D. R. et al. The effect of surface hydrophilicity on the behavior of embryonic cortical neurons. *Journal of Colloid and Interface Science*, vol. 299, pp. 647–655, 2006.

[85] STONE, M. H. Effect of degree of abrasion of composite surfaces on strengths of adhesively bonded joints. *Research Report*, 1981.

[86] ANAGREH, N.; DORN, L.; BILKE-KRAUSE, C. Low-pressure plasma pretreatment of polyphenylene sulfide (PPS) surfaces for adhesive bonding. *International Journal of Adhesion & Adhesives*, pp. 16–22, 2007.

[87] ANDRÉ, N. M. et al. Influência da Espessura do Filme Polimérico Intermediário na Resistência Mecânica de Juntas Híbridas de Alumínio 2024-T3 e CF-PPS Produzidas por União Pontual por Fricção. In: CONGRESSO NACIONAL DE SOLDAGEM, 41., Salvador - BA, Brazil, 13 - 15 of October, 2015.

[88] JUNG, K.-W.; KAWAHITO, Y.; KATAYAMA, S. Mechanical property and joining characteristics of laser direct joining of CFRP to polyethylene terephthalate. *Int. J. of Precis. Eng. and Manuf.-Green Tech.*, vol. 1, 1, pp. 43–48, 2014.

[89] CHANG, B.; SHI, Y.; LU, L. Studies on the stress distribution and fatigue behavior of weld-bonded lap shear joints. *Journal of Materials Processing Technology*, vol. 108, 3, pp. 307–313, 2001.

[90] BROCKMANN, W. Durability of Adhesion Between Metals and Polymers. *Jounal of Adhesion*, pp. 53 – 61, 1989.

[91] KIM, W-S.; LEE, J-J. Adhesion strength and fatigue life improvement of co-cured composite/metal lap joints by silane-based interphase formation. *Journal of Adhesion Science & Technology*, vol. 21, 2, pp. 125–140, 2007.

[92] DUBÉ, M. et al. Fatigue performance characterisation of resistance-welded thermoplastic composites. *Composites Science and Technology*, vol. 68, 7–8, pp. 1759–1765, 2008.

[93] MIKLAVEC, M. et al. Fatigue strength of a hybrid joint formed between a PA6-GF60 polymer matrix and a S420MC steel insert. *Materials & Design*, vol. 51, pp. 493–500, 2013.

[94] ROESLER, J.; HARDERS, H.; BAEKER, M. *Mechanical Behavior of Engineering Materials: Metals, Ceramics, Polymers, and Composites*. 1st ed. Germany: Springer, 2007.

[95] WHITWHORTH, H. A. Fatigue evaluation of composite bolted and bonded joints. *Journal of Advanced Materials*, vol. 30, pp. 25–31, 1998.

[96] SCHIMDT, H. J.; SCHIMDT, B. Fatigue & Damage Tolerance and Composite Training. Helmholtz-Zentrum Geesthacht: Geesthacht, 2012.

[97] KINLOCH, A. J.; LITTLE, M. S. G.; WATTS, J. F. The role of the interphase in the environmental failure of adhesive joints. *Acta Materialia*, vol. 48, 18–19, pp. 4543–4553, 2000.

[98] CALLISTER, W. D. J. *Materials Science and Engineering: An Introduction-Text Only*. 7th ed. Wiley Publishers, 2006.

[99] BRYDSON, J. A. *Plastics Materials*. Butterworth-Heinemann. 1999.

[100] ZHANG, F. et al. Durability of adhesively-bonded single lap–shear joints in accelerated hygrothermal exposure for automotive applications. *International Journal of Adhesion and Adhesives*, vol. 44, pp. 130–137, 2013.

APPENDIX A - FITTING PROCEDURE FOR S-N CURVES

The fitting procedure of the S-N curves obtained from the plot of the fatigue results followed the ASTM E379-10. This standard covers the S-N relationships that may be reasonably approximated by a straight line. Thus, the produced model is in the linear form:

$$Y = A + B \cdot X \qquad \text{Equation (A.1)}$$

Where Y is log N; N is number of cycles; and X is the maximum level of load applied during the fatigue test (F_{max}). Then, to calculate the parameters A and B in Equation A.1, the following equations were applied:

$$\hat{A} = \overline{Y} - B \cdot \overline{X} \qquad \text{Equation (A.2)}$$

$$\hat{B} = \frac{\sum_{i=1}^{k}(X_i - \overline{X}) \cdot (Y_i - \overline{Y})}{\sum_{i=1}^{k}(X_i - \overline{X})^2} \qquad \text{Equation (A.3)}$$

Where the symbol caret (^) denotes estimate, the symbol overbar (–) denotes average, Y_i = log N_i, X_i = $F_{max\ i}$, and k is the total number of tested joints.

The obtained parameters for the joints were:

- For low heat input condition: A = 8.629 and B = - 0.0024
- For high heat inout condition: A = 7.993 and B = - 0.0021

After obtain the parameters, the adequacy of the linear model must be tested. For this purpose, it is supposed that fatigue tests were conducted at l different levels of load (X) and that m_i replicate values of Y were observed at each X_i. In this way, the hypothesis of linearity is approved if the computed value of:

$$\frac{\sum_{i=1}^{l} m_i \cdot \left(\hat{Y} - \overline{Y_i}\right)^2 / (l-2)}{\sum_{i=1}^{l} \sum_{j=1}^{m_i} \frac{(Y_{ij} - \overline{Y_i})^2}{k-l}} \qquad \text{Equation (A.4)}$$

do not exceeds F_p, which is provided by the standard in a table for the desired level of significance. Consider that k is computed as $\sum_{i=1}^{l} m_i$ in Equation A.4.

The current work tested 3 different levels of load, with 3 replicates per level in the fatigue testing of the joints. Thereby, in order to perform the linearity

F test, two degrees of freedom should be established for the specimens in analysis: $n_1 = l - 2$ and $n_2 = k - l$. For the current analysis n_1 is 1 and n_2 is 6. In this way, the F_p obtained from the standard is 5.9874 for 5% significance level, and 13.745 for 1% significance level. On the other hand, the adequacy values calculated for the joints are:

- For low heat input condition: 2.998
- For high heat inout condition: 13.409

Therefore, the linearity hypothesis is approved for the low heat input condition with 5% significance level, whereas the high heat input the condition got the hypothesis approved for 1% significance level.

It is important to note that the ASTM E379 recommends the exclusion of run-outs and stopped specimens from the analysis. However, in the present analysis, once only three levels of load were tested, the run-out specimens were included to turn the analysis statistically feasible. The referred run-outs are the joints tested at 35% of ultimate lap shear force which overcome 1 million cycles without failure.

In summary, the estimated fitting S-N curves are:

- For low heat input condition: $\log N = 8.629 - 0.0024.F_{max}$, 1 % significance level
- For high heat input condition: $\log N = 7.993 - 0.0021.F_{max}$, 5% significance level

APPENDIX B - CALCULATION METHOD OF THE COOLING RATES APPLIED DURING FSpJ

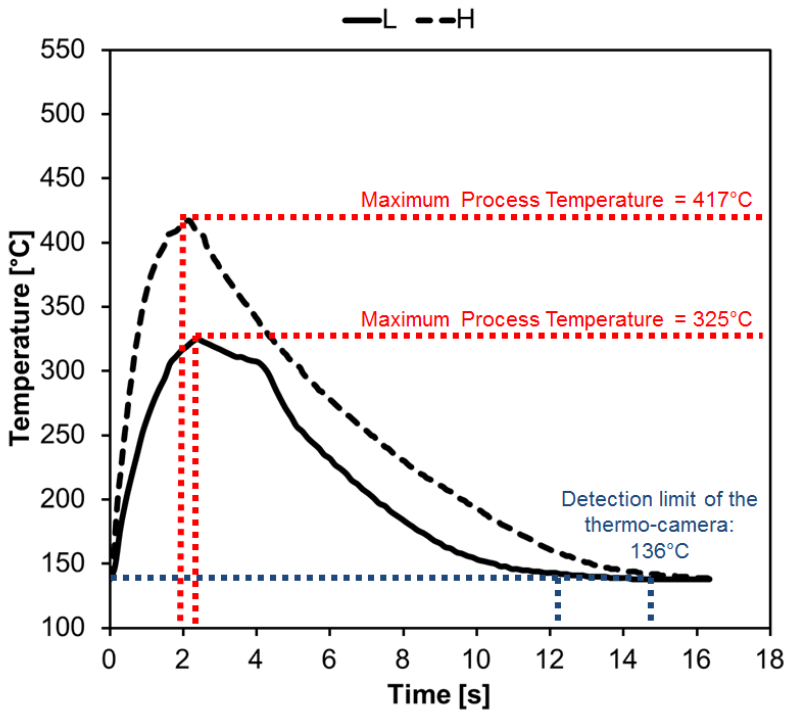

Figure B.1: Temperature evolution during FSpJ for joints produced with high and low heat input conditions. The temperatures and times used to calculate the cooling rates are indicated.

The cooling rate (CR) was calculated in accordance to Equation B.1:

$$CR = \frac{MPT - DLT}{t(DLT) - t(MPT)} \qquad \text{Equation (B.1)}$$

Where MPT is the maximum process temperature achieved, DLT is the limit of detection temperature of the thermo-camera used, and t(T) denotes time (t) as a function of the process temperature (T).

APPENDIX C - ANALYSIS OF VARIANCE (ANOVA) AND TUKEY TEST

The Analysis of Variance (ANOVA) is a statistical method employed in this work to evaluate responses of DSC, TGA and nanohardness tests through comparisons of means and variance. Thus, the significance of the properties variation between base and joint's material can be statistically stated [77].

The responses to be analyzed through ANOVA must have a normal distribution, with the mean as the central point. The means and the associated variances are compared based on a system of hypothesis testing. The null hypothesis (H_0) states that there is no statistical difference among the means in comparison, whereas the alternative hypothesis (H_1) states that they are statistically different. There are two type of errors associated to the hypothesis testing: type I and type II. The type I (α, alfa) consists in the probability of reject H_0 when it is in fact true. The type II (β, beta) is the probability of do not reject H_0 when it is in fact false. The current work employed the error type I, with 95% of confidence, so α is 5% or 0.05.

Once the type and level of error is established, it is applied the test "p" in order to verify the rejection or approval of the null hypothesis (H_0). In this work, the *Minitab® 16* statistical software were employed. The test consists in compare a p-value and the α of the analysis. The p-value is obtained through a equation which considers the variance of the response. For p-values superior than α the H_0 is approved. Thus, the means in comparison are statistically equal. In the case p-value is inferior than α, H_0 is rejected. It states that the means in comparison are statistically different.

The test p indicates if at least one of the means are different from the others. However, it does not indicate which one. This identification can be achieved through the multiple comparison method of Tukey. The Tukey test enables comparisons among all the responses based on a least significant difference (lsd) which is obtained from the means and variances of the responses. Considering the confidence level established for the ANOVA, the software sorts in ascending order the means in comparison and assign one letter of the alphabet for the first one. Then, the first mean is compared to the next one. If the difference between them is larger than lsd, then the second

mean receives a different letter. On the other hand, if the difference is smaller than lsd, then the second average receive the same letter of the first one. At the end, the means that present a statistically significant difference do not share a letter, whereas the ones which are statistically equal will have a letter in common. Thus, it is possible to statistically identify which means are coincident and which differ from each other. The Tukey test is especially useful in this work to compare the properties variation of the joining parts before and after the FSpJ process.

APPENDIX D - ANALYSIS OF THE JOINT'S INTERFACE FOR THE HIGH HEAT INPUT JOINING CONDITION

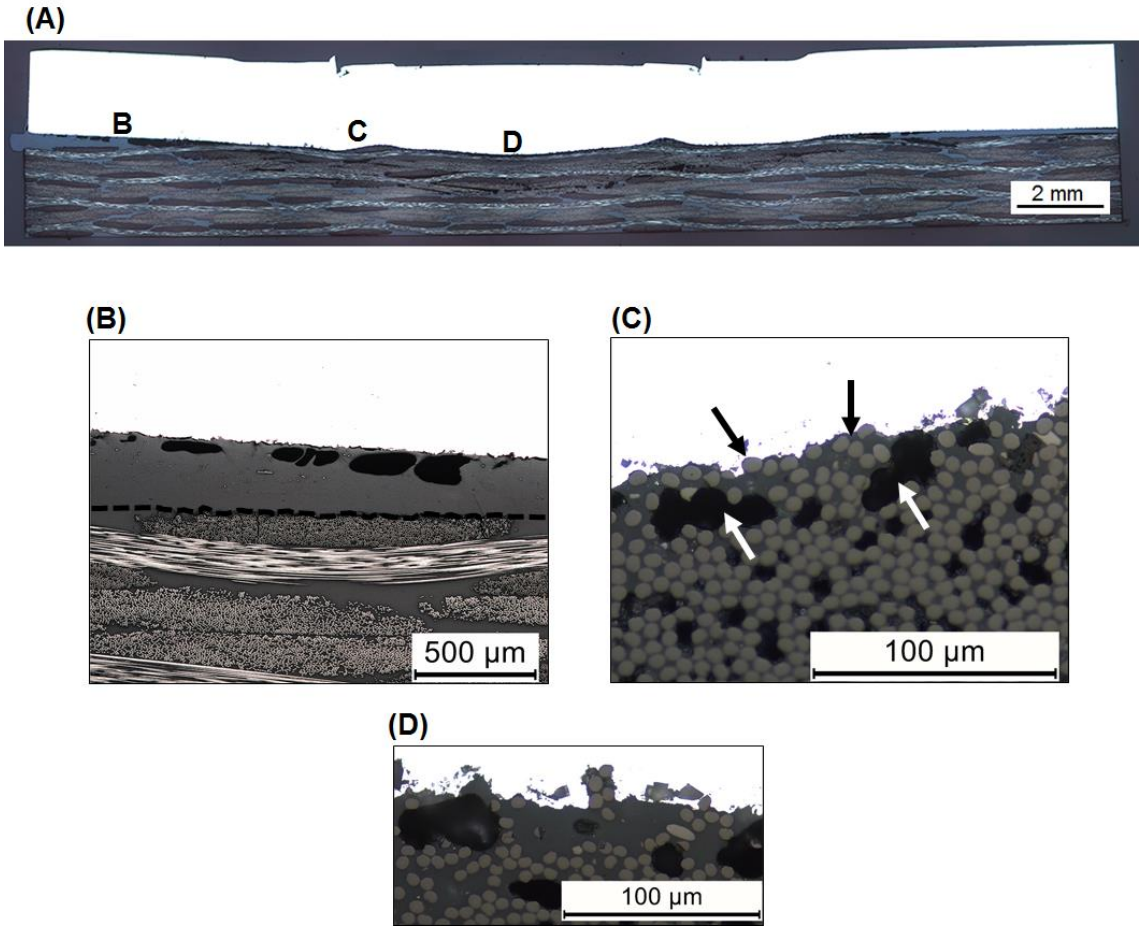

Figure D.1: Microstructural details of the joint interface: (A) cross section of an FSp joint with interlayer; (B) interface of aluminum/interlayer/composite at the edge of the joint; (C) carbon fibers embedded by the aluminum (black arrows), and microvoids (white arrows); (D) entrapped molten polymer into the crevices of sandblasted aluminum surface.

APPENDIX E - DETAILED SHEAR FORCE-DISPLACEMENT CURVES OF SINGLE LAP FSP JOINTS WITH INTERLAYER

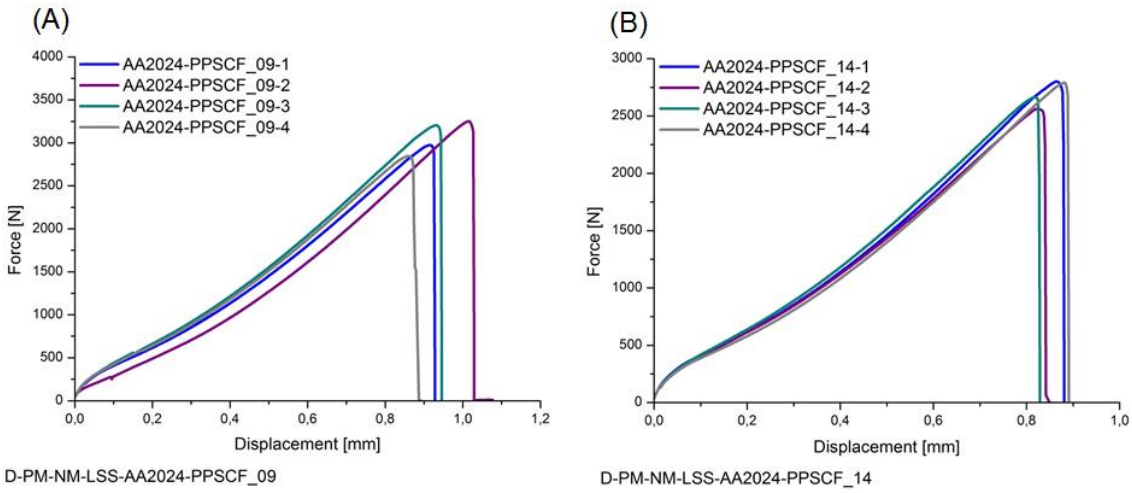

Figure E.1: Shear force-displacement curves for Al 2024-T3/PPS/CF-PPS FSp joints produced with (A) low heat and (B) high heat input conditions.

APPENDIX F - COMPARISON OF SHEAR FORCE-DISPLACEMENT CURVES OF SINGLE LAP FSP JOINTS WITH AND WITHOUT INTERLAYER

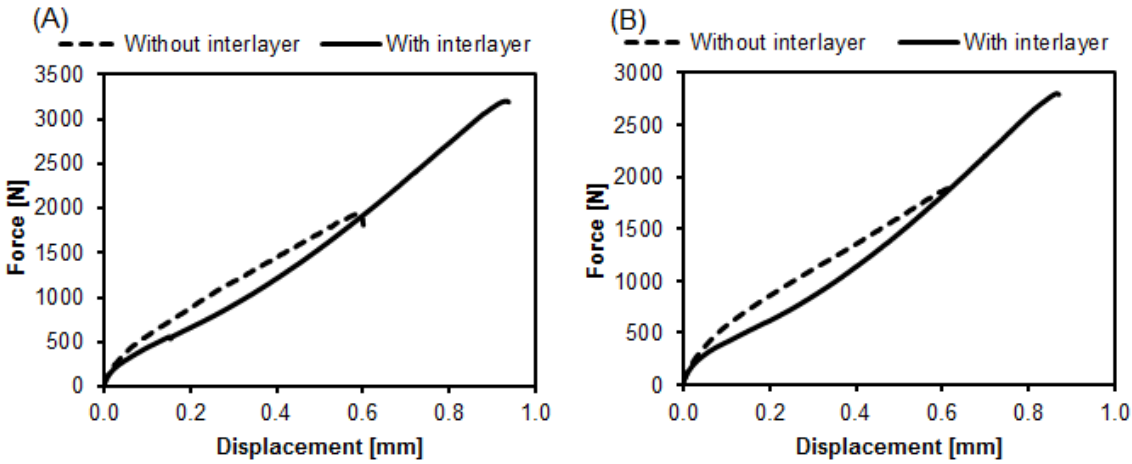

Figure F.1: Representative examples of shear force-displacement curves for FSp joints with and without interlayer produced under (A) low heat and (B) high heat input conditions.